Inferring the Elastic Structure of the Earth's Mantle using the Spectral Element Method

by

Vedran Lekic

B.A. (Harvard University) 2004

A dissertation submitted in partial satisfaction of the
requirements for the degree of
Doctor of Philosophy

in

Earth and Planetary Science

in the

Graduate Division
of the
University of California at Berkeley

Committee in charge:

Professor Barbara Romanowicz, Chair
Professor Michael Manga
Professor Geoffrey W. Marcy

Fall 2009

The dissertation of Vedran Lekic is approved:

Chair _____ Date _____

_____ Date _____

_____ Date _____

University of California, Berkeley

Fall 2009

Inferring the Elastic Structure of the Earth's Mantle using the Spectral Element Method

by

Vedran Lekic

Abstract

Inferring the Elastic Structure of the Earth's Mantle using the Spectral Element Method

by

Vedran Lekic

Doctor of Philosophy in Earth and Planetary Science

University of California at Berkeley

Professor Barbara Romanowicz, Chair

Mapping the elastic and anelastic structure of the Earth's mantle is crucial for understanding the temperature, composition and dynamics of our planet. Extracting the information contained in seismic waveforms is the key to constraining the elastic and anelastic structure within the Earth, and is the goal of our work. In the past quarter century, global tomography based on ray theory and first-order perturbation methods has imaged long-wavelength velocity heterogeneities of the Earth's mantle. However, the approximate techniques upon which global tomographers have traditionally relied become inadequate when dealing with crustal structure, as well as short-wavelength or large amplitude mantle heterogeneity. The spectral element method, on the other hand, permits accurate calculation of wave propagation through highly heterogeneous structures, and is computationally economical when coupled with a normal mode solution and applied to a restricted region of the earth such as the upper mantle (SEM: Capdeville et al., 2003). Importantly, SEM

allows a dramatic improvement in accounting for the effects of crustal structure.

Here, we develop and apply a new hybrid method of tomography, which allows us to leverage the accuracy of SEM to model fundamental and high-mode long period (>60s) waveforms. We then present the first global model of upper mantle velocity and radial anisotropy developed using SEM. Our model, SEMum, confirms that the long-wavelength mantle structure imaged using approximate semi-analytic techniques is robust and representative of the Earth's true structure. Furthermore, it reveals structures in the upper mantle that were not clearly seen in previous global tomographic models, providing new constraints on the temperature, composition as well as flow in the mantle. We show that applying a clustering analysis to the absolute shear wave-speed profiles offers a powerful new way of exploring the relationship between surface expressions of tectonics and their elastic signature in the upper mantle. We note that this new hybrid approach to tomography can be applied to a bigger and higher-frequency dataset in order to gain new insights into the structure of the lower mantle and more robustly map seismic structure at the regional and smaller scales.

Professor Barbara Romanowicz, Chair

To my grandfather, for encouraging me to explore.

Contents

List of Figures

List of Tables

Acknowledgements

I foremost would like to thank Barbara Romanowicz for providing guidance, support and inspiration throughout my graduate studies. I also gratefully acknowledge the support of my other dissertation committee members: Professors Michael Manga and Geoffrey Marcy. I thank my collaborators, Fabio Cammarano, Adam Dziewonski, Jan Matas and Mark Panning, for their insights and assistance, and my friend and colleague, Karl Kappler, for helping me with and candidly commenting on my research. I would also like to thank Yann Capdeville for providing me the cSEM code used in much of this work, and assisting me with modifying and using it.

I am deeply appreciative of my fellow graduate students for helping sustain an environment in which criticism is constructive and excitement about science is ubiquitous.

Of course, nothing would have been possible without the support of my friends and family, who have willingly shared my joys and disappointments.

Finally, I would like to acknowledge the staff at the Department of Earth and Planetary Science and especially within the Berkeley Seismological Laboratory for providing and maintaining our seismic networks, computing resources, and administrative services. This work was financially supported through a National Science Foundation Graduate Research Fellowship, a UC Berkeley Graduate Fellowship, and NSF grant EAR-0738284. Many of the large-scale computations were carried out at the National Energy Research Scientific Computing Center.

Chapter 1

Introduction

Global networks of digital seismometers routinely record seismic waves that, once excited by earthquakes, travel thousands of miles through the Earth. During their voyage, seismic waves are affected by variations in elastic wavespeeds and by anisotropy, which causes differently polarized waves to travel at different velocities. Variations of velocity provide clues to the temperature and composition in the Earth's interior, while anisotropy can be used to infer flow within the mantle. Furthermore, the waves lose energy due to microscopic (anelastic) dissipative processes operating at a variety of timescales. This energy loss is thought to be strongly dependent on temperature, and is summarized by a quantity $Q \propto -1/\Delta E$, which varies with frequency and position in the Earth.

Thus, precise observations of seismic waveforms contain information on the elastic and

anelastic structure - and through them, the thermal and compositional state - of the Earth's interior. Extracting this information with the goal of imaging the Earth's interior at local, regional and global scales has been the focus of intense study since the beginnings of seismology. This work builds upon the efforts on the global scale, and attempts to improve the constraints of mantle elastic and anelastic structure of the Earth's upper mantle. In its course, we identify and seek to address a set of challenges that have stymied the development of higher resolution images of the Earth's interior.

We first turn our attention to resolving the heretofore poorly constrained frequency dependence of attenuation. Despite strong indications from theoretical and laboratories studies that Q increases with frequency, the difficulty of a robust measurement of this frequency dependence in the Earth has compelled seismologists to routinely assume that Q is independent of frequency. Yet, constraining the frequency dependence of intrinsic seismic attenuation is crucial for: 1. correcting for velocity dispersion due to attenuation; 2. constructing attenuation and velocity models of the interior using datasets with different frequency contents; and, 3. interpreting lateral variations of velocity and attenuation in terms of temperature and composition. Frequency dependence of attenuation q can be represented by a power law $q \propto q_0^{-\alpha}$. Despite its importance, efforts at determining α from surface wave and free oscillation data have been thwarted by the strong tradeoffs between the depth- and frequency dependence of attenuation.

In Chapter 2, we develop and validate a new method that eliminates this tradeoff, allow-

ing a direct estimation of effective frequency dependence of attenuation without having to construct a new depth-dependent model of attenuation. Using normal mode and surface wave attenuation measurements between 80 and 3000 s, we find that α varies with frequency within the absorption band. It is 0.3 at periods shorter than 200 s, it decreases to 0.1 between 300 and 800 s, and becomes negative at periods longer than 1000 s. We then discuss the implications that this observation holds for the construction of 1D profiles of attenuation and for performing velocity dispersion corrections.

In Chapters 3-5, we turn our attention to the elastic structure of the upper mantle.

Accurate accounting for the effects of crustal structure on long-period seismic surface waves and overtones is difficult but indispensable for determining elastic structure in the mantle. Standard linear crustal corrections have been shown to be inadequate on the global scale, and newer non-linear techniques are computationally expensive when applied to waveforms containing higher frequencies and/or overtones. In Chapter 3, we describe a technique for significantly improving the accuracy of linear corrections without increasing the computational cost. We validate the technique by using the Spectral Element Method to carry out a series of synthetic tests that probe the consequences of using both standard and our modified linear crustal corrections. We show that the use of standard linear corrections can cause significant contamination of retrieved isotropic mantle velocities to 150 km depth and anisotropic structure to 250 km. At depths shallower than 100 km, anisotropic structure can be obliterated by purely crustal effects. The use of the modified linear cor-

rections nearly eliminates the contamination of isotropic mantle structure, and significantly reduces contamination of anisotropic structure. Finally, we apply the technique to a real long period waveform dataset and demonstrate the benefit of improved crustal corrections on the retrieved model.

Chapter 4 describes a novel hybrid approach to long-period waveform tomography, that we have developed. In the past quarter century, global tomography based on ray theory and first-order perturbation methods has imaged long-wavelength velocity heterogeneities of the Earth's mantle. While these models have contributed significantly to our understanding of mantle circulation, the development of higher resolution images of the Earth's interior holds tremendous promise for understanding the nature of the observed heterogeneities. This endeavor confronts us with two challenges. First, it requires extracting a far greater amount of information from the available seismograms than is generally used. Second, the approximate techniques upon which global tomographers have traditionally relied become inadequate when dealing with short-wavelength heterogeneity. The spectral element method, on the other hand, permits accurate calculation of wave propagation through highly heterogeneous structures, and is computationally economical when coupled with a normal mode solution and applied to a restricted region of the earth such as the upper mantle (cSEM: Capdeville et al., 2003). Importantly, cSEM allows a dramatic improvement in accounting for the effects of crustal structure.

In order to meet these challenges, we have developed a novel approach in which forward-

modeling is performed using the Coupled Spectral Element Method (CSEM: Capdeville et al., 2003), which can accurately model seismic wave propagation in a 3D earth with both short and long wavelength structure, while in the inversion step, the sensitivity kernels are calculated using an approximate, non-linear normal mode summation approach (NACT: Li and Romanowicz, 1995). Modeling is performed in an iterative fashion, and convergence is achieved as long as the average sign of the sensitivity kernels is correct. Indeed, we verify that the use of approximate kernels does not prevent our iterative procedure from converging. We start our iterative inversion procedure with a 1D model, so as to not bias our results toward existing 3D upper mantle models. Our dataset consists of complete 3-component time domain seismograms filtered at periods greater than 80 s for 100 earthquakes observed at well over 100 stations of the IRIS/GSN, GEOSCOPE, GEOFON and various regional broadband networks. In order to improve the resolution of shallow structure, we supplement this waveform dataset with maps of group velocity dispersion in the 25-150s range, provided by M. Ritzwoller.

In Chapter 5, we present the first global model of upper mantle velocity and radial anisotropy developed by applying the SEM to modeling fundamental- and higher-mode waveforms. Our model confirms the large- scale features observed by previous researchers. In particular, we retrieve the relatively shallow, seismically slow velocities beneath volcanic arcs and mid-ocean ridges, the deeper fast roots underlying cratons, slow velocities in the central Pacific below 250km depth, and enhanced fast velocities anomalies consistent with slab locations in the transition zone. We discuss notable features of the model, comparing

and contrasting them with global and regional models developed using less accurate techniques. We then infer the thickness of the lithosphere across the globe, by associating the lithosphere-asthenosphere boundary with the strongest negative gradients of velocity with depth. Finally, we apply a clustering analysis to the profiles of absolute shear wavespeed in order to explore the relationship between surface tectonics and upper mantle elastic structure. This approach allows us to distinguish oceanic and continental regions, as well as make more nuanced distinctions, such as those between stable and tectonically active continents as well as to identify the world's major cratons using only our tomographic model.

In Chapter 6, we summarize the implications enabled by the hybrid tomographic technique developed in Chapter 4 and applied in Chapter 5 to the creation of a new upper mantle anisotropic model. We identify a number of potential ways in which the results of our work can be used to better constrain the temperature and composition of the mantle as well as its flow field. Finally, we explain how our anisotropic upper mantle model can be used to facilitate the development of a model of 3D variations of seismic attenuation in the upper mantle. The development of such a model would provide complementary and independent constraints on temperature within the mantle.

Chapter 2

Measurement and Implications of Frequency Dependence of Attenuation

2.1 Introduction

As they propagate through the Earth, seismic waves experience attenuation and dispersion resulting from microscopic dissipative processes operating at a variety of relaxation times. These dissipative effects can be summarized by the macroscopic quantity $q = -\Delta E/2\pi E_{max}$, where ΔE is the internal energy lost by a seismic wave in one cycle. This quantity can be related to the often-used quality factor Q through $q \equiv (1/Q)$. The Earth acts as an absorption band (e.g. Anderson, 1976) and attenuation depends on the fre-

quency of oscillation. Within the absorption band, attenuation is relatively high and does not strongly depend on frequency. Outside the band, attenuation rapidly decreases with frequency. Since the relaxation times of the dissipative processes giving rise to the absorption band might strongly depend on pressure and temperature, the frequency bounds of the band can change with depth (e.g. Anderson and Minster, 1979; Minster and Anderson, 1981; Anderson and Given, 1982). Within the absorption band, the frequency dependence of q can be described using a power law, $q \propto \omega^{\alpha}$, with a model-dependent α, usually thought to be smaller than 0.5 (e.g. Anderson and Minster, 1979).

In the past few years, three new models of 3-D variations in upper mantle attenuation have been developed (Selby and Woodhouse, 2002; Gung and Romanowicz, 2004; Dalton and Ekström, 2006), offering the promise of clarifying the origin (thermal versus chemical) of lateral heterogeneities. Yet, knowing the value of α within the absorption band is required for interpreting lateral variations in attenuation in terms of temperature. It is also one of the governing parameters for interpreting observed lateral variations in seismic velocities. Matas & Bukowinski (2007) proposed a self-consistent attenuation model based on solid state physics and showed that anelasticity can substantially enhance seismic anomalies due to high temperature (by $\sim$ 30 %), thus confirming earlier observations of Romanowicz (1994). It is important to note that interpreting attenuation in terms of temperature and predicting its effects on seismic anomalies is only reasonable if the contribution of scattering is small compared to that due to intrinsic anelastic processes.

A non-zero α implies that seismic waves of different frequencies are differently attenuated, and accordingly modifies the velocity dispersion relation. This has three important consequences: 1) Because oscillations at different frequencies can have very different depth sensitivities to elastic and anelastic properties of the Earth, the value of α affects the construction and interpretation of such profiles. In particular, the lower mantle q is mostly constrained by low-frequency modes and is thus not directly comparable to q obtained from high-frequency modes, which sample the upper mantle. A single radial attenuation profile is only relevant if $\alpha = 0$; 2) Because the frequency content of different attenuation measurements can differ, combining these datasets requires accounting for the effect of α. For instance, if $\alpha = 0.3$, then q varies by a factor of two in a dataset including periods between 50s and 5s; 3) Because geophysical datasets used to constrain Earth structure have very different dominant frequencies, using them together requires applying a dispersion correction whose functional form is different for a non-zero α than it is under the assumption of frequency independent attenuation (Minster and Anderson, 1981).

Efforts at determining α of the mantle have followed three approaches: theoretical studies, laboratory experiments and seismological observations. Theoretical investigations have focused on explaining the origin of the absorption band and incorporating models of likely relaxation mechanisms developed using solid state physics. Liu et al. (1976) and Kanamori and Anderson (1977) modeled the absorption band for a standard linear solid as a superposition of relaxation mechanisms, whose combined effects resulted in a frequency-independent q within the absorption band. Minster and Anderson (1981) applied insights

from solid state physics to suggest that, for dissipation dominated by dislocation creep, $\alpha > 0$ within the absorption band. Building on this work, Anderson and Given (1982) developed an absorption band model of the Earth in which the effects of pressure and temperature on the underlying relaxation mechanisms caused the frequency bounds of the band to change with depth.

Despite observational and experimental advances, no clear consensus concerning the value of mantle α has emerged over the past 25 years. Nevertheless, theoretical predictions of $\alpha > 0$ have been systematically confirmed in various laboratory studies. In their review paper, Karato & Spetzler (1990) argued that its value lies between 0.2 and 0.4. A more recent review by Romanowicz & Mitchell (2007) identifies a number of studies that collectively constrain α to the 0.1-0.4 range. On the laboratory front, Jackson et al. (2005) obtained α of 0.28 ± 0.01 for a fine-grained olivine sample at a pressure of 300 MPa and temperature of 1200 $^{\circ}$C. Relating laboratory measurements to α in the real mantle, however, is not straightforward, due to uncertainties in extrapolating laboratory measurements to actual mantle materials under high-pressure and high-temperature conditions prevailing in the mantle.

On the other hand, seismological efforts at constraining globally-averaged α within the absorption band have benefited from numerous measurements of surface wave or normal mode attenuation. Yet, although attenuation measurements of nearly 250 individual modes are currently available from the website of the Reference Earth Model project

(http://mahi.ucsd.edu/Gabi/rem.html, see Fig. 1), the determination of α has been confounded by the fact that oscillations at different frequencies can have very different depth sensitivities to elastic and anelastic properties of the earth. As a result of this tradeoff between frequency and depth effects, radial variations of attenuation can obscure the α signal. The only studies attempting to obtain α within the absorption band have found α ranging from 0.1 to 0.3 while emphasizing the lack of resolution on the inferred values (Anderson and Minster, 1979; Anderson and Given, 1982; Smith and Dahlen, 1981). More recent studies (e.g. Shito et al., 2004; Cheng and Kennett, 2002; Flanagan and Wiens, 1998) have relied upon analysis of body waves to argue for values of α in the 0.1-0.4 range. However, these studies were restricted to frequencies higher than 40mHz and were of regional character, leaving unanswered the question of the average mantle α.

A further complication in determining the frequency dependence of attenuation from seismic data arises from the discrepancy between attenuation measurements of spheroidal modes carried out using a propagating (surface) wave and those using a standing wave (normal mode) approach. As can be seen in Fig. 1, surface wave studies indicate attenuation values that are higher by about 15-20% than normal mode measurements of the same frequency. This discrepancy is not present in the toroidal modes. The origin of the discrepancy has not yet been determined. Whereas Durek & Ekström (1997) argued that noise can bias normal mode measurements toward lower attenuation values by up to 5-10%, Masters & Laske (1997) pointed to difficulties in choosing an appropriate time window for long-period surface waves as a reason for favoring normal mode measurements. A more recent

study by Roult & Clévédé (2000) based on a detailed analysis of measurement techniques and associated errors argues that the normal mode measurements are the more reliable. Yet, their analysis is far from being complete (Romanowicz and Mitchell, 2007), and the question of which set of measurements is more representative of the Earth's attenuation remains open. The compilation of attenuation measurements used in this study (Masters, personal communication) relies on careful windowing and a multi-taper approach in order to achieve a smooth transition from the normal mode values at lower frequencies to surface wave values at higher frequencies (see Fig. 1).

In light of the data uncertainties and the strong tradeoff between the depth and frequency dependence of attenuation, seismic studies routinely focus on modeling the depth-dependence of attenuation (e.g Anderson and Hart, 1978; Dziewonski and Anderson, 1981; Masters and Gilbert, 1983; Widmer et al., 1991; Durek and Ekström, 1996). In other words, they assume that, within the seismic band, α cannot be resolved and thus implicitly rely on the frequency-independent attenuation model of Kanamori & Anderson (1977). Anderson and Given (1982) created the only model of both the frequency and depth dependence of attenuation by relating them through a physical model of the underlying relaxation mechanisms. The exact nature of mantle relaxation processes is, however, still debated (e.g. Jackson and Anderson, 1970; Karato and Spetzler, 1990). In this paper, we develop and apply a new method based on the standard analysis of Backus & Gilbert (1970) that allows us to separate the effects of the radial q profile from those due to frequency dependence of q as described by α. Therefore, we are able to eliminate the tradeoffs present in previous

studies and to focus on determining α without having to construct a new radial q profile or a full absorption band model of attenuation in the mantle. Our method also makes it possible to move beyond the assumption of frequency-independent attenuation without relying on model-dependent physical constraints, as Anderson and Given, 1982 had done. In what follows, we carry out a suite of synthetic tests which explore the characteristics of the available attenuation measurements. We also attempt to extract α from available long-period seismic attenuation data.

2.2 Method

We here modify the standard analysis of the resolution provided by a set of measurements (Backus and Gilbert, 1970), which has been recently applied to the study of radial density resolution within the Earth (Masters and Gubbins, 2003). Our goal is to adapt this analysis in order to extract the signal of frequency dependence of seismic attenuation.

We can relate a mode attenuation measurement q to material properties within the Earth via sensitivity (Fréchet) kernels K_μ and K_κ (e.g. Dahlen and Tromp, 1998):

$$q = \int_0^R dr \, \left(\kappa_0 q_\kappa K_\kappa + \mu_0 q_\mu K_\mu \right), \tag{2.1}$$

where R is the radius of the Earth, κ_0 and μ_0 are the reference radial profiles of bulk and

shear moduli, and q_κ and q_μ are values of radial bulk and shear attenuation. In this study we use either PREM (Dziewonski and Anderson, 1981) or ak135 (Kennett et al., 1995) as the elastic, and QL6 (Durek and Ekström, 1996) or QM1 (Widmer et al., 1991) as the attenuation reference profiles . We calculate the relevant frequencies of oscillation and sensitivity kernels K_μ and K_κ using a modified MINOS (Woodhouse, 1998) code (Capdeville, personal communication). The results of our analysis are valid insofar as the deviations of q from the reference profile remain sufficiently small to not affect the kernels themselves.

All the quantities in the integrand of Eq. (2.1) are functions of radius. We proceed to discretize them with respect to radius, so that they can be written in vector form, e.g. $K_\mu(r)$ becomes $\mathbf{K}_\mu$. For the frequency range considered in this study, we verify that the discretization is sufficiently dense.

It is important to observe that the sensitivity kernels of fundamental modes with similar frequencies are very similar. Therefore, existing q datasets are likely to be highly redundant (Masters and Gilbert, 1983). We seek to exploit this redundancy and divide modes into a low and high frequency bin, denoted by superscript l and h, respectively. Each linear combination of Fréchet kernels of modes in each bin defines a new "hyperkernel":

$$\mathbf{H}^{\text{low}}_{\mu,\kappa} = \sum_{l=1}^{N_l} \gamma^l \mathbf{K}_{\mu,\kappa}{}^l \quad \text{and} \quad \mathbf{H}^{\text{high}}_{\mu,\kappa} = \sum_{h=1}^{N_h} \gamma^h \mathbf{K}_{\mu,\kappa}{}^h, \tag{2.2}$$

where N_l and N_h are the number of modes in each bin, and the subscripts μ, κ denote that

the kernels refer to either shear or bulk attenuation. Though called averaging kernels by Backus and Gilbert (1970), we have dubbed them "hyperkernels" to stress their usefulness for separating the effects of the depth dependence of attenuation from its frequency dependence.

Each particular choice of γ^l and γ^h will yield hyperkernels with different depth sensitivities. Therefore, by requiring that γ^l and γ^h yield hyperkernels with identical sensitivities to the radial attenuation profile, it is possible to remove the trade-off between depth and frequency dependence of attenuation measurements. Since we focus on the effective α in the mantle, we also seek to eliminate the contamination from the inner core while averaging mantle structure. We do this by requiring the hyperkernels to be zero in the core while providing maximally uniform sensitivity in the mantle. In order to eliminate the contribution from poorly-constrained mantle bulk attenuation, we seek hyperkernels that are insensitive to q_κ. These three coupled constraints can be written as:

$$\mathbf{H}_\mu^{\text{high}} = \mathbf{H}_\mu^{\text{low}} \quad \text{and} \quad \mathbf{H}_\mu^{\text{high}} = \mathbf{H}_\mu^{\text{low}} = \mathbf{b} \quad \text{and} \quad \mathbf{H}_\kappa^{\text{low}} = \mathbf{H}_\kappa^{\text{high}} = 0 \tag{2.3}$$

where **b** is unity in the mantle and zero elsewhere. While the first constraint is paramount, the others cannot be satisfied exactly and require the introduction of a damping parameter, λ_1. In light of Eq. (2), we write these conditions in condensed matrix notation as $\mathbf{P} \cdot \Gamma = \mathbf{B}$

or as:

$$\begin{pmatrix} \mathbf{K}_{\mu}^{\mathbf{l}} & -\mathbf{K}_{\mu}^{\mathbf{h}} \\ \lambda_1 \mathbf{K}_{\mu}^{\mathbf{l}} & \mathbf{0} \\ \mathbf{0} & \lambda_1 \mathbf{K}_{\mu}^{\mathbf{h}} \\ \mathbf{K}_{\kappa}^{\mathbf{l}} & \mathbf{0} \\ \mathbf{0} & \mathbf{K}_{\kappa}^{\mathbf{h}} \end{pmatrix} \begin{pmatrix} \gamma^{\mathbf{l}} \\ \gamma^{\mathbf{h}} \end{pmatrix} = \begin{pmatrix} \mathbf{0} \\ \lambda_1 \mathbf{b} \\ \lambda_1 \mathbf{b} \\ \mathbf{0} \\ \mathbf{0} \end{pmatrix} \tag{2.4}$$

The damping parameter λ_1 allows us to select among all combinations of nearly-identical hyperkernels those that have zero sensitivity to q_κ and inner core q_μ. Ideally, our hyperkernels would only use modes whose attenuation measurements have the smallest published uncertainties. Therefore, we seek γ^l and γ^h that minimize the squared misfit:

$$S = \mathbf{B} - \mathbf{P} \cdot \Gamma + \lambda_2 \mathbf{V} \cdot \mathbf{I}, \tag{2.5}$$

where $\mathbf{V}$ is a vector containing published variances of the q measurements of individual modes in both bins, $[v^l, v^h]$, and λ_2 is a constant that sets the importance of the constraint on minimizing the resulting uncertainties.

To each hyperkernel corresponds a q value, which is a weighted average of the q measurements of its constituent normal modes:

$$q^{\text{low}} = \sum_{l=1}^{N_l} \gamma^l q^l \quad \text{and} \quad q^{\text{high}} = \sum_{l=1}^{N_h} \gamma^h q^h. \tag{2.6}$$

Furthermore, if we assume that the uncertainties in the attenuation measurements of the low- and high-frequency modes are uncorrelated, we can directly relate variances v ($v \equiv \sigma^2$) in the mode q measurements to uncertainties in q^{low} and q^{high} via

$$v^{\text{low}} = \sum_{h=1}^{N_l} \gamma^l v^l \gamma^l \quad \text{and} \quad v^{\text{high}} = \sum_{h=1}^{N_h} \gamma^h v^h \gamma^h. \tag{2.7}$$

Since the two hyperkernels have identical sensitivity to radial attenuation structure but differing frequency content, differences in q^{low} and q^{high} can be attributed to frequency dependence of attenuation. These effects of frequency dependence can be accounted for by projecting the individual mode q's to a reference value q_0 using:

$$q_{0_i} = q_i \left(\frac{\omega_i}{\omega_0} \right)^{\alpha}. \tag{2.8}$$

In the absence of systematic measurement error, q^{low} and q^{high} will be reconciled at the reference frequency for the value of α that corresponds to the effective α of the mantle. Note that this correction for the effects of frequency dependence must also be applied to variances $\mathbf{V}$, and therefore affects the misfit function and through it the retrieved coefficients, γ.

For each test value of α we can use the uncertainty on the q measurement of the hyperkernels (i.e. v^{low} and v^{high}) to calculate the probability that the q^{low} and q^{high} can be considered identical at the reference frequency. Since the q of each hyperkernel can be

represented by two Gaussian probability density functions (PDFs) with means q^{low} and q^{high} and variances v^{low} and v^{high}, we seek to calculate the likelihood that sample q values drawn at random from these two PDFs can be considered identical. The PDF that describes the difference between the two random samples is described by a Gaussian of mean $q^{low} - q^{high}$ and variance $v^{low} + v^{high}$. In addition to measurement uncertainty, the damping contributes to the uncertainties of q^{low} and q^{high} by preventing the two hyperkernels from being identical. We restrict this uncertainty to be small by requiring that the attenuation values predicted by the two hyperkernels for an identical radial attenuation profile are within 3% of one another. This is why we consider q^{low} and q^{high} to be reconciled by a test value of α if their difference is less than 3%. The value of 3% was found to be the most stringent value that could be satisfied for a large range of damping parameters.

Having calculated the probability that a trial α value reconciles q^{low} and q^{high}, we can proceed to conduct a search for an optimal value of α which would maximize this probability. For the particular choice of damping parameters λ_1, and λ_2 used in constructing the hyperkernels, this optimal α value is taken to be the measurement of effective mantle α.

2.3 Results

2.3.1 Method validation

Armed with a method which has the potential to separate the depth- and frequency-dependence of attenuation, we first proceed to quantify its α-resolving power. At the same time, we investigate whether the existing normal mode attenuation measurements are sufficiently numerous and precise for constraining α. To this end, we perform a series of synthetic tests in which we generate q values of modes whose attenuation has been measured. We assume the radial attenuation profile QL6 together with PREM elastic structure, because the QL6 model fits the Earth-orbiting surface waves better than the attenuation structure of PREM. We adopt a depth-invariant α value of 0.3 throughout the mantle and assume frequency independent attenuation, i.e. $\alpha = 0$, in the inner core. To each synthetic mode q we assign the same variance ν as that of the corresponding real measurement. Generated q's and the corresponding kernels $K_{\mu,\kappa}$ are then distributed within two distinct frequency bins. There are, of course, multiple choices for the frequency content of each bin. Tab. 1 specifies the frequency content and number of modes with available measurements for the four different binning schemes used in this study.

In order to find the most likely α value, we explore α values between -1 and +1 subject to a range of damping parameters λ_1 and λ_2 from 10^{-4} to 1 and from 10^{-6} to 10^{-2}, respectively. The values of λ_1 and λ_2 have to be small in order to ensure that the hyperkernels

	Low frequency bin			High frequency bin		
	Upper bound (s)	Lower bound (s)	Number of modes	Upper bound (s)	Lower bound (s)	Number of modes
A	3231	600	35	600	10	168
B	3231	700	26	700	500	23
C	700	500	23	400	200	70
D	400	200	70	200	10	58

Table 2.1: The four choices of upper and lower bounds on high and low frequency bins used in this study. For each bin, the number of modes with available measurements is also listed.

have identical shape. Fig. 2 (top row) shows the retrieved effective α for the four different binning schemes (labeled from A to D), with warm colors indicating higher probabilities than the cool colors. For all binning choices, the greatest likelihood is in excellent agreement with the initial value of α regardless of the value assigned to the damping parameter λ_2, which controls the resulting variance. We stress that the retrieved likelihoods are stable over a large range of damping parameters λ_1 and λ_2. Based on Fig. 2, we conclude that the number and precision of existing attenuation measurements are indeed sufficient to retrieve accurately the frequency-dependence of attenuation.

As expected, the uncertainty on the α measurement decreases as the variance damping λ_2 increases. But, values of λ_2 that are too large can result in significant differences between hyperkernels and contaminate the extracted value of α. Note that in the case of the choice D (high frequency bins), the uncertainty of the retrieved α is considerably larger than in the case when lower frequency modes are included. This is because the higher frequency overtone attenuation measurements are generally less precise than the measurements made

at lower frequencies. The blanked areas correspond to situations when the difference in the hyperkernels exceeded 3%.

The hyperkernels $\mathbf{H}_{\mu}^{\text{low}}$ and $\mathbf{H}_{\mu}^{\text{high}}$ corresponding to schemes A - D are plotted in Fig. 2. (bottom row). The hyperkernels are almost indistinguishable (the difference is less than 3%) and they vanish in the core. As for the hyperkernels $\mathbf{H}_{\kappa}^{\text{low}}$ and $\mathbf{H}_{\kappa}^{\text{high}}$, they remain negligible throughout the whole Earth. Peak of the sensitivity with depth reflects the frequency content of the corresponding binning schemes; while lower frequency modes sample the entire mantle (A and B), the higher frequency ones only sample shallower regions (C and D).

We have also tested other binning schemes (not listed in Tab. 1) and other values of input α, and our method consistently retrieves the correct α value. Changing the bounds of the frequency bins results in a different population of modes in each bin. As a result, the optimized hyperkernels may change as may the uncertainties on the α measurement. When the frequency contents of the two hyperkernels are made to be very different, the problem of finding a linear combination of mode sensitivities that will satisfy the three constraints of Eq. (3) becomes more difficult. At the same time, hyperkernels with frequency content that is too similar have difficulty resolving the effects of frequency dependence of attenuation, as observed in panel D of Fig. 2.

2.3.2 Effective α in the mantle

Having validated our approach, we apply our methods to the real q measurements. We use a compilation of original measurements and published data provided by (Masters, personal communication). Fig. 3 (top row) shows the retrieved α likelihoods for the same binning schemes listed in Tab. 1. The retrieved α likelihoods are characterized by strikingly different trends than those extracted from our synthetic tests that assumed a frequency- and depth-independent α. When all available measurements are used (binning scheme A), the most prominent characteristic is a systematic increase of retrieved α with increasing λ_2. Highest likelihoods are reached at a zero value of effective α in the mantle. Analysis of the lowest-frequency measurements (binning scheme B) accentuates this trend, while indicating a negative value of effective α. When modes of intermediate frequency are used (binning scheme C), the character of the retrieved α likelihoods changes significantly. The most likely effective α in this frequency range is 0.1, and is largely independent of the value of λ_2 . Moving onward to the highest available frequencies (binning scheme D), the most likely α values are positive, lingering around a value of 0.3, but suffering from large uncertainties.

These systematic changes in behavior of retrieved α are clearly incompatible with a constant α model, regardless of its absolute value. Therefore, neither the usual assumption of frequency-independent attenuation often used in seismology (e.g. Dziewonski and Anderson, 1981; Kanamori and Anderson, 1977), nor the constant non-zero α models suggested

by laboratory studies (Jackson et al., 2002), allow us to explain the observations. In fact, Fig. 3 strongly suggests that α varies with frequency within the absorption band. In particular, mantle α appears to be negative at periods longer than 1000s, transitioning to a small positive value in the period range $\sim$ 1000-700s, and increasing again at periods shorter than 500s. It is important to realize that noise in the attenuation measurements might introduce artifacts in the retrieved α signal. However, the observed systematic behavior is likely to be a robust feature.

Frequency dependence of α

In order to better constrain the variation of effective α with frequency, we perform a series of forward-modeling exercises. We start by allowing a single jump in α from negative to positive values, i.e. we assume that at long periods q increases with increasing frequency, while at short periods, q decreases with increasing frequency. We create several dozen trial models by varying the frequency position and magnitude of the jump. Each of these models is used to calculate a synthetic dataset, which is then analyzed in the same way as the actual measurements. We find that no model with a single jump in α is capable of capturing the complex character of the retrieved α shown in the top row of Fig. 3. Nevertheless, models in which α transitions from negative to positive in the $\sim$ 1000-400s period range reproduce the character observed in the data better than any constant α model.

Allowing for a more complex frequency-dependent character of α, we fashion a set of trial

models characterized by jumps in α at two different frequencies. Given uncertainties in the attenuation measurements and the possibly complex behavior of mantle α, no single model is likely to explain all the features present in Fig. 3 (top row). However, we find that a model in which α changes from a value of -0.4 at periods longer than 1000s, to a value of 0.1 in the period range 300-800s, before changing to 0.3 at periods shorter than 200s, reproduces well the overall features present in the data (see bottom row of Fig. 3). Our preferred model is shown in Fig. 4 and it is compared with laboratory studies and the frequency-independent assumption. In constructing the figure, we have assumed that the high-frequency corner occurs at 1 Hz where q^{-1} is 600 (Sipkin and Jordan, 1979), since our study constrained the value of α and not of q^{-1}. Of course, our preferred model of α should be viewed as an example of a set of possible models, which must share its distinguishing features: a negative α at periods longer than 1000s, and a positive and increasing α at shorter periods.

Depth dependence of α

In order to investigate possible depth-dependence of α, we have fashioned hundreds of models in which we allow α to vary with both frequency and depth. In these models, $\alpha = -1$ at periods longer than a prescribed critical period T_c, whereas it is allowed to take on values between 0.0 and 0.3 at periods shorter than T_c. We then allow T_c to vary between 1000s and 400s in three different regions of the mantle: the upper mantle, transition zone,

and lower mantle. None of the explored models fits the data as well as the preferred model shown in Fig. 4; they are particularly inadequate in capturing the character of the high-frequency data seen in panel D of Fig. 3. Nevertheless, the subset of the explored models that is capable of explaining the low frequency features (panels A, B and C of Fig. 3) has T_c = 1000s and $\alpha = 0.1$ at periods shorter than T_c at all depths.

Because of the shape of the hyperkernels used in this study, our method is only weakly sensitive to α and T_c values in thin layers, such as the transition zone and D". Indeed, because forward-modeling tests indicated that our sensitivity to the D" region was nearly negligible, we have not parameterized it as distinct from the lower mantle. This lack of sensitivity implies that even though none of the models in which T_c or α varied significantly with depth were able to reproduce the behavior observed in Fig. 3, we cannot rule out smaller variations in T_c, or even significant variations within thin layers such as D".

For completeness, one might consider models in which the value of α is the same below and above T_c, which corresponds to a model in which α varies with depth by not frequency. However, this class of models has not been considered as a plausible solution to explain the available attenuation measurements. Such a frequency-independent model would require negative α values across a wide range of frequencies in large sections of the mantle in order to match the characteristics observed in the top row of Fig. 3. Such behavior has been suggested by neither theoretical studies nor by experiments, and is thus highly unlikely.

We note that these results are robust across different reference Earth models. The character

of the retrieved α likelihoods remains largely unchanged when ak135 (Kennett et al., 1995) is used instead of PREM (Dziewonski and Anderson, 1981). Using the QM1 (Widmer et al., 1991) radial profile of attenuation instead of QL6 (Durek and Ekström, 1996) similarly only marginally affects the retrieved likelihoods, confirming the fact that our method allows us to constrain α independently of the radial attenuation profile. Of course, using inappropriate reference models can result in sensitivity kernels sufficiently different from those corresponding to the actual measurements to obliterate the sought-after α signal.

2.4 Discussion

We have devised a method capable of separating the frequency-dependence of attenuation from its depth-dependence. After validating our method on a synthetic dataset, we demonstrated that the number and precision of existing attenuation measurements are sufficient for constraining α. Applying the approach to actual attenuation measurements of free oscillations and surface waves spanning the period range 3200s-50s, we observed that effective α is likely to be frequency dependent. Specifically, α is negative at periods longer than 1000s and positive and increasing from ~ 0.1 to ~ 0.3 at shorter periods (see Fig. 4). This conclusion runs against both the assumption of frequency-independent attenuation often used in seismology, and the constant, positive α model suggested by laboratory studies (Jackson et al., 2005).

Having constrained α and its frequency dependence, we explored a large set of models in which α varied with both frequency and depth. Our tests were motivated by the expectation that α in the Earth depends on both frequency and depth, since the pressure- and temperature-dependence of the activation enthalpy of the relaxation mechanisms giving rise to the absorption band may induce a shift in its frequency extent with depth (Jackson and Anderson, 1970; Anderson and Minster, 1979; Minster and Anderson, 1981; Anderson and Given, 1982). Despite this expectation, we were unable to observe any significant variation of α with depth.

Our frequency-dependent model of α is physically plausible, and was suggested by the pioneering study of Anderson and Given (1982) who constructed a mantle attenuation model (ABM) in which the frequency location of the absorption band changed with depth. While the ABM predicted positive α values in the midmantle for all frequencies considered in our study, their upper and lowermost mantle regions were characterized by negative α values at periods longer than 1000s. This is consistent with our findings. Further direct comparisons between our preferred model and the ABM are not straightforward, since Anderson and Given (1982) modeled both the depth- and frequency-dependence of attenuation, whereas the novelty of our approach rests in its ability to constrain the frequency-dependence of attenuation independently of its radial profile. We have also re-analyzed the dataset used by Anderson and Given (1982) using our method, and found that the number and quality of the measurements available to them were insufficient for a reliable estimation of α. Indeed, Anderson and Given (1982) noted the lack of resolution of α and used only modes sensitive

to the mid-mantle in order to constrain its value at ~ 0.15. Both our novel approach and the dramatic improvement in the precision and number of available attenuation measurements - we use twice as many as were available a quarter-century ago - has made it possible to constrain the complex character of α in the mantle in a way that was unavailable when ABM was created.

In addition to being physically plausible, our preferred model of frequency dependence of attenuation is consistent with earlier studies that have relied upon body waves and have focused on higher frequencies (see Fig. 4). A number of studies (Ulug and Berckhemer, 1984; Cheng and Kennett, 2002) looking at S/P ratios at frequencies greater than 40mHz have argued for α values in the 0.1-0.6 range. Shito et al. (2004) used continuous P-wave spectra to constrain α between 0.2-0.4 at periods shorter than 12s, while Flanagan and Wiens (1998) found that an α value of 0.1-0.3 was needed to reconcile attenuation measurements on sS/S and pP/P phase pairs in the Lau basin. Unlike these studies, however, our model of α relies upon data that provide more uniform global coverage, and, therefore, ought to more closely approximate the α representative of the average mantle.

A non-zero value of α carries important implications for the construction of radial profiles of attenuation. Efforts at determining the radial profile of attenuation in the Earth have routinely assumed that attenuation is frequency independent (e.g. Dziewonski and Anderson, 1981; Durek and Ekström, 1996). The resulting models have, therefore, mapped the signal of frequency-dependence of q into its depth profile. The extent to which neglecting

the frequency-dependence of α contaminates the true depth profiles of q can be probed by comparing the magnitude of the variation in measured values of q to the variation expected for different values of α. Such a comparison is attempted in Fig. 5, which shows the effects that α can have on attenuation measurements; for our preferred model, the effects of α on attenuation can be very significant. Therefore, we expect that the existing radial profiles of attenuation are likely to be contaminated, and that they should not be used as-is to constrain the thermochemical state of the Earth's interior. Nevertheless, if these models are to be used solely for modeling the effects of Earth structure on seismic waves, then mapping the frequency dependence of attenuation into its radial profile is not a problem.

The dependence of intrinsic attenuation on temperature can be described by the following expression (e.g. Romanowicz and Mitchell, 2007):

$$q \propto \omega^{-\alpha} exp\left(-\alpha H/RT\right) \tag{2.9}$$

where H is the activation enthalpy, R is the gas constant, and T is the temperature. The value of α, then, determines the functional form of $\delta q/\delta T$. When α is zero, $\delta q/\delta T$ is independent of temperature, whereas when α is positive, $\delta q/\delta T$ is exponentially dependent on temperature (Minster and Anderson, 1981). Recent studies seeking to constrain lateral attenuation variations rely on data with periods shorter than $\sim$ 300s (e.g. Gung and Romanowicz, 2004). At these periods, our preferred model suggests a positive α value close

to 0.3. This value implies an exponential temperature dependence of attenuation, and justifies the interpretation of lateral attenuation variations in terms of temperature variations. Note that the amplitude of lateral temperature variations necessary to obtain the observed q signal are therefore smaller than would be in the case of frequency-independent attenuation. Similarly, a positive α value affects the anelastic correction to the velocity-temperature relationships that need to be used when interpreting the lateral seismic velocity variations (Romanowicz, 1994; Matas and Bukowinski, 2007).

Intrinsic attenuation causes dispersion of seismic velocities, decreasing the velocities of longer period waves compared to shorter period ones. Properly correcting for the dispersion effect is crucial when datasets with different frequency content are used to simultaneously constrain velocities in the Earth (Kanamori and Anderson, 1977). Usually, the difference in wave-speeds due to an attenuation value q at two frequencies $\omega_{1,2}$ is calculated using the expression

$$\frac{V(\omega_2)}{V(\omega_1)} = 1 + \frac{q}{\pi} ln\left(\frac{\omega_2}{\omega_1}\right), \tag{2.10}$$

which is only valid when $\alpha = 0$. However, non-zero values of α , as suggested by this study, require the use of a different dispersion correction (Anderson and Minster, 1979; Minster and Anderson, 1981)

$$\frac{V(\omega_2)}{V(\omega_1)} = 1 + \frac{q(\omega_1)}{2} cot\left(\frac{\alpha\pi}{2}\right)\left[1 - \left(\frac{\omega_1}{\omega_2}\right)^{\alpha}\right] \tag{2.11}$$

We can see from this expression that the values of α and $q(\omega_1)$ will significantly affect the magnitude of the dispersion correction. The relative difference between these two expressions, though, is independent of q. For an α value of 0.3, the assumption of frequency-independent attenuation will result in 25% error for a frequency ratio of 10 and a 50% error for a frequency ratio of 100. Assuming that $\alpha = 0$ substantially overestimates the velocity dispersion, as pointed out by Anderson and Minster (1979) and results in differences that are not negligible when compared to those between different models of Earth's 1D velocity structure (see Fig. 6). Indeed, the effect of non-zero α can be larger than the correction applied to seismic velocities measured at high frequencies using spectroscopic laboratory methods. We note that Eq. (10) is valid for frequency-independent α. When α varies within the frequency range over which the dispersion correction is applied (i.e. ω_1 to ω_2), Eq. (10) should be applied separately to each domain of constant α.

Finally, the precise knowledge of seismic velocity, its dispersion and associated attenuation is important for meaningful comparisons with other geophysical observables, such as the geoid (e.g. Romanowicz, 1990). For example, estimations of viscosity of the lower mantle are based on values of $R_{s,\rho} = \partial V_s / \partial \rho$ parameter that (e.g. Richards and Hager, 1984; Ricard et al., 1993) do not include the anelastic effects. Matas & Bukowinski (2007) showed that anelasticity may significantly affect the value of $R_{s,\rho}$ and $R_{p,\rho}$, but pointed out that a more precise knowledge of the absorption band and its characteristics is still needed. Future work should thus be aimed at improving the precision of q measurements and the development of radial q profiles that properly account for the frequency dependence of q.

Acknowledgments

This project was supported by the National Science Foundation (through NSF grants EAR-0336951 and EAR-0738284) and by French CNRS-SEDIT program during the stay of JM at University of California, Berkeley. VL acknowledges supported through a Graduate Research Fellowship from the National Science Foundation. We wish to thank Guy Masters for kindly providing us his attenuation measurement compilation and, along with Mark S.T. Bukowinski, for inspiring discussions that helped improve the manuscript. This is Berkeley Seismological Laboratory contribution no. 09-05.

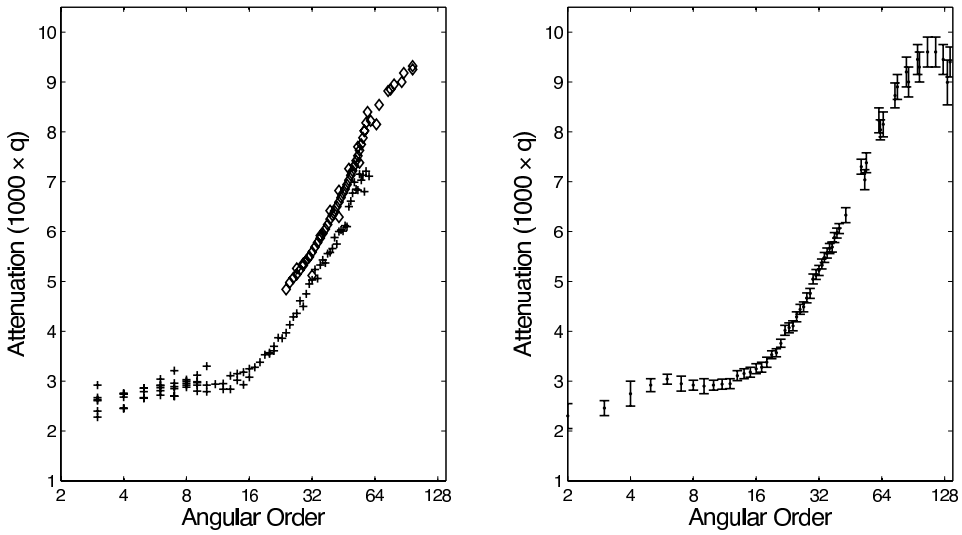

Figure 2.1: Left: Attenuation measurements for the spheroidal fundamental mode branch (compilation from http://mahi.ucsd.edu/Gabi/rem.html). Measurements based on normal mode analysis (plusses) show attenuation values 15-20% smaller than corresponding surface-wave-based measurements (circles). Right: The data compilation used in this study (Masters, *personal communication*) transitions smoothly from values more consistent with normal mode analyses at low frequencies to values consistent with surface wave analyses at higher frequencies.

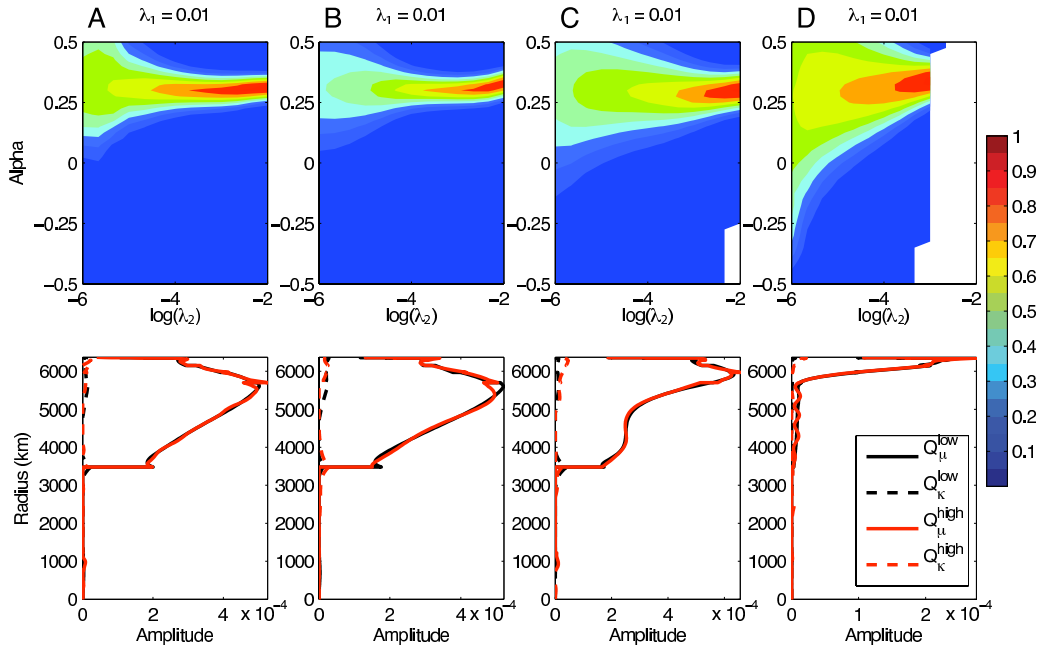

Figure 2.2: Top row: The retrieved α likelihoods for a synthetic dataset with input $\alpha = 0.3$ for the four different binning schemes (A,B,C,D) detailed in Tab. 1. Warm colors indicate greater likelihoods than cool colors. The retrieved α is in excellent agreement with the input value, and it is independent of λ_2. Bottom row: The hyperkernels associated with the four binning schemes for $\lambda_1 = 0.01$ and $\lambda_2 = 4 \cdot 10^{-4}$. $H_{\kappa}^{low,high}$ are nearly zero everywhere in the Earth, and $H_{\mu}^{low,high}$ have no sensitivity to inner core structure and nearly identical sensitivity in the mantle.

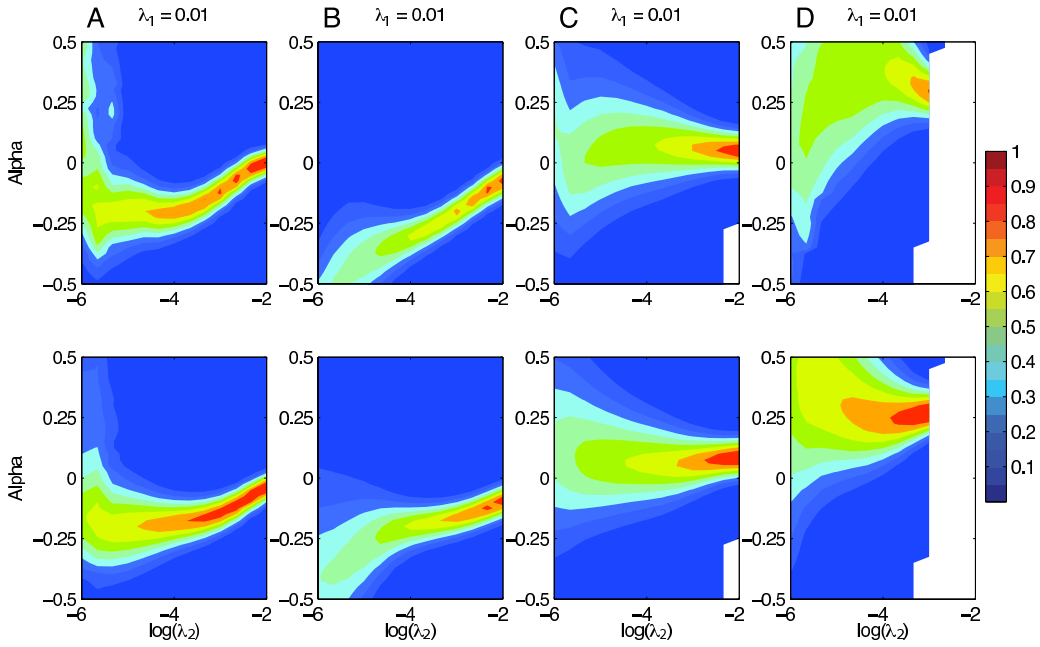

Figure 2.3: Top row: The retrieved α likelihoods for actual attenuation measurements binned according to the four different schemes (A,B,C,D) listed in Tab. 1. Warm colors indicate greater likelihoods than do cool colors. Bottom row: Similar overall behavior is obtained from synthetic q values generated using our preferred model of frequency-dependent q (see text).

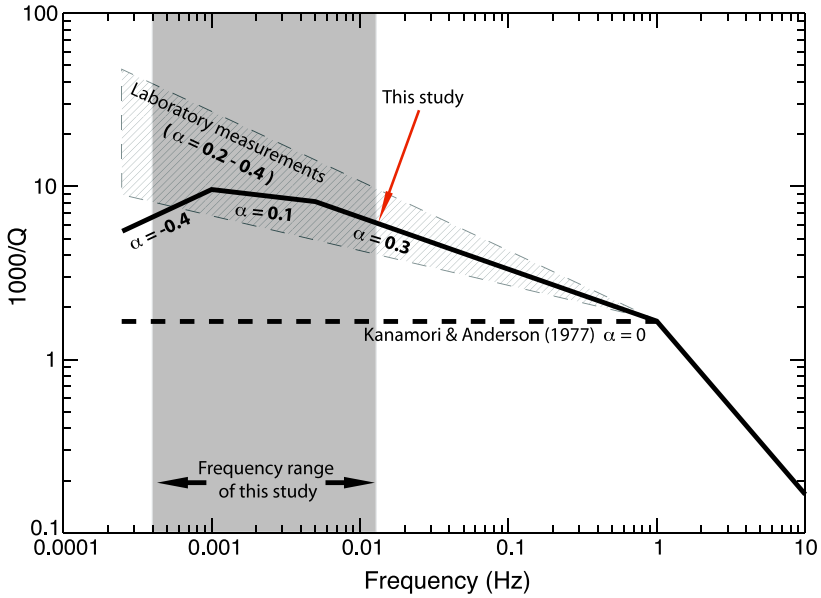

Figure 2.4: Preferred model (solid line) of frequency dependence of attenuation within the absorption band compared with constraints from laboratory studies (hachured region) and the frequency-independent assumption (dashed line). In our model, α is approximately 0.3 at periods shorter than 200 s, decreasing to 0.1 in the period range 300-800s, and becoming negative (-0.4) at periods longer than 1000s. We assume that the high-frequency corner occurs at 1 Hz where q^{-1} is 600, past which frequency α is 1 (Sipkin and Jordan, 1979). It is important to emphesize that we constrain the value of α and not of q^{-1}.

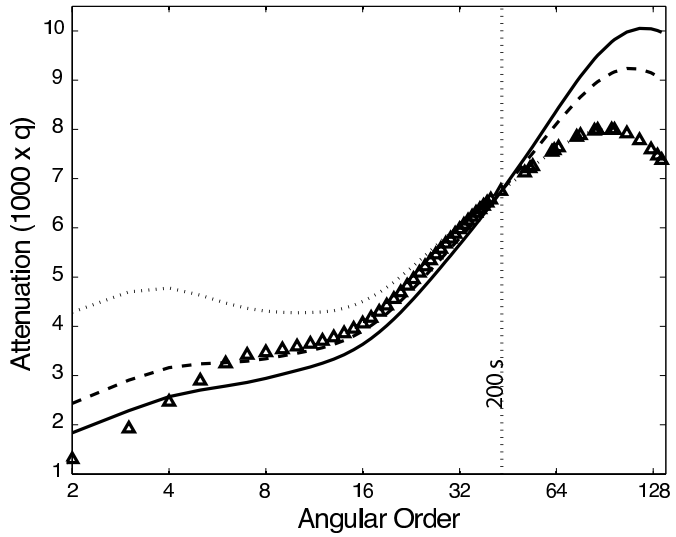

Figure 2.5: The effect of α on attenuation measurements can be significant. The solid line represents the attenuation values predicted by QL6. If we consider these predictions as representative of the q structure at a period of 200s, then values of α of 0.1 and 0.3 would result in q values indicated by the dashed and dotted lines, respectively. The effect obtained in the same fashion but using our preferred model of α is delineated by triangles. Note that the signal of frequency-dependence of attenuation can be significantly larger than the discrepancies between the normal mode and surface wave measurements shown in Fig. 1.

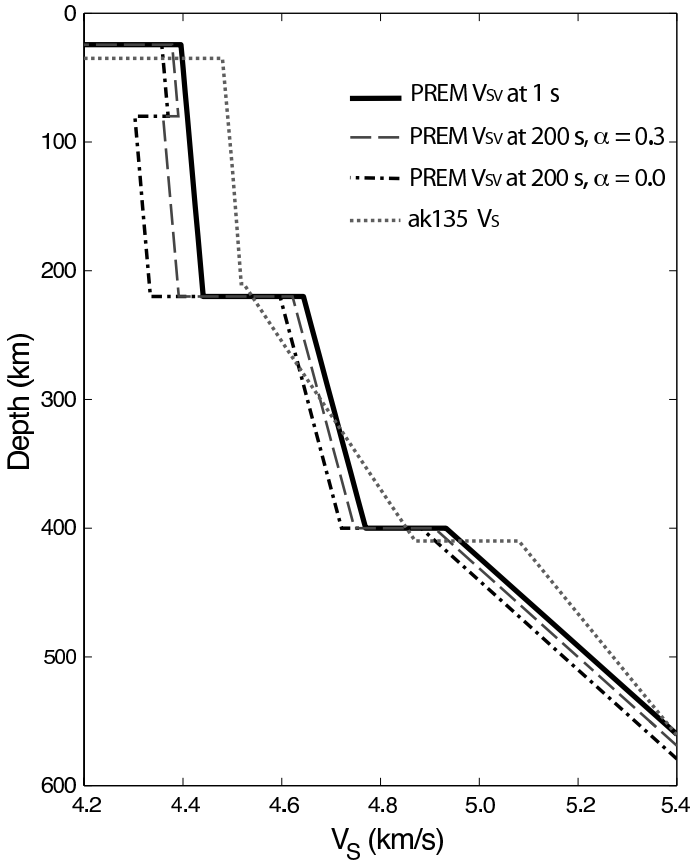

Figure 2.6: Accounting for the effects of frequency-dependence of attenuation is crucial for velocity dispersion corrections. The solid line represents the V_{SV} profile of PREM in the top 600 km of the mantle at the reference period of 1s. By taking the PREM shear attenuation structure to be appropriate at 200s (since it is derived from normal mode attenuation measurements) and a value of α, we can account for velocity dispersion due to attenuation. We calculate V_{SV} at a reference period of 200s using $\alpha = 0$ (dash-dotted line) and $\alpha = 0.3$ (long-dashed line). Assuming that $\alpha = 0$ substantially overestimates the velocity dispersion, as pointed out by Anderson and Minster (1979). The difference between the profiles with different α values are similar in magnitude to those between different models of Earth's 1D velocity structure, such as ak135 (dotted line) and PREM.

Chapter 3

Crustal effects in mantle long period waveform tomography

3.1 Introduction

Recordings of surface waves and overtones provide unparalleled constraints on the structure of the Earth's crust (e.g. Meier et al., 2007), upper mantle (e.g. Montagner and Tanimoto, 1991), and transition zone (e.g. Ritsema et al., 2004). This is because they offer excellent global coverage, and are sensitive to elastic and anelastic structure in both the crust and the mantle. Yet, in order to determine the seismic velocities and anisotropy in the mantle, we must disentangle the effects of the crust from those due to the sought-after

mantle structure. The ability of crustal effects to significantly affect retrieved models of mantle velocities, even at long periods and on large scales, was recognised as early as the pioneering work of Woodhouse and Dziewonski (1984). Accounting for the effects of crustal structure requires knowing the velocity structure of the crust as well as accurately calculating the effects of that structure on surface waves and overtones.

A number of efforts at determining the elastic structure of the crust have been carried out over the past decade. Global tomographers have typically relied on models of crustal structure derived from other datasets, such as refraction and reflection seismics, receiver functions and geological data, (e.g. 3SMAC: Nataf and Ricard, 1996; CRUST5.1: Mooney et al., 1998; CRUST2.0: Bassin and Masters, 2000), in order to predict and correct for crustal effects. More recently, global and regional crustal thickness and velocity models derived solely from surface wave data have been developed (e.g. Meier et al., 2007; Pasyanos, 2005).

Yet, since accurately modeling the effects of the crust on waves can be difficult, improved maps of crustal structure do not automatically translate into improved corrections for crustal effects. Within a normal mode formalism, which is useful for constructing and analysing long period waveforms, the effects of heterogeneity on waveforms can be expressed as shifts to the Earth's eigenfrequencies, as well as the displacement field (eigenfunction) associated with each vibrational mode. Woodhouse and Dziewonski (1984) applied linear corrections, in which eigenfrequency shifts due to crustal structure are calculated in a 1D

model, but the perturbations to the eigenfunctions are neglected, in order to remove the effect of the ocean/continent crustal dichotomy from long period waveforms. Due to their minimal computational costs, linear corrections have found widespread use (e.g. Chevrot and Zhao, 2007; Gu et al., 2003). Li and Romanowicz (1996) went one step beyond simply performing linear crustal corrections by allowing perturbations to the Mohorovičić (Moho) depth in the inversion, which partially accounted for umodelled crustal effects.

However, variations in crustal thickness are often too large to be accurately handled by linear corrections. In particular, the large differences in Moho depth between platforms, shields, orogens, continental margins, and ocean basins, change the shape of the eigenfunctions, thereby affecting the eigenfrequencies in a significantly non-linear fashion (Montagner and Jobert, 1988). In order to account for this non-linearity, Montagner and Jobert (1988) proposed a two-step approach in which the eigenfunctions and eigenfrequencies are calculated exactly for a set of tectonic settings (thereby capturing the non-linear effects), while perturbations away from these canonical 1D profiles are handled using linear corrections. This approach has recently been implemented in full-waveform analyses by Marone and Romanowicz (2007). Two global shear-wave speed and radial anisotropic models (Panning and Romanowicz, 2006; Kustowski et al., 2008) have been developed using these non-linear crustal corrections. A similar approach, in which phase perturbations are calculated exactly at each point along the raypath was implemented for fundamental-mode surface waves by Boschi and Ekström (2002). It is important to note that these approaches, while capturing some of the non-linearity associated with wave propagation through a heteroge-

neous crust, fail to explicitly take into account 3D finite-frequency effects calculated for the relevant 3D crustal model. Furthermore, when applied to higher modes and to high frequencies, they can be very computationally expensive.

Here, we present an alternative method for performing crustal corrections. Like the aforementioned methods, we calculate exactly the eigenfunctions and eigenfrequencies for a set of tectonic settings, but instead of using these directly, we solve for scaling coefficients, which, when applied to standard linear crustal corrections, mimic the non-linear effect. The main advantage of this approach is that, once the correction factors have been calculated, it requires no additional computational costs aside from those associated with linear corrections. This allows it to be more easily applied to overtones and to higher frequencies than the standard quasi-non-linear approach.

We then proceed to validate our approach using a synthetic dataset generated using the Coupled Spectral Element Method (Capdeville et al., 2003). First, we quantify the contamination of mantle models developed using full-waveform inversion that can result from the use of standard linear crustal corrections. Then, we demonstrate that our modified linear correction method effectively suppresses this contamination. Our approach for quantifying mantle contamination arising from crustal corrections is similar to that of Bozdağ and Trampert (2008) who undertook a thorough analysis of crustal effects on phase velocities of surface waves. Unlike that study, however, we model the complete seismic waveform in order to not discard amplitude information. Also, our use of finite-frequency kernels in the

vertical plane allows us to investigate crustal effects on overtones, which were not analyzed by Bozdağ and Trampert (2008).

3.2 Theoretical background

In this study, waveform modelling is accomplished within a normal mode formalism, which lends itself to constructing and analysing long period waveforms. Within this formalism, an acceleration time-series is represented as a summation of the contributions of a set of discrete, orthonormal modes of oscillation, each vibrating at a frequency ω_k:

$$u(t) = \sum_k A_k exp(i\omega_k t) \tag{3.1}$$

The modes' displacement field is represented radially by a set functions identified by index n, and laterally by spherical harmonics of degree l and order m. For convenience, we will use the index k to identify a mode defined by indices (n,l,m). The eigenfrequencies and eigenfunctions for a given 1D Earth model can be calculated using computationally efficient codes such as MINEOS (Woodhouse, 1998). The $2l+1$ modes with the same l and n are collectively referred to as a multiplet, and in a spherically symmetric model, they all have the same frequency. Source excitation and receiver orientation are represented by A_k, and the expressions for its constituent parts can be found in Woodhouse and Girnius

(1982).

First order perturbation theory can be used to account for effects of non-spherically-symmetric structure (e.g. Woodhouse and Dahlen, 1978). In this approach, 3D structure perturbs the frequencies of modes within a multiplet (called splitting), and couples energy within and between multiplets of similar frequency. Calculating the coupling between all possible pairs of modes can be computationally very expensive, so additional approximations have been used in order to make the problem computationally tractable.

Romanowicz (1987) showed that considering coupling along a single mode branch (all l and m for a given n) is, for large l, equivalent to accounting for average radial structure (1D) along the great circle path from source to receiver. This coupling can be represented by introducing a correction factor $\delta\tilde{\omega}_k$ to ω_k in Equation 3.1, which quantity can be obtained by integrating along the great circle joining source and receiver the local frequency shifts $\delta\omega_k$ resulting from coupling within an individual multiple induced by 3D structure:

$$\delta\tilde{\omega}_k = \frac{1}{\Delta}\int_0^{\Delta} \delta\omega_k(s)ds, \tag{3.2}$$

where Δ is the epicentral distance.

This approach, first implemented by Woodhouse and Dziewonski (1984), is appropriately called the path average approximation (henceforth, PAVA). Expressing the frequency shifts in the exponential has the benefit of somewhat relaxing the short-time limitation of standard

first order perturbation theory by accounting for multiple forward scattering.

For the case relevant to this study, in which only the radii of discontinuities r_d in the Earth are perturbed by δr_d, local frequency shifts due to coupling within a multiplet can be calculated in a linear fashion through the use of sensitivity kernels H_k^d, the expressions for which can be found on pages 350-351 of Woodhouse and Dahlen (1978). Note that these kernels are calculated for the spherically symmetric reference model:

$$\delta\omega_k^2 \equiv 2\omega_k \delta\omega_k = \sum_d r_d^2 \delta r_d H_k^d. \tag{3.3}$$

While the path average approximation is highly successful at modeling fundamental mode surface waves, it fails to capture the depth dependent sensitivity of overtone branches (see Li and Romanowicz (1995)). That is why, when calculating the effects of Earth structure on overtones, we must consider coupling between multiplets k and k' across branches (different n's) (Li and Tanimoto, 1993). Doing this accounts for finite frequency effects of wave sensitivity within the plane defined by the great circle joining source with receiver. In this study, we rely on Non-linear Asymptotic Coupling Theory (NACT: Li and Romanowicz (1995)), which is an implementation of across-branch coupling that relies upon asymptotic expressions for spherical harmonics. In it, a linear correction term δu that captures the

effects of cross-branch coupling is added to Equation 3.1:

$$\delta u(t) = \sum_k \left[-itA_k \delta\tilde{\omega}_k + \sum_{k' \subset \Gamma_k} D_{kk'} A_{kk'} \right], \tag{3.4}$$

with

$$D_{kk'} = \frac{exp(i\tilde{\omega}_k t) - exp(i\tilde{\omega}_k t)}{(\omega_k + \omega_{k'})(\tilde{\omega}_k - \tilde{\omega}_{k'})}, \tag{3.5}$$

$A_{kk'}$ are the asymptotic forms of scattering integrals, and are given by:

$$A_{kk'} = \frac{1}{2\pi} \int_0^{2\pi} \delta\omega_{kk'}^2 \left[Q_{kk'}^{(1)} cos(j\phi) + Q_{kk'}^{(2)} sin(j\phi) \right] d\phi, \tag{3.6}$$

where $j \equiv l - l'$ and the expressions for $Q_{kk'}^{(1)}$ and $Q_{kk'}^{(2)}$ can be found in Appendix A of Li and Romanowicz (1995).

Now, the local frequency shifts $\delta\omega_{kk'}^2$ account for coupling of multiplet k' with multiplet k that is induced by heterogeneity,

$$\delta\omega_{kk'}^2 \equiv 2\omega_{kk'}\delta\omega_{kk'} \equiv (\omega_k + \omega_{k'})\delta\omega_{kk'} = \sum_d r_d^2 \delta r_d H_{kk'}^d \tag{3.7}$$

and the kernels, $H_{kk'}$ still refer to the spherically symmetric reference model, and can be found in Appendix C of Li and Romanowicz (1996). For more details, see Romanowicz et al. (2008).

3.3 Standard Linear Crustal Corrections

We note that regardless of how PAVA and NACT incorporate the frequency shifts $\delta\omega$ that arise from 3D heterogeneity, they allow for these frequency shifts to be calculated in either a linear way, as used by Woodhouse and Dziewonski (1984), or a non-linear one proposed by Montagner and Jobert (1988). In the linear approach, we calculate $\delta\omega_k$ and $\delta\omega_{kk'}$ using Equations 3.3 and 3.7, with the kernels and discontinuity perturbations calculated for a single spherically symmetric model. In the non-linear approach, the local frequency shifts are calculated in a two-step approach. First, the eigenfrequencies (ω_k) of the relevant modes are calculated in one of a set of canonical models that most closely approximates the local radial velocity profile. This calculation captures the non-linearity of the local crustal effect on the eigenfrequencies. Then, the calculated frequency is modified using Equations 3 and 7, except that the kernels involved are calculated for the relevant canonical radial profile, and the discontinuity radius perturbations δr_d are taken with respect to this model as well. See Marone and Romanowicz (2007) for a more detailed explanation of this approach.

In order to quantify the inadequacy of linear crustal corrections, we divide the Earth's surface into 7 regions with similar crustal thicknesses and ocean depths. We base this regionalization on Moho depth, since it is the dominant parameter governing the seismic response of the crust at long periods. Starting with CRUST2 (Bassin and Masters, 2000), we identify 6 regions characterized by Moho depth ranges of 10-25 km, 25-40 km, 40-50 km, 50-60 km, and $>$60 km. In order to capture the strong effect of a shallow ($<$2 km)

Table 3.1: Physical parameters characterising the regions shown in Figure 3.1. Negative elevations are filled with ocean of density 1.02 g/cc and V_P 1.45 km/s.

Region	Elevation (km)	Moho depth (km)	Density (g/cc)	V_P (km/s)	V_S (km/s)
1	-3.00	9.67	2.86	5.95	3.14
2	-4.22	12.22	2.83	5.66	2.98
3	0.87	34.64	2.82	6.18	3.46
4	0.54	42.60	2.87	6.27	3.52
5	2.82	54.73	2.86	6.35	3.60
6	4.08	64.57	2.88	6.42	3.66
7	-0.80	25.76	2.82	5.71	3.11

ocean layer that characterizes the continental shelves, we introduce a seventh region. Figure 3.1 maps out the geographical extents of the 7 regions. For each region, we calculate an average radial profile of density (ρ) and shear (V_S) and compressional (V_P) wave velocity. The parameters characterising these profiles are shown in Table 3.3. Armed with a set of radial models that define 7 canonical crustal types, we proceed to calculate the frequencies ω_k of the fundamental modes for each model. These frequencies are then compared with those for PREM, and frequency shifts between PREM and each of the 7 regional models are calculated as

$$\delta\omega_k^{NL} = \omega_k^{(i)} - \omega_k^{PREM}, \tag{3.8}$$

where ω_k^i represents the frequency of mode k in the canonical crustal model i. Since these frequency shifts capture some of the non-linear effects of crustal structure, we identify them with a superscript *NL*.

For each canonical crustal model, we can calculate the kernels H_k^d that, through Equation 3.3, relate perturbations in the radii of discontinuities with the resulting frequency shifts

$\delta\omega_k$ of mode k. Note that these kernels only capture the effects of coupling within a multiplet. Figure 3.2 shows how sensitivity of fundamental modes to Moho depth and surface topography vary as a function of mode frequency. Similarly, Figure 3.3 shows the average sensitivities of modes in the first five overtone branches. Note that the basic assumption that underlies standard linear corrections is that discontinuity kernels for different crustal types do not appreciably differ from those of the reference model.

Even a cursory examination of the curves shown in Figure 3.2 shows that non-linear effects of surface and Moho topography on fundamental modes dominate at frequencies above 15 mHz. A comparison of the magnitude of the kernels for spheroidal and toroidal modes confirms the well-known fact (Dahlen and Tromp, 1998) that toroidal modes are significantly more sensitive to crustal structure than are spheroidal modes. A number of differences between the sensitivity curves indicate that the non-linearity of crustal effects can be non-intuitive. For spheroidal modes, oceanic models with thin crusts are associated with greatest sensitivities to Moho depth. At frequencies higher than 25 mHz, however, a continental-type model takes the lead. For toroidal modes, the story is entirely different, with models with intermediate crustal thicknesses being associated with larger sensitivities to Moho depth than either thin-crust oceanic models or thick crust continental ones. Other examples abound. For instance, note the change in concavity of H^S_{topo} between crustal types 4 and 5, whose crustal thicknesses differ by 12 km. Finally, we point out that for toroidal modes, both surface and Moho kernels are more similar between models 1 and 6, than they are between 6 and 4, even though differences in crustal structure are far larger between 1

and 6. In short, the condition that discontinuity kernels for different crustal types do not appreciably change is violated even at long periods.

Though the first five overtone branches are significantly less sensitive to topography and Moho depth, Figure 3.3 shows that non-linear effects of crustal structure become significant at frequencies higher than $\sim$ 15 mHz. As is the case with the fundamental mode branch, overtones show a number of interesting non-linear effects. For instance, even though toroidal modes are far more sensitive to Moho depth in oceanic models, they are less sensitive to it in PREM than in continental models. This is likely due to the fact that the crust in PREM has two layers, while those of our canonical models have only one. The behavior of spheroidal modes' sensitivities can also be counter-intuitive. First, unlike toroidal modes, spheroidal modes are more sensitive to topography and Moho depth in continental models than in oceanic ones. In fact, spheroidal mode frequencies are several times more sensitive to discontinuity topography in continental, thick-crust models than they are in thin-crust, oceanic models. Interestingly, in models with thick continental crust, the sensitivity of spheroidal modes to discontinuity topography starts to decrease at frequencies above $\sim$ 28 mHz. Thus, even for overtones, non-linear effects of crustal structure cannot be neglected.

We can use discontinuity kernels calculated for the reference spherically symmetric model, in this case PREM, to predict the effect of the canonical crustal structures on the normal mode frequencies. To do this, we only consider the differences in the radii of the discon-

tinuities between each canonical crustal model and PREM, neglecting the differences in crustal velocities and density. This is an often used approximation of the true linear crustal effect, and is appropriate because crustal velocities have been shown to have minimal effect on long period waves (e.g. Stutzmann and Montagner, 1994). Since the discontinuity perturbations characterizing each canonical model are spherically symmetric (degree zero spherical harmonic), they cannot give rise to coupling of energy between multiplets within a dispersion branch (Dahlen and Tromp, 1998 pg. 652). As a result, considering coupling within a multiplet is sufficient to accurately model fundamental mode surface waves, and is likely to adequately model overtones as well, since coupling across branches is small, being restricted to only modes with the same l. Therefore, we only consider coupling within a multiplet and use Equation 3 instead of Equation 7 for calculating the frequency shifts. We label the frequency shifts calculated in this standard linear approach $\delta\omega_k^{SL}$. The dotted lines in Figures 3.4 and 3.5 show the $\delta\omega_k^{SL}$ for fundamental modes and overtones and each of the canonical crustal structures. A comparison of these approximate terms with the $\delta\omega_k^{NL}$ calculated before (and displayed as solid lines) confirms that linear crustal corrections are inadequate for both fundamental modes and overtones, even at long periods.

3.4 An effective modification

As illustrated in Figures 2-5, standard linear crustal corrections are not successful at accounting for the effects of variations in crustal and ocean thickness on surface waves and overtones, even at periods as long as 100 sec. Therefore, we are interested in ways of correcting the $\delta\omega_k^{SL}$ so that they better track $\delta\omega_k^{NL}$. In order to accomplish this task, we are confronted with a crucial choice.

We must decide which term or terms in Equation 3.3 to correct. Correcting H_k^d for each crustal type is a natural choice, since the problem itself is inaccuracy of the linear corrections, rather than the topography of discontinuities. However, since H_k^d needs to be calculated for each mode, and in the case of cross-branch coupling, between pairs of modes, correcting this term can be computationally expensive. Note that non-linear corrections require changing H_k^d. Correcting δr_d, on the other hand, does not increase computational costs, since reading one value of δr_d is just as computationally expensive as reading a modified value. The problem with correcting only δr_d, of course, is that it is but a single parameter for a given discontinuity, crustal type, and mode type. Nevertheless, the fact that deviations between $\delta\omega_k^{NL}$ and $\delta\omega_k^{SL}$ change gradually with frequency (see Figure 3.4) gives us hope that modifying δr_d might significantly improve the accuracy of $\delta\omega_k^{SL}$.

We start the procedure by rewriting Equation 3.3 in matrix notation, where we only consider N fundamental modes and identify perturbations relating to the Moho with a subscript m

and those pertaining to the surface with t:

$$\begin{pmatrix} \delta\omega_1^{SL} \\ \delta\omega_2^{SL} \\ \vdots \\ \delta\omega_N^{SL} \end{pmatrix} = \begin{pmatrix} r_m H_1^m & r_t H_1^t \\ r_m H_2^m & r_t H_2^t \\ \vdots & \vdots \\ r_m H_N^m & r_t H_N^t \end{pmatrix} \begin{pmatrix} \delta r_m \\ \delta r_t \end{pmatrix} \tag{3.9}$$

We attempt to improve standard linear corrections by introducing factors $c_{m,t}$, calculated for each canonical crustal type and mode type, that are added to $\delta r_{m,t}$ before being multiplied by the kernel matrix (relabeled **H**). Written in vector notation, we seek **c** that minimises:

$$\mathbf{w} - \mathbf{H}(\delta\mathbf{r_{m,t}} + \mathbf{c_{m,t}}), \tag{3.10}$$

where the vector **w** contains the non-linear frequency shifts $\delta\omega_k^{NL}$. The least-squares solution to this minimisation problem is given by:

$$\mathbf{c_{m,t}} = (\mathbf{H'H})^{-1}\mathbf{H'}(\mathbf{w} - \mathbf{H}\delta\mathbf{r_{m,t}}), \tag{3.11}$$

where the apostrophe indicates the transpose.

We could have introduced a multiplicative correction term, instead of the additive one described above. However, solving for such a term becomes unstable when the δr_d's are small. Given that discontinuity topography is likely to vary both above and below its depth

in the reference model, the accompanying zero-crossings of δr_d will have adverse effects.

Because the non-linearity of crustal effects depends strongly on both crustal and mode type, we perform the minimisation in Equation 3.11 separately for spheroidal and toroidal modes, for fundamental modes and overtones, and for each crustal type. Once the set of factors $\mathbf{c_{m,t}}$ appropriate for a given mode type are obtained, we modify the surface and Moho topography of CRUST2.0 at each point on the surface by the correction factor appropriate for the relevant crustal type (obtained from Figure 3.1). Therefore, the crustal type and correction factor information is fused into a single file that specifies a modified discontinuity topography for each mode type.

The dashed lines in Figures 3.4 and 3.5 show the frequency shifts predicted by our modified discontinuity radii for fundamental modes and overtones, respectively. Henceforth, we label them $\delta\omega_k^{CL}$. For the fundamental modes, the improvement in fit to $\delta\omega_k^{NL}$ is significant over a large frequency range. The fit for the overtones is less good, though still significantly better than that provided by standard linear corrections. When only long period waves ($T > 60s$) are considered, excellent agreement between $\delta\omega_k^{CL}$ and $\delta\omega_k^{NL}$ can even be achieved when only correcting the Moho topography. In the section that follows, we use uncorrected surface topography, modifying only the Moho radii.

3.5 method validation

Having devised a method for improving standard linear crustal corrections, we attempt to validate it by comparing its ability to predict crustal effects on waveforms against that of standard linear crustal corrections.

3.5.1 Application to a synthetic dataset

The advent of fully numerical global wave propagation codes, such as the coupled Spectral Element Method (cSEM Capdeville et al. (2003)), now allows accurate modelling of wave propagation through highly heterogeneous media such as the Earth's crust (e.g. Komatitsch and Tromp, 2002). This advance offers us the opportunity to quantify how well standard approximate techniques for treating crustal effects perform when applied to tomographic inversions based on waveform modelling.

To this end, we generate a synthetic dataset of long-period three-component waveforms for a set of 67 earthquakes selected from the global CMT catalog. We ensure a realistic station distribution by only using stations at which the waveforms observed from the actual earthquake are sufficiently well recorded that they would be used in our global tomographic inversions. For a more detailed description of the data-selection criteria, see Mégnin and Romanowicz (2000). Figure 3.6 shows the event and station distribution as well as raypath density of the synthetic dataset.

Our velocity model has a spherically symmetric velocity profile which is identical to PREM (Dziewonski and Anderson, 1981) below the 400 km discontinuity. At depths shallower than 400 km, the model is inverted to fit long-period waveforms starting from one of the physical reference models (Cammarano et al., 2005), which are calculated from a fixed composition (dry pyrolite) and a thermal profile using the elastic and anelastic properties of principal mantle minerals. The mantle model is radially anisotropic above 220 km, by the same amount as PREM. The crustal model has average crustal velocities and thicknesses from CRUST2.0 (Bassin and Masters, 2000) filtered by a 5.6^o Gaussian filter to avoid spatial aliasing by the SEM mesh. Topography from ETOPO1 (Amante and Eakins, 2008) is similarly filtered. Effects of the ocean, ellipticity, gravity, rotation and anelasticity are all accounted for. The synthetic seismograms have energy at periods between 60-400 sec, while earthquake source parameters are taken from the global CMT catalog.

3.5.2 Mantle contamination due to crustal structure

We start by expressing the Moho topography of CRUST2.0 and topography of ETOPO1 using a spherical spline expansion characterised by 642 knots and an average inter-knot spacing of 7.9^o (see Wang and Dahlen, 1995). We then use both standard and modified linear crustal corrections to predict the effects of the crust on the waveforms that make up our synthetic dataset.

Figure 3.7 shows a comparison of transverse-component accelerograms calculated using SEM and NACT with standard and modified linear corrections for the earthquake C032401C recorded at 8 stations. When standard linear corrections are used, large phase-shifts are apparent for long continental paths, and are especially large on the transverse component, since Love waves are more sensitive to crustal structure than are Rayleigh waves. For Rayleigh waves, phase-shifts and amplitude discrepancies are apparent, but are much smaller, since linear corrections are more accurate (see Figure 3.4). Waveforms predicted by our modified crustal corrections fit the SEM far better, and the improvement on continental paths is dramatic. Typically, the use of modified corrections for fundamental mode surface waves decreases the variance between SEM and NACT synthetics by $\sim 65\%$ on the transverse and $\sim 35-40\%$ on the radial and vertical components. When only overtone wavepackets are considered, modified linear crustal corrections reduce the variance by $\sim 30-40\%$ for all the components.

The NACT synthetics are used to correct the SEM synthetic waveforms for the crustal effects. Two sets of residuals are produced, one resulting from applying standard linear corrections, and the other from our modified method. These residuals, which would ideally be very small, are then inverted for mantle structure. The data are weighted by a diagonal covariance matrix which serves to equalise lateral sensitivity, as proposed by Li and Romanowicz (1996). The upper mantle is parameterised laterally with 642 spherical splines, and in depth by 5 cubic splines centred at depths of 24, 121, 221, 321, 471 km (see Mégnin and Romanowicz (2000)). At each point, we solve for two parameters - isotropic shear-

wave speed $V_S^2 = (2V_{SV}^2 + V_{SH}^2)/3$ and anisotropic parameter $\xi = V_{SH}^2/V_{SV}^2$ - and use scaling relations to obtain V_{PV}, V_{PH} and η, as in Panning and Romanowicz (2004). The inversion procedure is iterative and is stabilised by the introduction of an *a priori* model covariance matrix, as described in Tarantola and Valette (1982). Any retrieved mantle structure is interpreted as an artifact of unmodelled crustal structure, and will henceforth be referred to as contamination. Therefore, if the residuals efficiently map into mantle structure, then the inadequacies of crustal corrections can be expected to strongly contaminate existing mantle models. If, on the other hand, the residuals cannot be effectively modeled by mantle structure, then they are less likely to contaminate the mantle model.

Figure 3.8 shows variations of isotropic shear-wave speed obtained from the inversion of the residuals calculated using standard linear crustal corrections as well as our modified approach. Both fundamental mode and overtone wavepackets are used. The final model obtained with standard linear corrections explains a larger fraction of the starting variance in the residual seismograms than does the model obtained using modified corrections. This means that the inaccuracies of standard linear crustal corrections can be more easily modeled by mantle structure than the inaccuracies of the modified correction technique we propose; therefore, the use of standard linear corrections will contaminate mantle structure much more strongly than the use of modified method. For fundamental modes, the model obtained using standard linear corrections explains 64% of the residuals on the longitudinal, 76% on the transverse, and 80% on the vertical component, whereas the model obtained using modified corrections reduced the starting misfit by 44% for the longitudinal,

32% for the transverse and 70% for the vertical component. For overtones, the obtained model explains 47% of the misfit on the longitudinal, 42% on the transverse, and 57% on the vertical component. Interestingly, the model obtained from modified crustal correction residuals only marginally improved the fit to the overtones (ranging from no improvement on the transverse component to 14% on the vertical). This indicates that the correction factors succeeded in eliminating nearly all of the mantle contamination arising from the use of linear crustal corrections.

Anisotropic structure was held fixed during the first two iterations, and was allowed to vary in the final 2 iterations. At each step of the inversion process, a range of *a priori* model parameter variances was explored; small values muted, while large values amplified the amplitude of the retrieved structure. Misfits were calculated for all of the resulting models, and we chose a preferred a priori variance to be a compromise between achieving large variance reductions and keeping model size small. All parameters have a correlation lengthscale of 1000 km in the horizontal direction and 100 km in the vertical, which is similar to that imposed by the parameterisation itself. Regardless of *a priori* variances, the retrieved pattern of mantle contamination remained the same.

Note the strong tectonic character of the mantle contamination, which is seismically slow beneath continents, where standard linear crustal corrections under-predict the effects of crustal structure. In particular, anomalously slow regions underlying mountain ranges (e.g. North American Cordillera) appear down to 100 km depth. At greater depths, most of

the contamination is under the oceans, following the mid-ocean ridge systems, where the contamination is seismically fast. When modified linear corrections are used, we can see a significant reduction of contamination. In particular, amplitudes of contamination are reduced, especially at shallowest depths. Mantle beneath the North American Cordillera, for instance, is nearly free of contamination even at 40 km depth. Contamination beneath the oceans is effectively suppressed. In fact, the tectonic character of the contamination becomes less prominent, and less well-organised. It bears reminding that some of the remaining contamination might well result from the imperfect distribution of crossing paths afforded by our modest synthetic dataset.

The sensitivity kernels shown in Figure 3.2 show that the Love waves are significantly more sensitive to shallow layer structure than are Rayleigh waves. This fact, combined with other differences in the way that oceanic and continental crust affect Rayleigh and Love waves (see Bozdağ and Trampert (2008)), suggests that inadequacies in crustal modelling can map efficiently into mantle anisotropic structure. Indeed, our maps of lateral variations in ξ confirm this suspicion. Figure 3.9 shows the contamination of ξ that results from the use of standard and modified linear corrections. The maps shown are for the same model as in Figure 3.8.

When standard linear corrections are applied, we retrieve enhanced V_{SV} to V_{SH} ratios, indicated by warm colours in Figure 3.9, below both continents and oceans. Nevertheless, contamination is stronger beneath continents, and is particularly prominent beneath cra-

tons. Beneath Tibet, as well as the Canadian and Brazilian cratons, this contamination extends to 225 km depth. Structure beneath the oceans also shows anomalously high ξ that tracks along the mid-ocean ridge system; this signature peters out around 150 km depth. Our modified linear corrections are successful at suppressing contamination in all tectonic settings. In fact, signatures of all of the cratons except a small portion of the Brazilian craton are completely removed. Anomalous structure beneath Tibet becomes very weak as shallow as 100 km depth. Beneath oceans, no coherent contamination extends below 100 km depth.

Figures 3.8 and 3.9 attest to the ability of our modified linear corrections to minimise contamination of mantle isotropic and radially anisotropic structure that could result from the use of standard linear corrections. The success of our modifications is summarized in Fig. 3.10, which plots as a function of depth the variance reduction for both the Vs and ξ models resulting from the use of modified instead of modified linear corrections. We define the variance reduction at radius r as:

$$VR(r) = \int_{\theta}\int_{\phi} \frac{m^2_{slc}(r,\theta,\phi) - m^2_{mlc}(r,\theta,\phi)}{m^2_{slc}(r,\theta,\phi)} d\theta d\phi, \tag{3.12}$$

where $m(r,\theta,\phi)$ denotes the value of the model at location (r,θ,ϕ). At depths greater than 150 km, our modifications reduce the contamination of ξ mantle structure by more than half, and reduce by more than a third the contamination of isotropic structure at all depths.

3.5.3 Application to long period waveform data

Having demonstrated the potential of the proposed technique for reducing the contamination of mantle structure from unmodelled crustal effects, we proceed to apply the method to an actual waveform dataset used in the creation of the SAW642AN model of Panning and Romanowicz (2006, henceforth PR06). The dataset consists of three-component long period surface (T>60s) and body wave (T>30s) packets from 1191 events, and is detailed in Table 1 of PR06.

We employ identical data weighting and parameterization as that used in construction of SAW642AN. The primary difference is the removal of crustal effects via our modified linear corrections as opposed to the approximate, regionalized non-linear corrections used in PR06. We derive the final model after three iterations starting from SAW642AN. While we do not derive a specific set of modified linear corrections for body waves (and indeed, it is not obvious whether this approach, which does not take coupling between modes into account, would be appropriate for body wave data), we choose to correct the body wave data with the corrections derived for overtones, as it produces a better fit to the data than standard linear corrections. Regularization is chosen such that the final model size (as measured by the root-mean-squared amplitude of structure as a function of depth) closely matches that of SAW642AN for the isotropic portion of the model, and is matched or reduced in the anisotropic portion of the model.

The following two findings summarize the effects of the use of our modified linear crustal corrections on the retrieved mantle model: 1. The overall misfit to the data is reduced for all wavepacket types (fundamental modes, overtones, and body waves); and 2. the anti-correlation of upper and mid-mantle isotropic Vs structure present in SAW642AN is eliminated (see Fig. 11), bringing the model to closer agreement with other models of mantle shear wavespeed (e.g. Kustowski et al., 2008). While the improvement in fit is not extremely large (variance reduction of the final model with the modified linear corrections is 54.4% across all data types vs. 52.1% for SAW642AN using the regionalized non-linear corrections), it is important to note that the better fit is obtained with a model that is smaller in size, particularly in anisotropic structure, than the starting model. The detailed effects on the retrieved isotropic and anisotropic structure are more complicated and are discussed in a companion paper (Panning, Lekic and Romanowicz, in prep.), which also explores the effects of damping and quantifies model uncertainties.

3.6 Discussion

In this study, we have quantified the inadequacies of standard linear corrections in waveform tomography, and shown how crustal corrections can contaminate retrieved isotropic and anisotropic mantle structure to great depths. Our results have great bearing on recent efforts at validating existing tomographic models developed with approximate wave

propagation techniques using more accurate numerical approaches, such as SEM (e.g. Qin et al., 2009). In particular, since tomographic models of mantle structure were developed by predicting and correcting for the effects of crustal structure, they ought to be validated by using the same crustal corrections. Our work implies that implementing these crustal models in SEM is likely to result in very different crustal effects than those used to develop the mantle model. Since the effects of the crust are much larger for horizontally polarized shear waves, a straightforward crustal implementation in SEM is likely to find that models developed using horizontally polarized shear waves are less able to explain the observed waveforms than Vs models. Indeed, this is consistent with the findings of Qin et al. (2009).

We propose and validate a new method for improving linear crustal corrections. By considering a set of 7 crustal types, we quantify the inadequacy of standard linear corrections at accounting for the effects of the crust on the fundamental mode surface waves and overtones. Then, we improve the accuracy of linear corrections by introducing additive factors to the discontinuity topographies. Incorporating an additive correction factor to the discontinuity topography as opposed to the kernels results in no additional computation costs beyond those of standard linear corrections. The correction factors depend on the local crustal type, on the discontinuity considered, on the reference model used for calculating the sensitivity kernels, as well as mode type (spheroidal vs toroidal and fundamental vs overtone).

We use a synthetic dataset calculated using the Spectral Element Method for a 3D crustal

model and a 1D mantle to explore contamination that may result from inadequate crustal corrections. These tests show that the use of standard linear corrections can result in significant contamination of isotropic mantle structure down to depths of 150 km. In particular, at depths shallower than 100 km, mantle Vs beneath continents will be artificially reduced by the use of linear corrections; at greater depths, the oceanic ridges will appear artificially fast. Due to differences in crustal sensitivity of Rayleigh and Love waves, the effects on anisotropic structure are far more severe, and can potentially obliterate the mantle anisotropic signal in the upper 200 km. Our results confirm earlier findings of Bozdağ and Trampert (2008). When our modified linear corrections are applied to the SEM synthetics, much of the mantle contamination is removed. Contamination of isotropic Vs is eliminated below $\sim$ 75 km. The separate treatment of toroidal and spheroidal modes and fundamental modes and overtones proved to be highly successful in suppressing the contamination of radial anisotropy in the mantle.

We apply our new method for improving crustal corrections to the waveform dataset used to construct SAW642AN (Panning and Romanowicz, 2006). We find that the better treatment of crustal structure increases the fit to the data for all wavepacket types (body waves, surface waves and overtones alike). Furthermore, it eliminates anticorrelation between upper and mid mantle structure which distinguished SAW642AN from other global models of mantle shear wavespeed structure.

Our tests with the synthetic SEM dataset shows that the method improves the accuracy of

linear corrections equally well for fundamental modes as for overtones, though the total crustal signal is, unsurprisingly, far larger for the fundamental mode surface waves. Since the additive correction factors were calculated only accounting for coupling within multiplets, their success at modeling the true effects of crustal structure on overtones indicates that the non-linear crustal effects on multiplet-multiplet coupling are similar to those on coupling within a multiplet. This justifies our choice to neglect multiplet-multiplet coupling when calculating the additive correction factors.

The remaining inadequacies of our modified crustal corrections are likely due to off-path effects, source effects, limitations imposed by parameterisation, as well as the approximate nature of our method. Our approach can easily be combined with methods that take into account lateral sensitivity of surface waves. Accuracy of the method can be improved by considering a larger set of crustal types that would better capture the true variability in Earth's crustal structure, as well as topographies of intra-crustal discontinuities (such as the Conrad). We note that while increasing the number of crustal types and discontinuities would make the calculation of the correction factors more computationally costly, it would not increase computational costs associated with using the modified discontinuity topographies. The modified linear crustal corrections that we have outlined in this paper also present an advantage over numerical techniques such as the finite element or spectral element codes since they are capable, albeit approximately, accounting for the effects of near-surface, thin sedimentary layers; incorporating sedimentary basins in finite or spectral element codes vastly increases their already large computational costs. Thus, we believe

that the method presented here is particularly well-suited for taking advantage of ever-improving knowledge of crustal structure.

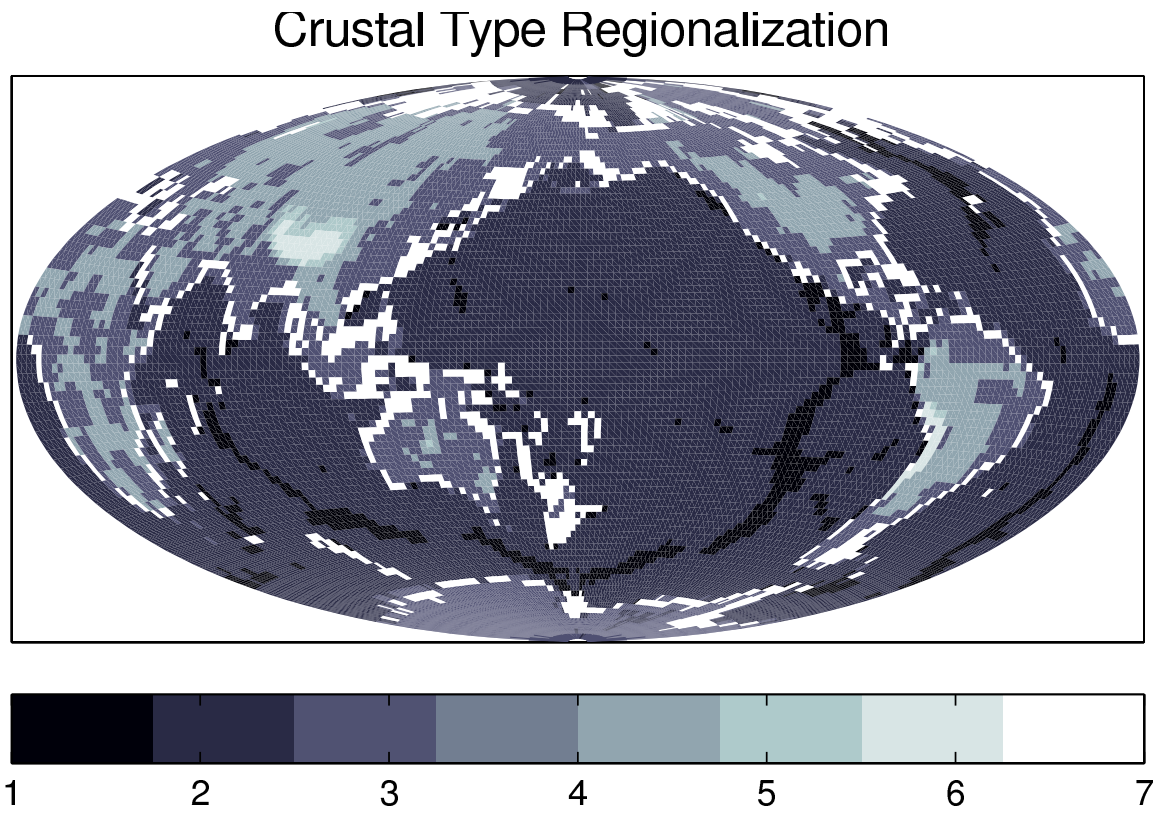

Figure 3.1: Map showing geographical distribution of the 7 crustal types used in this study.

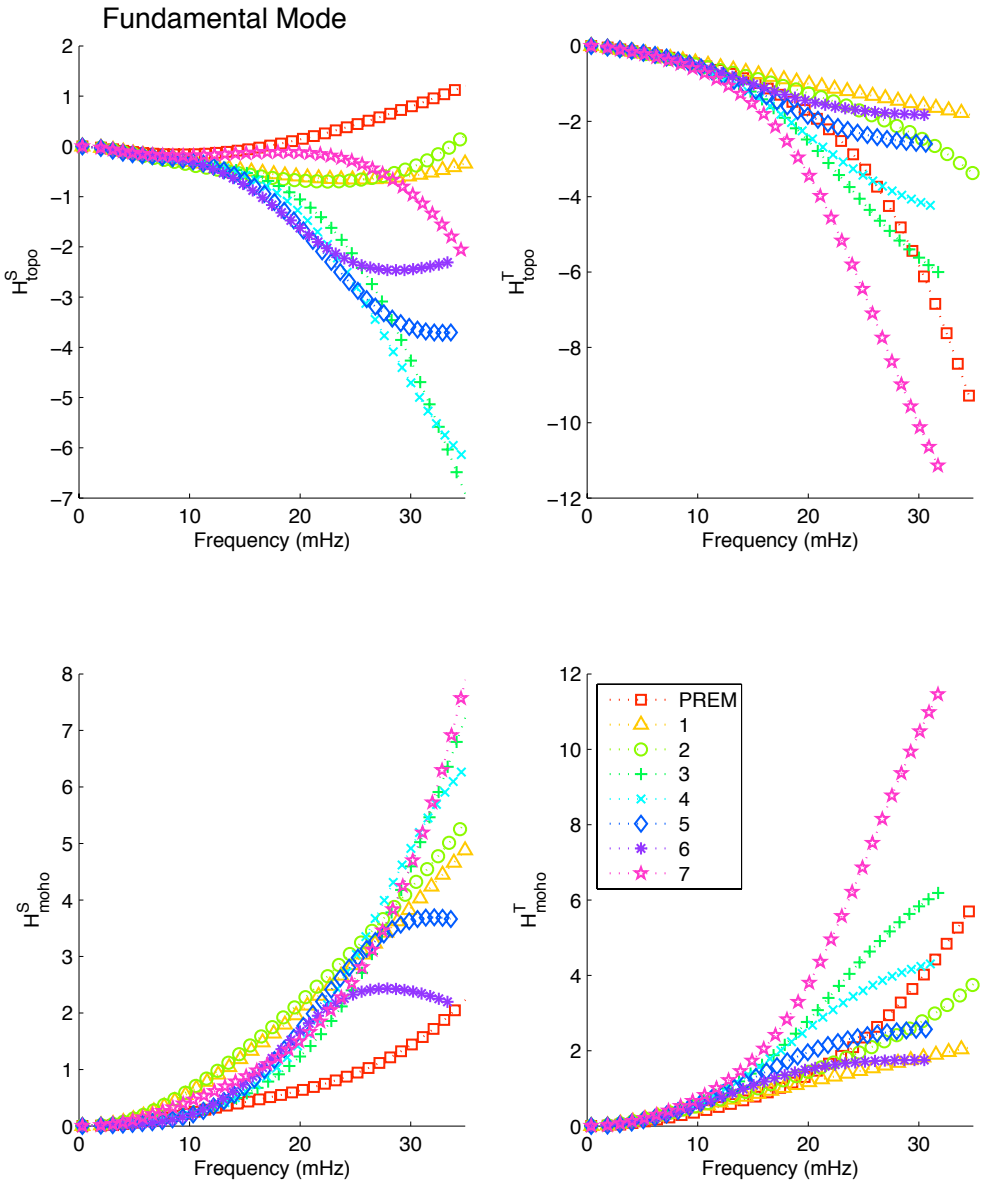

Figure 3.2: Discontinuity kernels H_k^d for surface topography (top row) and Moho depth (bottom row) as a function of frequency. Spheroidal fundamental modes are in the left column, while toroidal fundamental modes appear on the right.

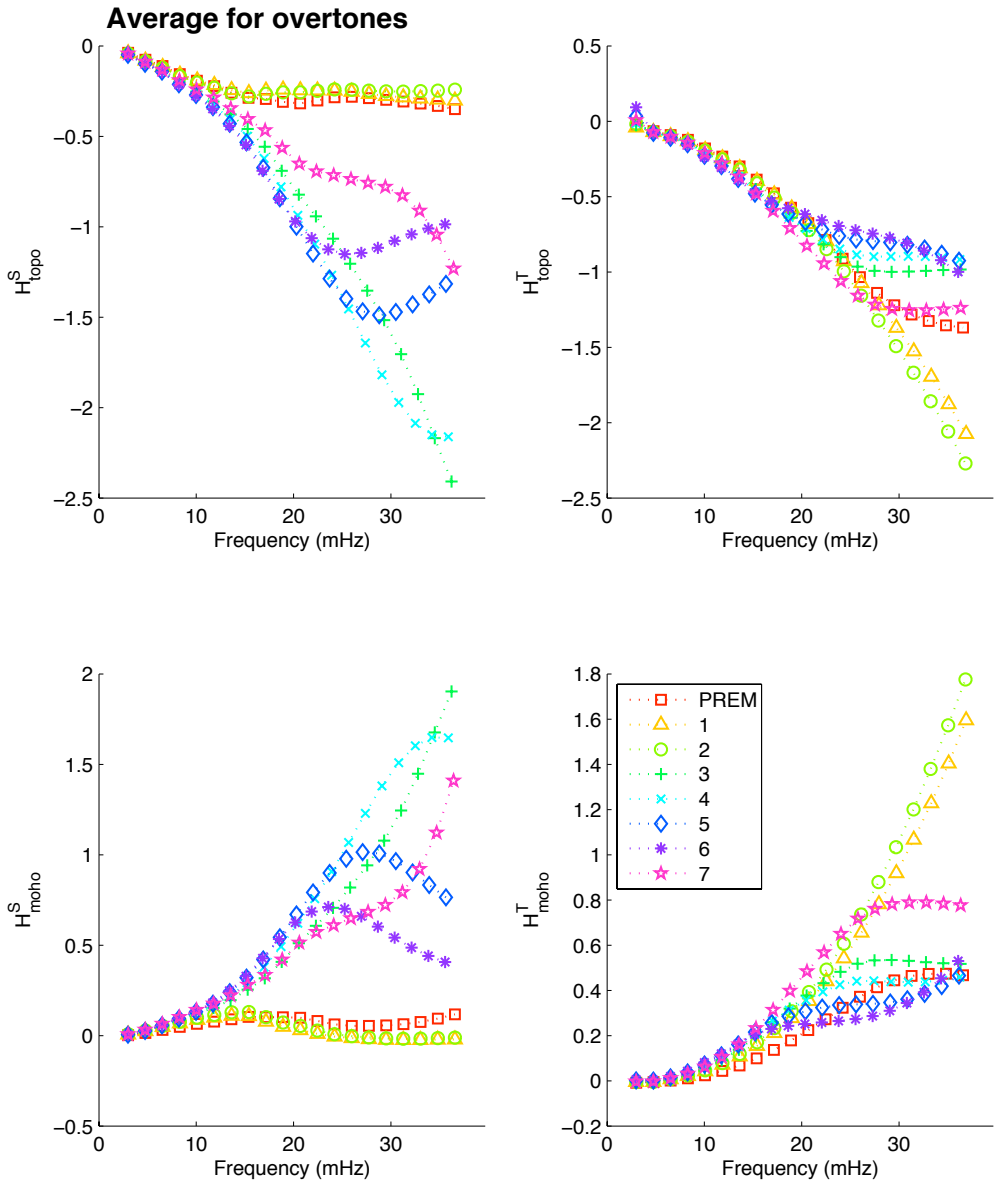

Figure 3.3: Average discontinuity kernels H_k^d of the first five overtone branches for surface topography (top row) and Moho depth (bottom row) as a function of frequency. Spheroidal modes are in the left column, while toroidal modes appear on the right.

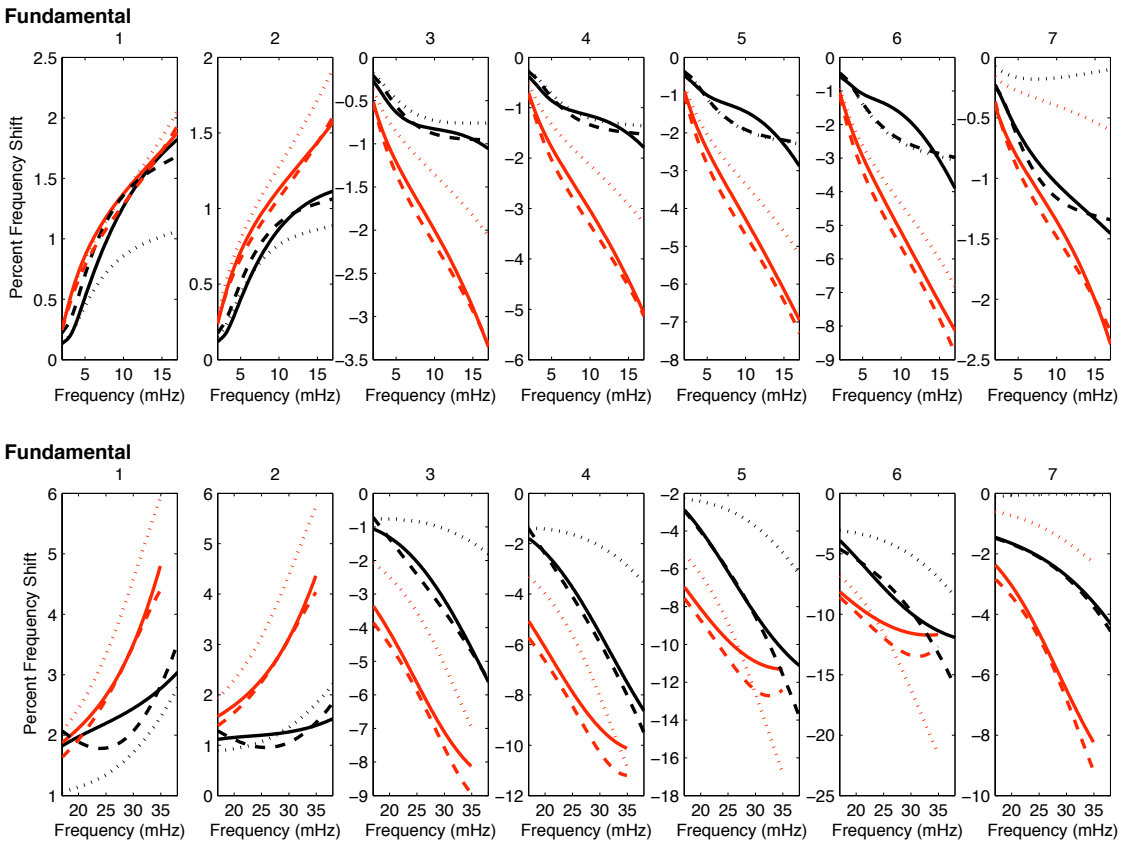

Figure 3.4: Frequency shifts of the fundamental toroidal (red) and spheroidal (black) due to differences in crustal structure between each of the canonical crustal types shown in Figures 3.1 and 3.3. Solid lines denote non-linear corrections ($\delta\omega_k^{NL}$), dotted lines indicate linear corrections($\delta\omega_k^{SL}$), and the dashed lines indicate linear corrections improved using the method outlined in this paper. Only Moho corrections are applied in the upper row, while corrections for both surface and Moho topography are required by the broader frequency range of the bottom row.

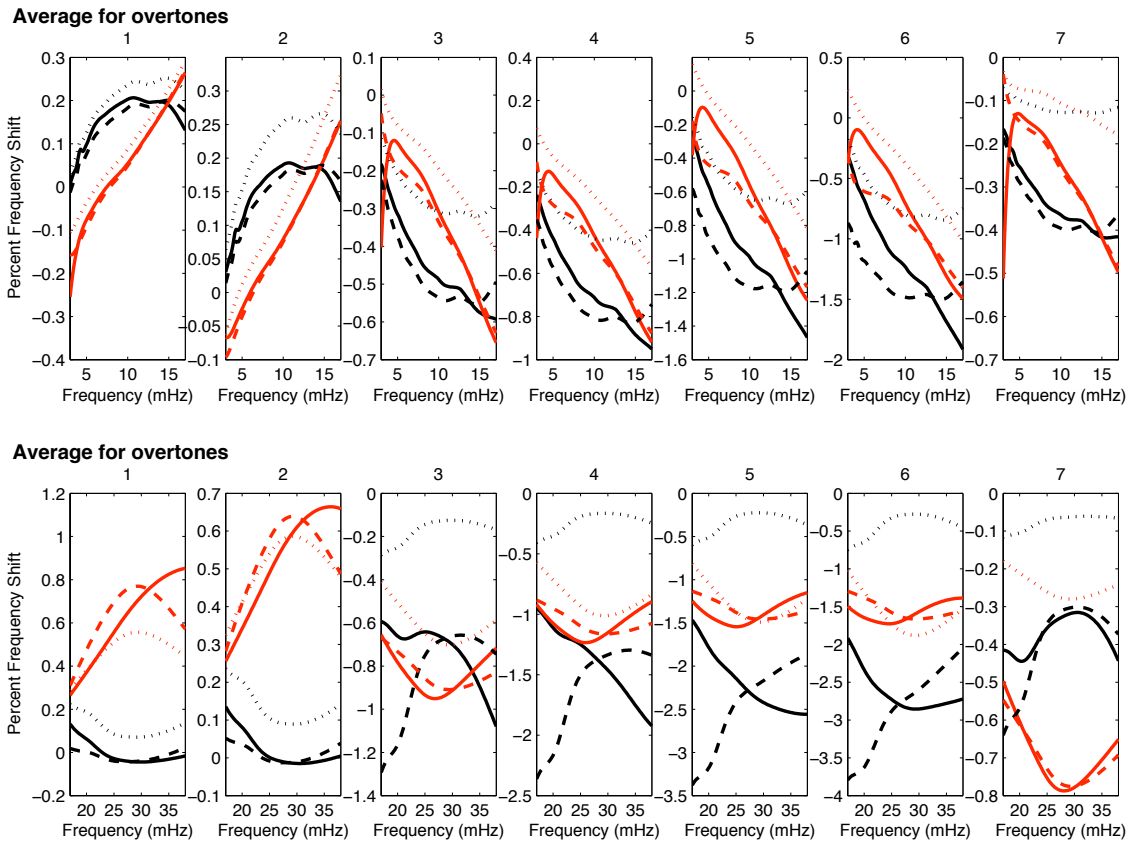

Figure 3.5: Average frequency shifts of the first five overtone toroidal (red) and spheroidal (black) branches due to differences in crustal structure between each of the canonical crustal types shown in Figures 3.1 and 3.3. Solid lines denote non-linear corrections ($\delta\omega_k^{NL}$), dotted lines indicate linear corrections($\delta\omega_k^{SL}$), and the dashed lines indicate linear corrections improved using the method outlined in this paper. Only Moho corrections are applied in the upper row, while corrections for both surface and Moho topography are required by the broader frequency range of the bottom row.

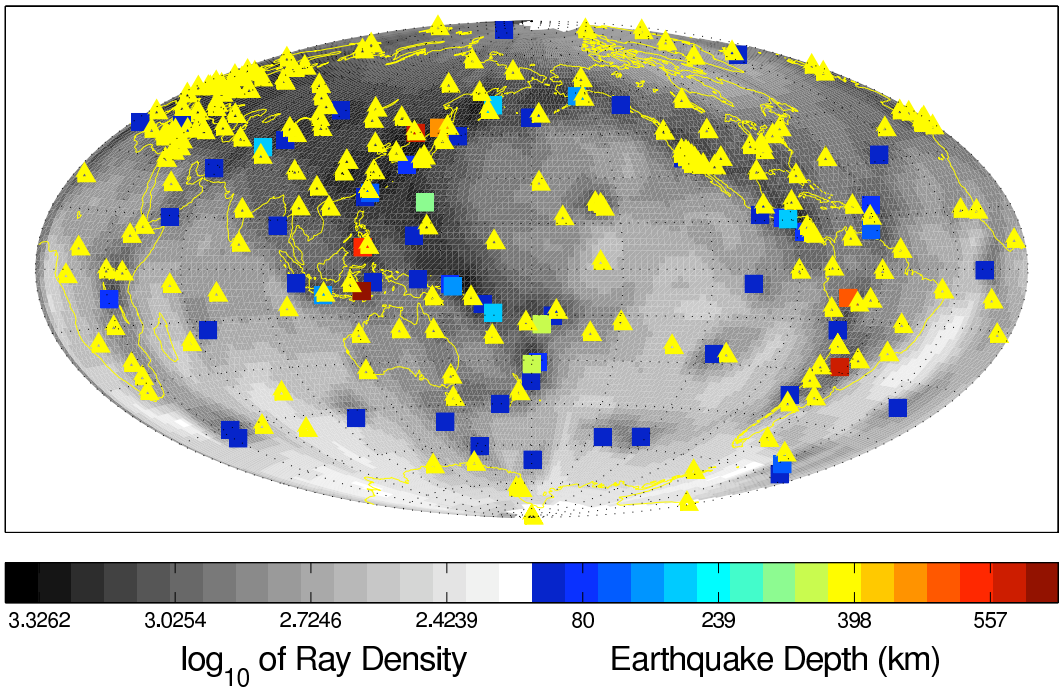

Figure 3.6: Map showing earthquake and station distribution of our synthetic dataset. Earthquakes (squares) are colour-coded by depth, while the stations are denoted by yellow triangles. The shading is proportional to the log of the number of raypaths at that location.

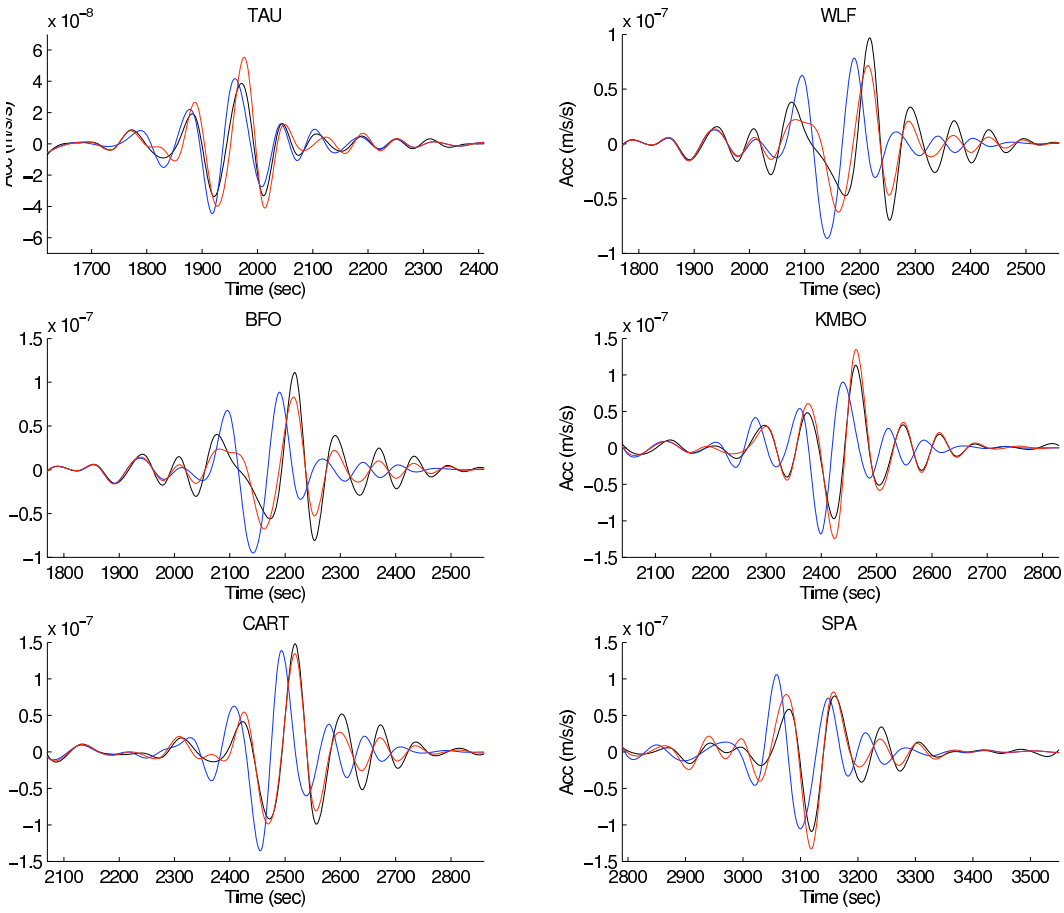

Figure 3.7: Comparison of Love waves predicted by SEM (black), standard linear corrections using NACT (blue), and our modified linear corrections using NACT (red). The earthquake is C032401C. The path to station TAU is largely oceanic, so both linear and modified corrections are capable of capturing the true crustal effect. This is not the case for continental paths, for which the use of standard linear corrections results in very large phase shifts. The modified crustal corrections do much better,

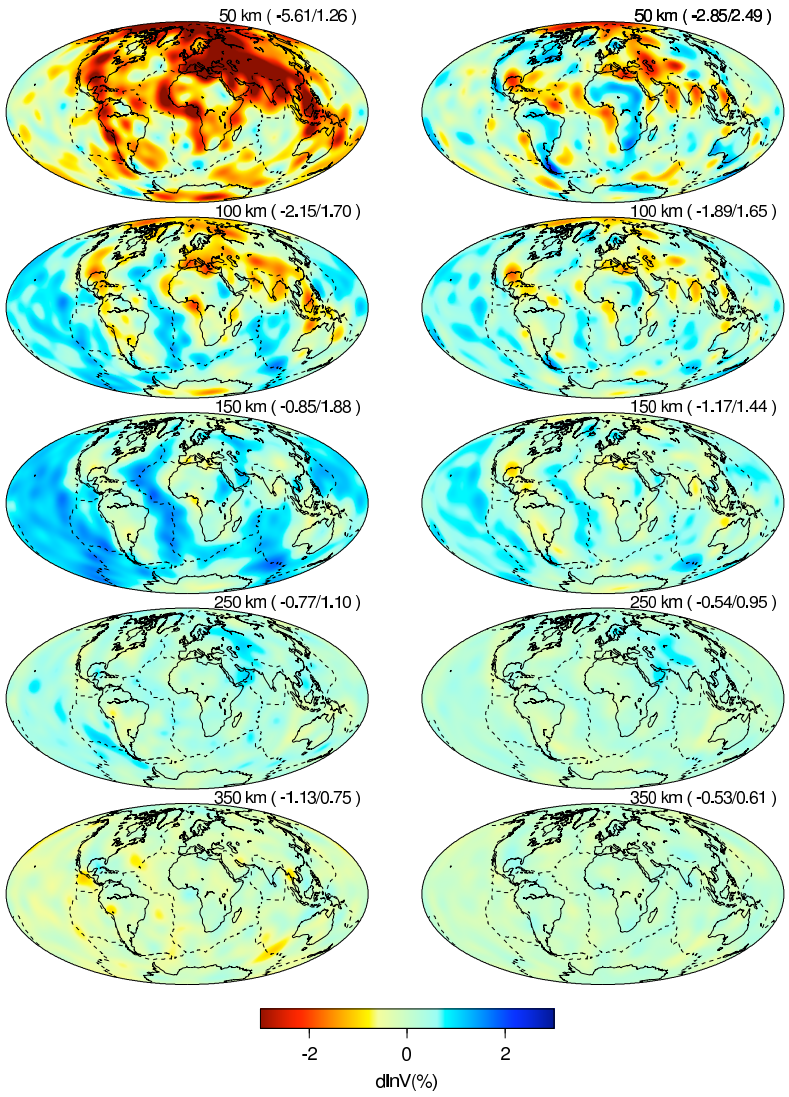

Figure 3.8: Contamination of mantle isotropic S-wave speed due to the use of standard (left column) and our modified (right column) linear crustal corrections on fundamental mode and overtone wavepackets. Warm (cool) colours indicate that using linear crustal corrections would artificially decrease (increase) retrieved mantle Vs. Note the significant amplitudes of contamination associated with standard linear corrections even at 150 km.

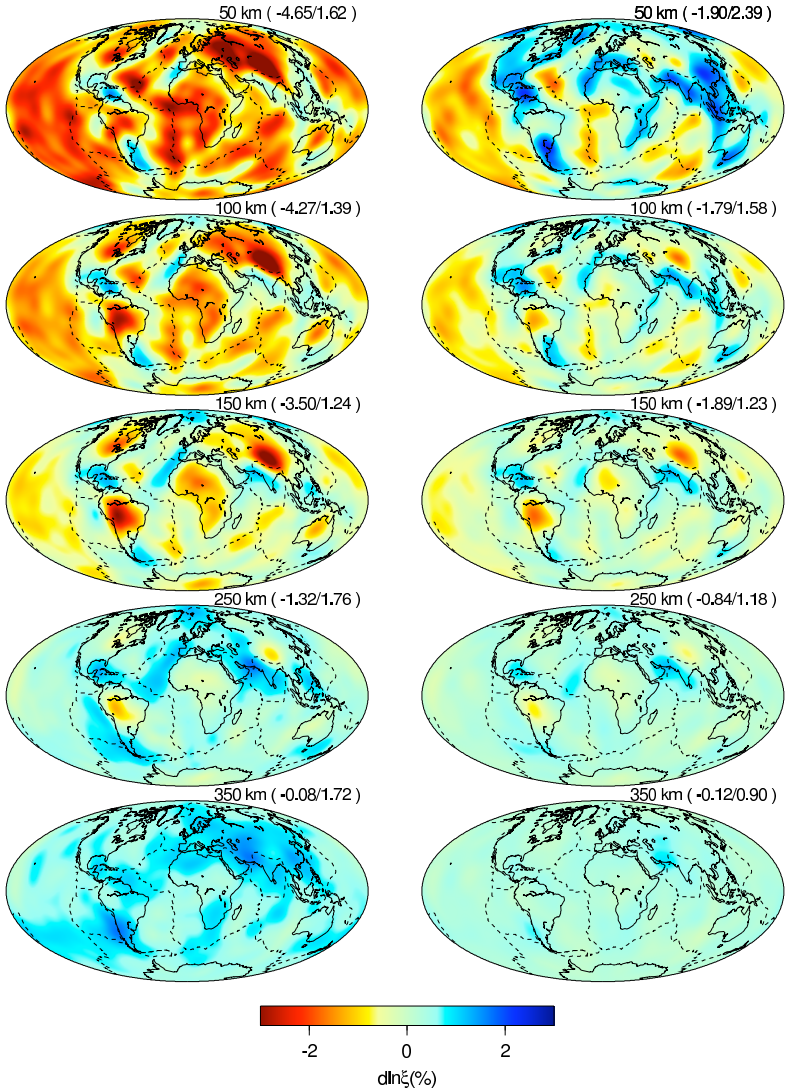

Figure 3.9: Contamination of mantle radial anisotropy due to the use of standard (left column) and our modified (right column) linear crustal corrections on fundamental mode and overtone wavepackets. Warm (cool) colours indicate that linear crustal corrections can cause artificially low (high) ξ ($V_{SV} > V_{SH}$ vs $V_{SH} > V_{SV}$). Note the large amplitudes of spurious anisotropic structure resulting from the use of standard linear corrections. Modified linear corrections result in significant reduction in contamination of anisotropic structure at all depths.

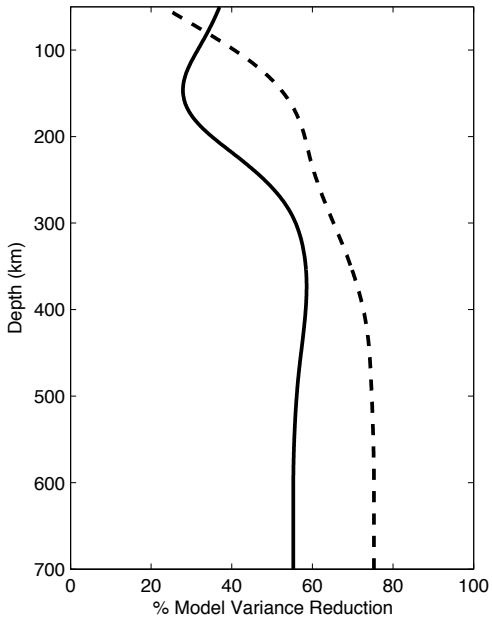

Figure 3.10: Variance reduction (in percent, relative to models obtained by standard linear corrections) provided by the use of modified linear corrections for the Vs (solid line) and ξ (dashed line) structure as a function of depth.

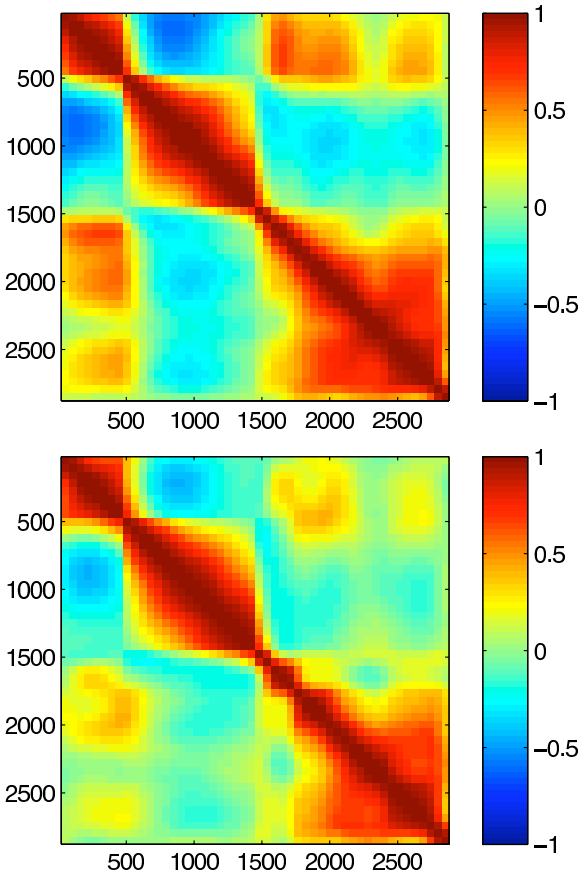

Figure 3.11: Radial correlation functions for the SAW642AN model (top) and a model derived from identical data but in which the crustal corrections were performed using modified linear corrections proposed here (bottom). Note that the use of modified linear corrections nearly eliminates the anticorrelation between upper and mid mantle structure apparent in SAW642AN. This anticorrelation is not seen in most other global models of shear wavespeed.

Chapter 4

A new method for global tomography

In this chapter, we motivate the development of a new, hybrid approach to tomography. We then describe the methods underlying this new approach. We also describe the data and creation of SEMum, a new upper mantle tomographic model of shear wave-speed and radial anisotropy. We leave discussion of the characteristics of SEMum for the next chapter.

4.1 Introduction

Since the pioneering study of Dziewonski (1977), seismic tomography has provided increasingly detailed images of the elastic structure of the Earth's deep interior. This progress was enabled by the proliferation of digital seismic data and the concomitant development

of techniques for analyzing that data based on ray- and perturbation theory. At present, several tomographic models of global structure purport to resolve structures as small as 1000 km (e.g. Panning and Romanowicz, 2006; Simmons et al., 2006; Kustowski et al., 2008; Houser et al., 2008; Ritsema et al., 2004; Shapiro and Ritzwoller, 2002). Yet, only the long wavelength variations of isotropic shear wave-speed appear to be robustly imaged on the global scale (Dziewonski, 2005) and structures smaller than $\sim$ 2500 km correlate poorly across the available models (Becker and Boschi, 2002). Discrepancies among models of variations of radial anisotropy (transverse isotropy) are present even at the longest wavelengths (see Kustowski et al., 2008; Becker et al., 2007).

The discrepancies amongst global tomographic models of mantle elastic structure can arise from a combination of factors, including data utilization, parameterization, regularization, theoretical limitations and unmodelled crustal effects.

Forward modeling of wave propagation through a complex medium such as the Earth presents a particularly difficult challenge to the robust mapping of small scale heterogeneity. This is because ray theory that underlies nearly all existing global tomographic models is expected to break down as the lengthscale of the sought-after structure approaches that of the input waveforms (see e.g. Wang and Dahlen, 1995; Spetzler et al., 2002). Even methods that include finite-frequency effects through single-scattering approximations (e.g. Dahlen et al., 2000; Zhou et al., 2006) are not accurate in modeling the effects of large anomalies (see Panning et al., 2009), which, due to the red spectrum of mantle heterogeneity (Su and

Dziewonski, 1991), are likely to dominate the observed waveforms.

Furthermore, traditional means of extracting information contained in seismic waveforms, such as phase-velocity and traveltime measurements (e.g. Ritsema et al., 2004; Houser et al., 2008) discard the constraints encoded in wave amplitudes. Yet it is precisely the amplitude information that best constrains the gradients and short-wavelength variations in elastic properties (Romanowicz, 1987). This is why Ferreira (2006) found that a number of recent nominally high-resolution models of phase-velocity anomalies did not provide better fits to observed amplitudes than a spherically symmetric model. The wealth of information contained in amplitude measurements was illustrated by Dalton and Ekström (2006), who demonstrated that phase velocity maps can be successfully extracted from amplitude information alone.

Finally, long period seismic waves used for mapping mantle structure are sensitive to both crustal and mantle structure. Thus, unmodelled effects of crustal structure can complicate and, in the case of lateral variations of radial anisotropy, even obliterate the signal coming from mantle structure (e.g. Bozdağ and Trampert, 2008). Since long-period waveforms do not have the resolution required to jointly invert for crust and mantle structure, corrections based on an assumed crustal model are typically performed. Linear corrections have been shown to be inadequate in describing the effects of the crust on surface waveforms (e.g. Montagner and Jobert, 1988). Even more accurate non-linear schemes (e.g. Marone and Romanowicz, 2007; Kustowski et al., 2007) are liable to map inaccuracies in the assumed

crustal structure, which, in the case of the most widely used CRUST2 model (Bassin and Masters, 2000), can be substantial (e.g. Meier et al., 2007; Pasyanos, 2005). Thus, eliminating the contamination of mantle images due to unmodelled crustal effects requires both the inclusion of higher-frequency data that provide better resolution of crustal structure and the use of forward modeling techniques capable of accurately predicting the effects of that structure on observed waveforms.

We develop a high resolution model of upper mantle structure, by:

1. optimizing data utilization through the use of full waveform modeling;
2. minimizing forward-modeling errors by using the spectral element method (SEM: e.g. Komatitsch and Vilotte, 1998), which is also capable of accurately representing the effects of the oceans, topography/bathymetry, ellipticity, gravity, rotation and anelasticity (Komatitsch and Tromp, 2002);
3. minimizing crustal contamination by supplementing our dataset of long period waveforms by higher frequency (T>25 s) group velocity dispersion maps.

This study develops and implements a new approach to waveform tomography, which exploits the accuracy of fully numerical wave propagation codes for forward modeling wave propagation through the Earth. Computational costs are kept reasonable by relying on approximate techniques for calculating partial derivatives that relate structure perturbations to waveform perturbations. The use of approximate partial derivatives decreases compu-

tational costs several-fold compared to adjoint methods (Tarantola, 1984) applied recently on the local (Tape et al., 2009) and regional (Fichtner et al., 2009a) scales. We stress that this study represents a break from traditional practice of tomography; for the first time, a global mantle model is constrained in large part using a fully numerical wave propagation code that dispenses with the approximations and assumptions inherent in commonly used tomographic methods.

4.2 Methods

Using seismic data to constrain the structure of the Earth's interior can be cast as a problem in which probabilities P are assigned to different possible interior structures given the available data. In this study, given a set of seismic waveforms and group velocity dispersion maps concatenated into the vector **d**, we infer the elastic parameters **m** describing the mantle, i.e. P(**m**|**d**). In practice, calculating the probabilities requires us to:

1. quantify data uncertainty;

2. incorporate *a priori* knowledge of correlations between elastic parameters in order to reduce the number of unknowns;

3. model propagation of seismic waves through heterogeneous mantle and crustal structures with minimal errors.

Waveforms of seismic waves that propagate through structure $\mathbf{m}$ are given by a non-linear function $\mathbf{g}(\mathbf{m})$. In practice, the computations and theory used to evaluate $\mathbf{g}(\mathbf{m})$ are inexact. This modeling uncertainty can be approximately summarized using a covariance matrix $\mathbf{C}_T$. We discuss the importance of this source of error in a separate section. If observational noise is close to Gaussian, we can also summarize the data uncertainty using a covariance matrix $\mathbf{C}_D$. We will summarize the *a priori* constraints on model parameters through a model covariance matrix $\mathbf{C}_M$ and a starting radially symmetric model $\mathbf{m}_0$.

Because $\mathbf{g}(\mathbf{m})$, the relation between earth structure and seismic waveforms, is non-linear, inferring Earth structure from seismic data involves an iterative procedure. At the kth iteration, then, the partial derivatives of $\mathbf{g}(\mathbf{m_k})$ with respect to model perturbations can be calculated, though they are only likely to be valid in the vicinity of the model $\mathbf{m_k}$ for which they are evaluated. Though a number of different techniques exist (see, for example Tarantola, 2005), we opt for the quasi-Newton method, as it furnishes a compromise between keeping down computational costs while ensuring a fast convergence rate. At each iteration k, the model update $\delta\mathbf{m_k}$ is obtained by solving the linear system:

$$\left[\mathbf{I}+\mathbf{C}_M\mathbf{G}_k^T(\mathbf{C}_D+\mathbf{C}_T)^{-1}\mathbf{G}_k\right]\delta\mathbf{m}_k=\mathbf{C}_M\mathbf{G}_k^T(\mathbf{C}_D+\mathbf{C}_T)^{-1}[\mathbf{g}(\mathbf{m_k})-\mathbf{d}]-\mathbf{m}_k+\mathbf{m}_0 \quad (4.1)$$

where $\mathbf{G}_k$ is the matrix of partial derivatives $(\partial d/\partial m)$ relating model perturbations to data perturbations and evaluated for the current model $\mathbf{m}_k$. This expression is obtained by re-writing expression (25) in Tarantola & Valette (1982) to avoid taking the inverse of the $\mathbf{C}_M$

matrix. The mean of the Gaussian PDF that best approximates P($\mathbf{m}|\mathbf{d}$) for iteration $k+1$ is obtained by summing the model update $\delta\mathbf{m}_k$ and the model $\mathbf{m}_k$.

4.2.1 Model parameterization and a priori information

Propagation of seismic waves through an arbitrary Hookean medium depends on 21 parameters of the stiffness tensor, and inferring the values of all these parameters at all locations within the mantle is not feasible with available seismic data. However, by approximating the Earth as a transversely isotropic medium, we can drastically reduce the number of free parameters while capturing the first order observation that horizontally polarized surface waves travel, on average, more quickly than vertically polarized ones (e.g. Anderson, 1961; McEvilly, 1964). Such a medium can be described by introducing anisotropic parameters, $\xi = V_{SH}^2/V_{SV}^2$ and $\phi = V_{PV}^2/V_{PH}^2$, in addition to the Voigt average istoropic velocities V_{Piso} and V_{Siso}, and the parameter η which governs the variation of wave-speed at directions intermediate to the horizontal and vertical. When η and ϕ are approximately equal to one, which is very likely the case in the mantle, we can approximately relate Voigt average velocities to those of vertically and horizontally polarized waves:

$$V_{Piso}^2 = \frac{1}{5}(V_{PV}^2 + 4V_{PH}^2) \tag{4.2}$$

$$V_{Siso}^2 = \frac{1}{3}(2V_{SV}^2 + V_{SH}^2) \tag{4.3}$$

as used by Panning and Romanowicz (2004). Because Love and Rayleigh waves at periods longer than 60s are primarily sensitive to shear-wave structure (see, e.g. p 344-345 of Dahlen and Tromp, 1998), we further decrease the number of parameters of interest by choosing not to invert for lateral variations in the poorly-constrained V_{Piso}, ϕ, ρ and η paremeters. Instead, we parameterize the elastic structure of the mantle in terms of V_{Siso} and ξ and impose the following a priori correlations (which are fixed):

$$\delta ln(\eta) = -2.5\delta ln(\xi) \tag{4.4}$$

$$\delta ln(V_{Piso}) = 0.5\delta ln(V_{Siso}) \tag{4.5}$$

$$\delta ln(\phi) = -1.5\delta ln(\xi) \tag{4.6}$$

$$\delta ln(\rho) = 0.3\delta ln(V_{Siso}) \tag{4.7}$$

Discussion of the reasons for this choice of physical parameterization can be found in Appendix A of Panning and Romanowicz (2006).

In depth, the model is expressed on 21 cubic splines $\nu_q(r)$ defined in Mégnin and Romanowicz (2000). The knot locations are at radii: 3480, 3600, 3775, 4000, 4275, 4550, 4850, 5150, 5375, 5575, 5750, 5900, 6050, 6100, 6150, 6200, 6250, 6300, 6346, 6361km and the surface. Laterally, we parameterize our model spatially in terms of spherical splines $\beta_p(\theta,\phi)$ (Wang and Dahlen, 1995). Thus, the value of a given model parameter m at any location in the Earth (θ,ϕ,r) can then be calculated from a set of spline coefficients m_{pq}

by:

$$m(\theta,\phi,r) = \sum_{p}\sum_{q} m_{pq}\beta_p(\theta,\phi)\nu_q(r) \tag{4.8}$$

The splines are a local basis, and thus help minimize the mapping of structure in one region into structure in distant regions, which can be an undesirable effect of global parameterizations such as spherical harmonics. By parameterizing our model, we put strict a priori constraints on the minimum lengthscale of structure allowed in our model. This truncation results in spectral leakage (aliasing) of shortscale heterogeneity into longer lengthscales (Trampert and Snieder, 1996), though the use of splines reduces this aliasing when compared to spherical harmonics or spherical pixels (Chiao and Kuo, 2001). In order to further reduce the aliasing of retrieved structure, we allow structure to vary at shorter length-scales than those that we can reasonably expect to image and interpret (Spetzler and Trampert, 2003).

Having parameterized our upper mantle model, we proceed to summarize our knowledge of upper mantle in terms of an average model ($\mathbf{m}_0$) and expected deviations from it. Our reference and starting transversely isotropic velocity model has a spherically symmetric velocity profile which is identical to PREM (Dziewonski and Anderson, 1981) below the 400 discontinuity. At depths shallower than 400 km, the model is inverted to fit long-period waveforms starting from one of the physical reference models of Cammarano et al. (2005), which are calculated from a fixed composition (dry pyrolite) and a thermal profile using the elastic and anelastic properties of principal mantle minerals.

We obtain a reference model of transverse anisotropy ξ by carrying out a grid search in which we test several hundred candidate radial distributions of ξ against observed frequencies of spheroidal and toroidal modes, keeping fixed the elastic structure. We allow smoothly-varying ξ to deviate from 1.0 (up to 1.2) at mantle depths shallower than 320 km, and do not allow values smaller than 1.0, which have been ruled out by numerous previous seismic studies (e.g. Dziewonski and Anderson, 1981). The best-fitting profile of ξ is shown in Figure5.1, alongside the profile from PREM.

The starting crustal model has average crustal velocities and thicknesses from CRUST2 (Bassin and Masters, 2000) filtered to avoid spatial aliasing by the SEM mesh. Topography from ETOPO1 (Amante and Eakins, 2008) is similarly filtered. Due to the inadequacies of CRUST2.0, we supplement our dataset by shorter period group velocity dispersion maps, and eventually invert for crustal structure. Our inversions for crustal structure require a smooth starting crustal model (unlike CRUST2.0, which is parameterized in layers), which we obtain through forward modeling described in a later section.

We stress that we could have chosen a laterally heterogeneous starting model. However, we wanted to avoid biasing our results to any of the existing global tomographic models, all of which have been developed using approximate first-order perturbation techniques. Therefore, the model we have developed is independent of previous findings.

The a priori model covariance matrix $\mathbf{C}_M$, which specifies the expected deviation of true mantle structure from that specified by our starting model, is defined by the variance σ_0^2

(which are the diagonal entries) and the horizontal and vertical correlation lengths, h_0 and v_0, associated with each spline knot. Thus, the a priori model covariance for splines i and j whose average horizontal and vertical correlation lengths are h_0 and v_0 and that are separated by Δ_{ij} horizontally and d_{ij} vertically, is given by:

$$c_M^{ij} = const \cdot exp\left(\frac{\Delta_{ij} - 1}{h_0^2}\right) exp\left(\frac{-2d_{ij}^2}{v_0^2}\right). \tag{4.9}$$

We choose vertical and horizontal lengths in line with the expected resolution of our dataset and similar to those used in previous studies, $\sim$100 km for vertical correlation length and $\sim$800 km for V_S and $\sim$1200 km for ξ.

4.2.2 Modeling long period waveforms

Calculating the non-linear function g(**m**) that relates observed long period seismic waveforms to perturbations of isotropic shear wave-speed and radial anisotropy commonly uses normal-mode summation approaches that rely on first order perturbation theory, asymptotic representations of Legendre polynomials and the stationary phase approximation (see Romanowicz et al., 2008). The most common of these approaches, the path average (great circle) approximation (PAVA: Woodhouse and Dziewonski, 1984) further simplifies the calculations by neglecting heterogeneity-induced coupling between modes on different dispersion branches.

Despite the inaccuracies of this approach (see, e.g. Li and Romanowicz, 1995; Romanowicz et al., 2008), PAVA allows computationally efficient computation of both g(**m**) and $\mathbf{G}_k$, and was used to develop the most recent radially anisotropic global mantle model (S362ANI: Kustowski et al., 2008). An improvement was proposed by Li and Tanimoto (1993), who advocated considering coupling across mode branches. Li and Romanowicz (1996) implemented a related formalism to global tomography (NACT: non-linear asymptotic coupling theory), which introduced an additional term to PAVA that accounted for coupling across normal mode dispersion branches. Panning et al. (2006) used NACT to develop a radially anisotropic model of the mantle (SAW642AN).

Fortunately, the development of computational techniques capable of fully modeling wave propagation through a complex, heterogeneous medium such as the Earth has enabled tomographers to move away from these approximate techniques. In this study, we use a version of the Spectral Element Method that couples the mesh to a normal-mode solution in the core, using a Dirichlet-to-Neumann operator (Capdeville et al., 2003) . This reduces computational costs while preserving accuracy.

Calculating g(m) and $\mathbf{C}_T$

The use of the aforedescribed approximate techniques amounts to replacing the true relationship g(**m**) of eq. 1 with an approximate one, g'(**m**). Insofar as this modeling error can be described by Gaussian uncertainties, the use of approximate forward-modeling schemes

introduces the additional covariance matrix $\mathbf{C}_T$ in eq. 1 (Tarantola, 2005). Since variances are always positive, the additional variance arising from the use of approximate forward modeling techniques will always increase the variances assigned to the observations. The use of approximate techniques can be thought of as the addition of noise to the data!

Relative contributions of observation noise to modeling noise can be compared in order to quantify the importance of using an accurate theoretical framework for modeling wave propagation. Because of its sharp lateral gradients and its non-linear effect on surface waves (Montagner and Jobert, 1988) crustal structure affects seismic waves in ways that are not readily captured by standard modeling approaches that rely on ray theory and first order perturbation theory. Bozdag and Trampert (2008) compared the most common non-linear approach for dealing with crustal structure against reference synthetics calculated using the spectral element method and found that for long paths it resulted in errors bigger than typical measurement error. Lekic et al. (*submitted*) extended this analysis to waveforms and found the often-used linear approaches to calculating crustal corrections to be inadequate. Even the effects of long-wavelength and smoothly-varying heterogeneities can be inaccurately captured by standard modeling techniques. Panning et al. (2009) find that for realistic Earth structures, the use of Born theory can result in waveform modeling errors greater than measurement error.

Making the optimistic assumption that the modelization error is Gaussian and of the same magnitude as measurement error, then the use of inaccurate forward-modeling schemes is

equivalent to doubling the uncertainty on the data. If data measurement error is also Gaussian, a dataset analyzed using accurate forward-modeling schemes carries the same uncertainty as a dataset that is four times bigger but analyzed with inaccurate forward-modeling. In fact, the more common situation is very much worse than this, since inaccuracies in forward-modeling are often correlated with Earth structure and are of different magnitude for different wavetypes. For example, inaccurately accounting for crustal structure affects Love waves more than Rayleigh waves, and can easily obliterate the anisotropic signal of the mantle (*Lekic et al., submitted*).

In this study, we minimize modelization error (rendering $\mathbf{C}_T$ negligible for our model parameterization) by using SEM to accurately calculate the propagation of waves through a complex and heterogeneous medium such as the Earth (Komatitsch and Tromp, 2002). Because our waves are insensitive to core structure and in order to reduce the computational costs, we only use the spectral element method to calculate wave propagation in the crust and mantle. In the core, wave propagation is calculated using a normal mode summation approach and it is coupled to SEM solution using a boundary-condition operator (Capdeville et al., 2003). Effects of the oceans, topography/bathymetry, ellipticity, gravity, rotation and anelasticity are all accounted for.

Calculating G_k

Due to the substantial increase in computational costs associated with the use of SEM, we rely on the approximate NACT approach to calculate the partial derivatives G_k. Even adjoint methods (e.g. Tarantola, 1984; Tromp et al., 2005) which make possible efficient SEM-based calculation of G_k, would increase computational costs several fold, compared to the use of NACT. This is because separately weighting wavepackets according to their type and thus allow fitting of overtone energies and equalizing sensitivity to horizontally and vertically polarized wavefields, would require separate calculation of adjoint kernels for each wavepacket type. Furthermore, while NACT kernels are indeed approximate, they do capture finite-frequency effects in the vertical plane defined by the great circle path, and thus enable meaningful representation of the sensitivities of body and overtone phases. While we expect that inaccuracies of NACT kernels may slow down the convergence of our iterative procedure, we are confident that our accurate evaluation of the cost function at each step will ensure that a meaningful solution is obtained. Indeed, the only requirement on the kernels is that they capture the correct sign of the partial derivatives with respect to a given model parameter once the kernels for all available data points are summed.

In the NACT formalism, a model perturbation $\boldsymbol{\delta}\mathbf{m}$ affects the seismic waveform u(t) by inducing coupling within a mode multiplet k and across multiplets k and k' within and

across dispersion branches:

$$u(t) = \Re e \left\{ \sum_k \left[(1 - it\widetilde{\omega}_{kk}) e^{i\widetilde{\omega}_{kk}t} \sum_m R_k^m S_k^m + \sum_{k' \geq k} \frac{e^{i\widetilde{\omega}_{kk}t} - e^{i\widetilde{\omega}_{k'k'}t}}{(\omega_k + \omega_{k'})(\widetilde{\omega}_{kk} - \widetilde{\omega}_{k'k'})} A_{kk'} \right] \right\} \quad (4.10)$$

where k denotes a multiplet of radial order n and angular degree l, m is the azimuthal order of singlets within the multiplet, R_k^m and S_k^m are the source and receiver vectors defined in Woodhouse and Girnius (1982), ω_k is frequency of multiplet k, and

$$\widetilde{\omega}_{kk} = \omega_k + \frac{1}{\Delta} \int_S^R \delta\omega_{kk'} \delta_{kk'} ds \quad (4.11)$$

is the new mode frequency shifted by coupling within the multiplet. Coupling across multiplets is captured by the $A_{kk'}$ term:

$$A_{kk'} = \frac{1}{2\pi} \left[Q_{kk'}^{(1)} \int_0^{2\pi} \delta\omega_{kk'}^2 cos[(l' - l)\varphi] d\varphi + Q_{kk'}^{(2)} \int_0^{2\pi} \delta\omega_{kk'}^2 sin[(l' - l)\varphi] d\varphi \right] \quad (4.12)$$

where the integrations are carried out of the great circle containing source and receiver and the expressions for $Q_{kk'}^{(1,2)}$ can be found in appendix A of Li and Romanowicz (1995). Finally, the mode frequency shifts due to heterogeneity-induced coupling are given by:

$$\delta\omega_{kk'}(\theta, \phi) = \frac{1}{\omega_k + \omega_{k'}} \int_0^{R_\oplus} \delta\mathbf{m}(r, \theta, \phi) \mathbf{M}_{kk'}(r) r^2 dr \quad (4.13)$$

where the kernels, $\mathbf{M}_{kk'}$ can be calculated according to expressions derived by Woodhouse

and Dahlen (1978) in the case when $k = k'$ and Romanowicz (1987) when $k \neq k'$.

From these expressions, we derive the partial derivatives that make up $\mathbf{G}_k$ (for an explanation of how this is done, see Li and Romanowicz, 1995). Effects of lateral heterogeneity $\delta\mathbf{m}$ on the seismic waveforms $u(t)$ are fully captured by considering the coupling-induced frequency shifts $\omega_{kk'}$ of normal modes. Symbolically, $\partial u(t)/\partial\delta\mathbf{m} = F(\delta\omega_{kk'})$. In fact, NACT waveform kernels can be thought of as weighted averages of individual mode frequency kernels $\mathbf{M}_{kk'}$, in which the weights depend on the seismic source characteristics, observation component, source-receiver distance and time. For the case of the fundamental mode dispersion branch ($n = 0$) which comprises Rayleigh and Love waves, it is sufficient to consider only along-branch coupling, and neglect modes for which $n \neq n'$.

4.2.3 Modeling group velocity dispersion

Consider a wave whose speed of propagation depends on three interdependent variables: its frequency (ω), the elastic properties of the medium (m), and its wavenumber (κ). The cyclic chain rule relates the partial derivatives of ω, m and κ:

$$\left(\frac{\partial\omega}{\partial\kappa}\right)_m \left(\frac{\partial\kappa}{\partial m}\right)_\omega = -\left(\frac{\partial\omega}{\partial m}\right)_\kappa \tag{4.14}$$

Introducing the group velocity $U = \left(\frac{\partial\omega}{\partial\kappa}\right)_m$, and the wave-speed $c = \omega\kappa$, we can rearrange

this expression to obtain:

$$\frac{U}{c^2}\left(\frac{\partial c}{\partial m}\right)_{\omega} = \frac{1}{\omega}\left(\frac{\partial \omega}{\partial m}\right)_{k} \tag{4.15}$$

which expression can be used to calculate phase velocity kernels at a fixed period from eigenfrequency kernels calculated at fixed wavenumber. It is important that these partials are exactly the required ones, since we are keeping frequency constant, and phase (and group) velocity measurements are made at a specific frequency, rather than a particular wavenumber. If only coupling within a mode multiplet is considered, our waveform analysis is built upon kernels $\mathbf{M}_{kk}$ which capture the effect of a relative model perturbation $\delta\mathbf{m}/\mathbf{m}$ on the squared frequency ω^2, i.e. $\mathbf{M}_{kk} = 2\omega m\left(\frac{\partial\omega}{\partial\mathbf{m}}\right)_{\kappa}$. Then, the logarithmic phase velocity kernel, $K^c = \frac{m}{c}\left(\frac{\partial c}{\partial m}\right)_{\omega}$ can be written as:

$$K^c = \frac{c}{2U\omega^2}\mathbf{M}_{kk} \tag{4.16}$$

In order to obtain the expressions for group velocity kernels, we start by expressing U in terms of c and $(\partial c/\partial\omega)_m$, and differentiate the expression with respect to $\mathbf{m}$. Reorganizing, we obtain expressions for the group velocity kernels:

$$\left(\frac{\partial U}{\partial m}\right)_{\omega} = \frac{U^2}{c^2}\left[\left(\frac{2c}{U}-1\right)\left(\frac{\partial c}{\partial m}\right)_{\omega} + \omega\left(\frac{\partial}{\partial\omega}\right)_{m}\left(\frac{\partial c}{\partial m}\right)_{\omega}\right] \tag{4.17}$$

The second term of this expression involves taking the frequency derivative of the phase

velocity kernels. This can be done numerically (Rodi et al., 1975) by differencing the phase kernels calculated at $\omega + \delta\omega$ and $\omega - \delta\omega$. In practice, we are concerned with group velocity dispersion measurements made on the fundamental mode branch, so in order to obtain group velocity kernel corresponding to the frequency of a mode with angular order $l = l_0$, we difference phase velocity kernels for $l = l_0 - 1$ and $l = l_0 + 1$, and divide by the difference in the eigenfrequencies $\Delta\omega = \omega_{l+1} - \omega_{l-1}$.

Casting equation 4.17 in terms of K_c, defines a new group velocity kernel K_U which relates logarithmic perturbations in model parameters to logarithmic perturbations in group velocity:

$$K^U = \frac{m}{U}\left(\frac{\partial U}{\partial m}\right)_\omega = K^c + \omega\frac{U}{c}\left(\frac{\partial}{\partial \omega}\right)_m K^c \tag{4.18}$$

Ensuring linearity

These kernels relate group velocity U at some point on the surface of the Earth (θ, ϕ) measured at frequency ω_j to the elastic structure beneath that point. Let the vector m_{pq} represent a set of coefficients that capture earth structure parameters expressed in terms of spherical splines $\beta_p(\theta, \phi)$ and vertical cubic splines $\nu_q(r)$. The structure at point (r, θ, ϕ) is then given by equation 4.8.

In genereal, the relationship between model vector m_{pq} and group velocity at a specified

location $U_j(r,\theta,\phi)$ (where j is indexes the frequency ω_j at which the group velocity is measured) is described by a non-linear function $\mathbf{g}(\mathbf{m})$. However, in the vicinity of a reference model ${}^{i}m_{pq}$, small changes in structure δm will not appreciably change the kernels ${}^{i}K_j^U(r)$; in this situation, deviations of group velocity from the reference value ${}^{i}U_j$ will be linearly related to the perturbations of the model parameters from ${}^{i}m_{pq}$:

$$\sum_p \sum_q \frac{m_{pq} - {}^{i}m_{pq}}{{}^{i}m_{pq}} \beta_p(\theta,\phi) \int_0^a {}^{i}K_j^U(r')\nu_q(r')dr' = \frac{U_j(r,\theta,\phi) - {}^{i}U_j}{{}^{i}U_j} \tag{4.19}$$

where a is the radius of the earth. By introducing ${}^{i}M_{j,q}^U$ as the radial integral of kernel ${}^{i}K_{j,q}^U(r)$ with vertical spline $\nu_q(r)$, we can re-write the expression as:

$$\sum_p \beta_p(\theta,\phi) \sum_q^i M_{j,q}^U dln\, m_{pq} = dln {}^{i}U_j \tag{4.20}$$

or in matrix notation:

$$(\mathbf{M} \otimes \mathbf{B})\ \delta ln\mathbf{m} = \mathbf{G}\ \delta ln\mathbf{m} = \delta ln\mathbf{U} \tag{4.21}$$

where $\mathbf{B}$ is the matrix of spherical spline values at points of interest, and $\otimes$ denotes the Kronecker product. The matrix $\mathbf{G}^T\mathbf{G}$ will have the same dimension as that for the waveform inversion, and the set of linear equations that represent the constraints provided by group velocity maps can then be weighted and added to the set of equations furnished by the waveform dataset.

In order to ensure that we use these kernels only in the valid, linear regime in which model perturbations are linearly related to group velocity perturbations, we need to generate a set of reference models ${}^{i}m_{pq}$ which span a sufficiently broad range of profiles of crustal and mantle velocity structure to capture the heterogeneity present in the Earth. We accomplish this by taking a set of five profiles that span the variability present in a pre-existing model of upper-mantle and crustal shear wave-speed structure.To avoid biasing our modeling toward pre-existing models of crustal structure such as CRUST2.0, we conduct a grid search to develop a new starting model of crustal structure.

We do this by generating 21,000 models of crustal structure in which we vary the model coefficients m_{pq} so that crustal V_S takes on values between 3-4.5 km/s in the oceans and 2-4 km/s in the continents. After a series of tests, we choose to keep apparent Moho depth fixed at 60 km and introduce crustal ξ to compensate, allowing it to vary from 0.8-1.4. This is because the introduction of anisotropy allows a smooth model to have a similar response for long period waves as a model with thin layers (see Backus, 1962; Capdeville and Marigo, 2007). Having a deeper Moho avoids the need for meshing thin shallow layers, thereby reducing computational costs associated with the spectral element method three-fold. The group velocities for each of the candidate models are calculated by integrating the elasto-gravitational equations (Woodhouse, 1998), and the model best predicting the observed Love and Rayleigh group velocity dispersion is selected at each point. Our crustal model, then, specifies a smoothed crustal structure beneath each point on the Earth that fits the group velocity dispersion data. Even though the best-fitting model is selected considering

only fundamental mode dispersion, we confirm that it also provides fits for overtones. This procedure is similar to the one used by Fichtner and Igel (2008). We then use this smooth crustal model alongside a long wavelength model of crustal structure to extract five reference models ${}^{i}m_{pq}$, within the vicinity of which the variations of group velocity lie in the linear regime.

4.3 Data and noise

In this study, long period seismic waveforms and group velocity dispersion maps are used together in order to constrain the variations of crustal and upper mantle shear wave-speed and radial anisotropy. In order to better map shallow structure, we must consider higher frequency waveforms, the modeling of which presents excessive computational costs. Therefore, we choose to supplement our waveform dataset and improve constraints on shallow structure using group velocity dispersion maps provided by Ritzwoller (*personal communication*). Shapiro and Ritzwoller (2002) explain the data and uncertainties associated with these dispersion maps. Group velocity dispersion measurements have the advantage of not being susceptible to cycle-skipping errors that beset phase measurements at high frequencies. In addition, at the same period, the group velocity is sensitive to more shallow structure than is phase velocity.

Our waveform dataset comprises fundamental mode Love and Rayleigh waves, which pro-

vide excellent coverage of the uppermost 300 km, long period overtones crucial to imaging the transition zone, and long period body waves which improve transition zone constraints while introducing some sensitivity to the lower mantle. Sensitivity tests show that lower mantle structure at most contributes a few percent to the misfit of the wavepackets that include body waves; nevertheless, we correct for lower mantle strucutre by using SAW24B16 model of Megnin and Romanowicz, 2000. Full waveform modeling of higher frequency waves can be computationally costly and prone to errors due to cycle-skipping or mismapping of multiply-reflected energy.

We use 3 component long-period accelerograms bandpass filtered using a cosine-taper window with cutoffs at 60 and 400s and corners at 80 and 250s . In order to ensure high signal to noise level and limit the effects of possible complexity of the seismic moment-rate function, our dataset is restricted to 104 earthquakes with moment magnitudes $6.0 \leq M_w \leq 6.9$. These are shown in Figure 4.1. Moment tensors and source location are taken from the Harvard Centroid Moment Tensor project (*www.globalcmt.org*). The waveforms are recorded at broadband stations of the global seismic network (GSN), GEOSCOPE, GEOFON, and several regional networks.

Each waveform is divided into wavepackets that isolate, in the time domain, the large amplitude fundamental-mode surface waves from smaller higher-mode waves. This allows separate weighting coefficients to be applied to the wavepackets, so that the large-amplitude signals are prevented from dominating the inversion. A detailed description of the scheme

used for constructing wavepackets can be found in Li and Romanowicz (1996), henceforth LR96. Our analysis includes both minor- and major-arc Love and Rayleigh waves and overtones since the major-arc phases provide complementary coverage to that afforded by the minor-arc phases. By including major-arc phases, we ensure much better coverage of the southern hemisphere in which many fewer broadband stations are located compared to the northern hemisphere. Figure 4.1 shows the density of ray coverage for the complete waveform dataset. The inclusion of overtones is crucial for resolving structure deeper than about 300 km, including the transition zone (*e.g. Ritsema et al.*, 2003).

An automated, but user-reviewed, picking scheme is used in order to select only well-recorded accelerograms (see Appendix B of Panning and Romanowicz, 2006). This is done to avoid noisy data and to identify other problems including reversals of polarity, timing errors, gaps, spikes and incorrect instrument response information. The data are then hand-reviewed and the data covariance matrix $\mathbf{C}_D$ is calculated. We assess the signal-to-noise level of our dataset by taking the quietest 5 minute interval within the time-period as a representative sample of underlying noise. The standard deviation of the signal is then divided by the standard deviation of the noise in order to obtain a signal-to-noise summary statistic for each wavepacket. The low-noise characteristics of the data summarized in Fig. 4.3 justifies our picking procedure. We use the scheme proposed by LR96 to approximate the data covariance matrix $\mathbf{C}_D$ by a diagonal matrix whose entries w_i are the product of three measures of data undesirability: 1. the signal root-mean-square level; 2. data content of each wavepacket; and 3. path uniqueness. The final term is beneficial since it homogenizes

the data coverage across the globe.

Because surface waves are sensitive to variations in both azimuthal and radial anisotropy (e.g. Montagner and Jobert, 1988), accurate retrieval of variations in radial anisotropy requires that the data provide broad sampling of azimuths, so that the azimuthal dependence can be averaged out and not contaminate the model of velocity or radial anisotropy. We verify that our dataset provides sufficient azimuthal coverage by binning rays passing through 10^o by 10^o bins by azimuth for each component of our dataset and plot them in Figure 4.2 on a rose diagram.

4.4 Inversion and fits

We initialize our iterative inverse scheme with our starting 1D model, CRUST2 crustal velocities and Mohorovicic topography, and invert for large-scale structure of the mantle V_{Siso}, which we accordingly parameterize with only 162 horizontal splines. At each iteration, we calculate data misfits using SEM synthetic waveforms. We also re-calculate the kernels for the partial derivatives matrix G in the updated 1D model, and approximately account for the effects of 3D structure on the partial derivatives by re-calculating the frequency shifts $\omega_{kk'}$ of equation 4.13. Crustal effects are also accounted for in the partial derivatives matrix through the frequency shifts $\omega_{kk'}$, though these are calculated using the modified linear corrections approach developed by Lekic et al. (*submitted to GJI*).

In the NACT formalism, the effect of 3D structure on both g(m) and the partial derivatives matrix G is non-linear, because the frequency shifts appear in the exponent (see Equation 4.10). This allows us to introduce "minor" iterations between SEM runs, with the goal of speeding up the convergence of the iterative scheme. Thus, in the early iterations, which tend to produce large model updates δm, we introduce a few "minor" iterations in which the waveform perturbation δu due only to the model update δm_k (not m_k the deviation of the current model from the 1D profile) is added to the SEM synthetics for that iteration, and the residual $[\mathbf{g}(m_k+\delta m_k)-d]$ is approximated by $[\mathbf{g}(m_k)+\mathbf{g}'(\delta m_k)-d]$, where the NACT synthetic is primed. These approximate residuals are then inverted with an updated partial derivatives matrix for another perturbation $\delta m'_k$. Thus, the effective model perturbation δm for k-*th* "major" iteration is the sum of the model updates: $\delta m = \delta m_k + \delta m'_k$. SEM synthetics are then used to calculate the exact residual for a model that incorporates this total model update, i.e. $[\mathbf{g}(m_k+\delta m)-d]$.

In order to minimize computational costs, we begin the iterative scheme with a well-distributed subset (67) of the earthquakes in our dataset. Once we retrieve the long-wavelength features of lateral heterogeneity, we refine our V_{Siso} horizontal parameterization to 642 horizontal splines, and expand the subset of earthquakes to 80. Starting with the third iteration, we use the entire dataset (104 earthquakes) and allow long-wavelength variations of radial anisotropy, parameterizing variations of ξ with 162 horizontal splines. We settle on a final parameterization with 2562 splines for V_{Siso} and 642 for ξ. This corresponds to spherical harmonic expansions to degree ~ 48 and 24, respectively.

Our effective dataset expands with each subsequent iteration, as our model better captures the true structure of the Earth and fits to waveforms improve. This is because we only use data that are sufficiently similar to the synthetic seismograms at each iteration, in order to avoid cycle-skipping problems to which waveform modeling in the time domain is susceptible. We stress that fits improve systematically even for waveforms not included in the inversion! The fact that the number of acceptable waveforms increases with refinements to our model independently confirms the validity of our inversion scheme, our forward modeling approach, and the use of approximate sensitivity kernels G.

After four iterations, we discovered that we could not simultaneously fit Rayleigh and Love waves. This, combined with inaccuracies of CRUST2 at both the global (*Meier et al.*, 2007; *Masters, personal communication*) and regional (e.g. *Pasyanos and Nyblade*, 2008) scales, motivated us to invert for crustal V_{Siso} and ξ structure by adding constraints from Love and Rayleigh group velocity dispersion maps in our inversions. At each iteration, the tomographic model is regionalized into five representative profiles or radial structure (${}^{i}m_{pq}$), and group velocity kernels are calculated for each of these; the kernel for the radial profile most similar to that beneath a given point is then used in the construction of the partial derivatives matrix G. We carried out four more iterations before our inversion appeared to converge, and misfits only marginally improved for two consecutive iterations.

The final model, which we hereafter refer to as SEMum, provides $\sim$75% variance reduction with respect to the starting model to the fundamental mode waveforms recorded on

the longitudinal and vertical components, and 53% improvement on the somewhat noisier transverse component. For overtones, the final variance reduction was $\sim$40% on all components, probably due to the higher levels of noise contribution in these wavepackets. Mixed, fundamental-overtone wavepackets had variance reductions of $\sim$70% on the vertical and longitudinal component, and $>$80% on the transverse component. Figures 4.4 and 4.5 show waveform fits before and after inversion for a typical event. Variance reduction for the group velocity dataset is $\sim$ 60%.

Since our waveform misfit function is affected by both amplitude and phase differences between data and synthetics, we separately analyze the contribution of phase alignment and amplitude similarity to the variance reduction for different wavepacket types and components. The results of this analysis are summarized by histograms in Figure 4.6 for the vertical component, and in Figure 4.7 for the transverse component. The root-mean-squared waveform misfits between data and synthetics in both the starting model (gray) and SEMum (purple) are shown in the left column of both figures. These are calculated by taking the square root of the variance of the residual seismogram between the synthetics and data, normalized by the variance of the data. We can see that for both components and all wavepacket types, misfit is reduced, though the reduction is more apparent for the minor-arc phases than the more-noisy major-arc ones, and for surface waves than overtones.

The middle column of each figure shows histograms of the correlation coefficient between the synthetic and data waveforms. Correlation coefficients are only sensitive to phase align-

ment and are independent of amplitude misfits. Comparing the histograms for the starting model and SEMum synthetics, we see dramatic improvement in phase alignment for all wavepacket types, though, once again, we see poorer alignment for overtones and major-arc phases. In order to probe the improvement in amplitude fit, we calculate the envelopes of both data and synthetics and calculate the ratio of the ten largest data values divided by the ten largest values for the synthetics. The third column of both figures shows histograms of the natural logarithm of this ratio; a value of zero is perfect amplitude agreement, negative values indicate that synthetic waveforms are too large and positive values indicate that the synthetic waveforms are too small. While SEMum synthetics clearly have more similar amplitudes to the observations than do synthetics in the starting model, the improvement is not dramatic. Thus, the vast majority of the waveform improvement provided by SEMum results from phase alignment rather than amplitude fits.

4.5 Resolution Tests

In order to ascertain the reliability of our model, we undertake a series tests using the resolution matrix. Analyses that rely upon the resolution matrix help quantify the resolving power of a model given the data distribution, sensitivity and noise, as well as the amount and character of *a priori* information used. However, resolution matrices are strictly only valid for linear problems, though they remain approximately valid for mildly non-linear

problems (e.g. Tarantola, 2005). Furthermore, they do not in any way account for inaccuracies due to theoretical and computational approximations. Because our hybrid method of tomography takes advantage of accurate SEM synthetics and thereby substantially reduces theoretical and computational errors, analysis of the resolving power of our dataset based on the resolution matrix is more appropriate in our case than for other tomographic inversions to which it is commonly applied.

By applying the resolution matrix operator on a set of synthetic input models, we obtain output models which capture the ability of our dataset to image the input structure. Before proceeding to explore the geographic resolving power of our dataset, we conduct a set of tests that explores the expected amount of cross-contamination between elastic and anelastic structure in SEMum. The left panel of Figure 4.8 shows the retrieved V_S anomalies for an input model that contains only ξ structure, which is identical to the ξ structure of SEMum. We can see that variations of isotropic shear wave-speed are not likely to be contaminated by anisotropy. The right panel of Figure 4.8 shows the retrieved ξ anomalies for an input model that contains only V_S structure, which is identical to the V_S structure of SEMum. Once again, the contamination is negligible (smaller than 0.5% at all depths); we conclude that our retrieved ξ structure is unlikely to be contaminated by variations of isotropic shear wave-speed, insofar as those are captured by SEMum.

We explore the resolving power of our dataset at different depths by considering a set of input checkerboard patterns of various lengthscales. Figure 4.9 shows checkerboard tests

in which the input model contains only V_S variations; we show both V_S and ξ variations of the output model. At 300 km depth, we are able to robustly resolve both the amplitude and pattern of isotropic shear wave-speed variations with lengthscales of $\sim$1500 km. Patterns with larger scale features are also robustly retrieved, and the smallest resolved lengthscale is even shorter at shallower depths. At a depth of 600 km, however, our resolution degrades, and we can only robustly retrieve V_S variations that are 2500 km across or bigger. Furthermore, whereas contamination of ξ structure was undetectable at 300 km depth, it is small but present in the transition zone.

Checkerboard resolution tests shown in Figure 4.10 demonstrate that our resolving power for variations of ξ is weaker than for V_S. At 300 km depth, the minimum lengthscale of robustly imaged ξ structure is somewhat smaller than $\sim$2500 km. However, in the transition zone, we are only able to resolve anomalies 4000 km across. While no significant contamination of V_S structure by variations in ξ are seen at either depth for the chosen checkerboard lengthscales, we note that smaller scale variations in ξ map strongly into V_S variations at 600 km depth. These tests show that our dataset of overtone wavepackets needs to be expanded in order to provide resolution of anisotropic structures shorter than 4000 km in the transition zone.

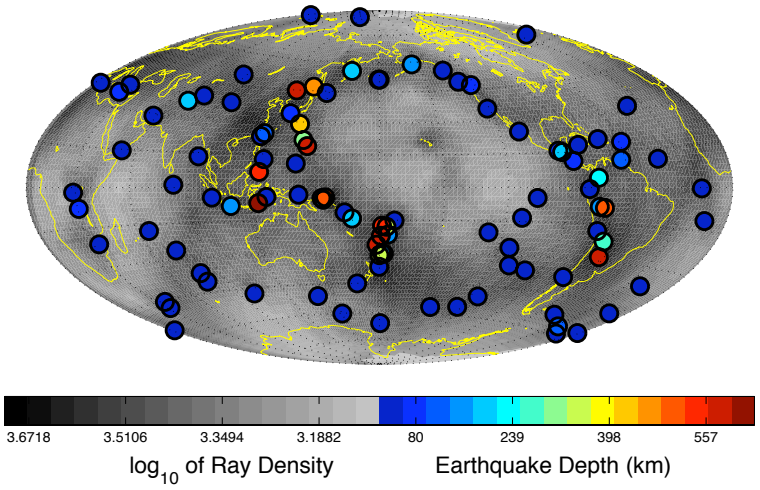

Figure 4.1: Map showing the earthquakes used in our study, which are colorcoded according to centroid depth. The shading indicates the ray coverage number density on a log scale.

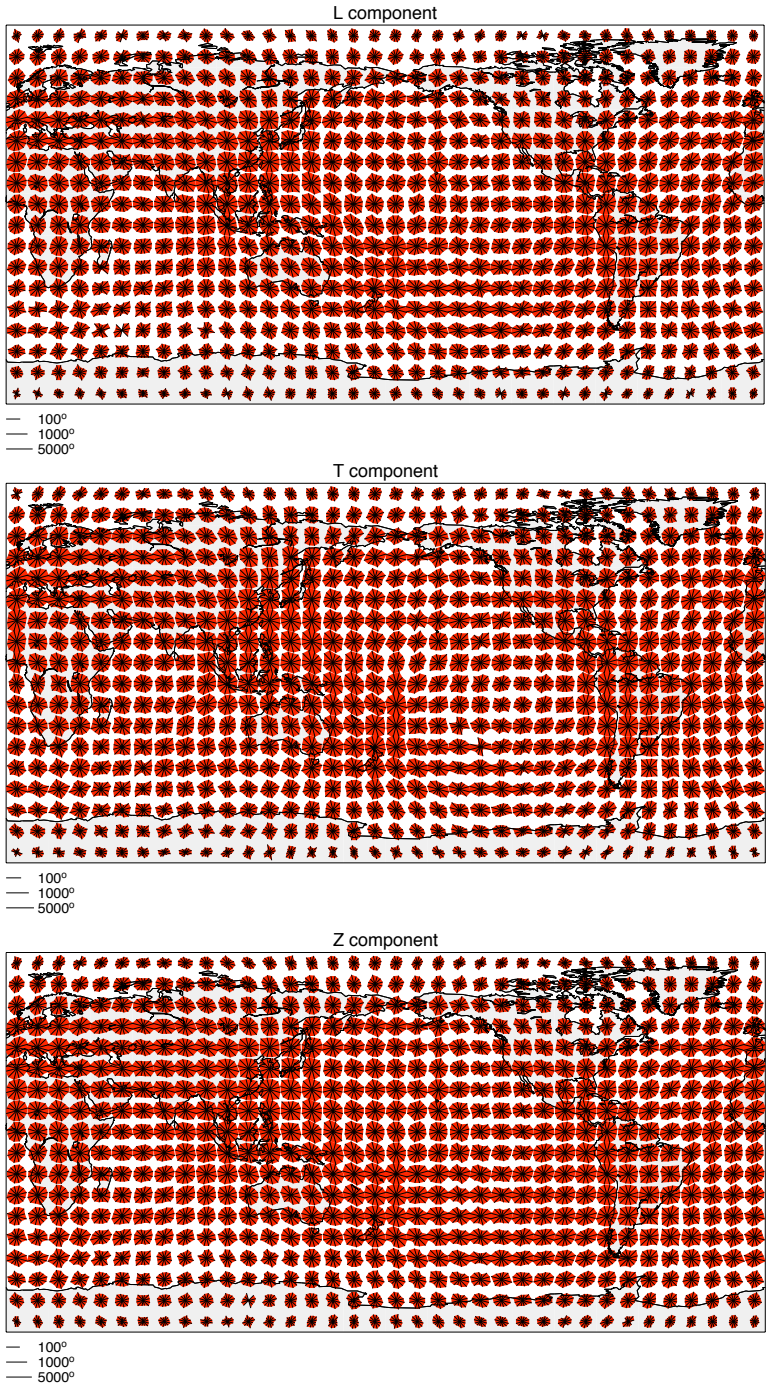

Figure 4.2: Rose diagrams showing the azimuthal distribution of raypaths passing through each 10^o by 10^o block. Note that the azimuthal coverage is good for the longitudinal (top), transverse (middle) and vertical components (bottom), indicating that we are unlikely to map azimuthal anisotropy into the variations of isotropic velocity and radial anisotropy.

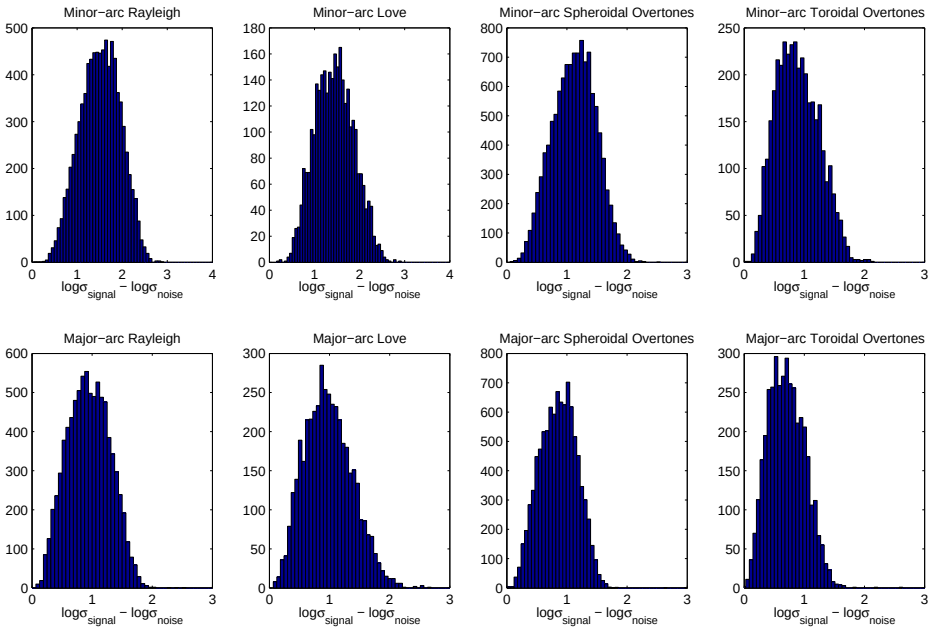

Figure 4.3: Histograms of the summary signal-to-noise ratios for each of the wavepacket types used in this study. The signal-to-noise ratios are approximated by taking the signal standard deviation (σ_{signal}) and dividing it by the noise standard deviation (σ_{signal}). We can see that even the least-well recorded wavepackets (second-orbit toroidal overtones) have noise levels below 20 %, while the minor-arc Rayleigh and Love waves have typical noise levels of only 3 %.

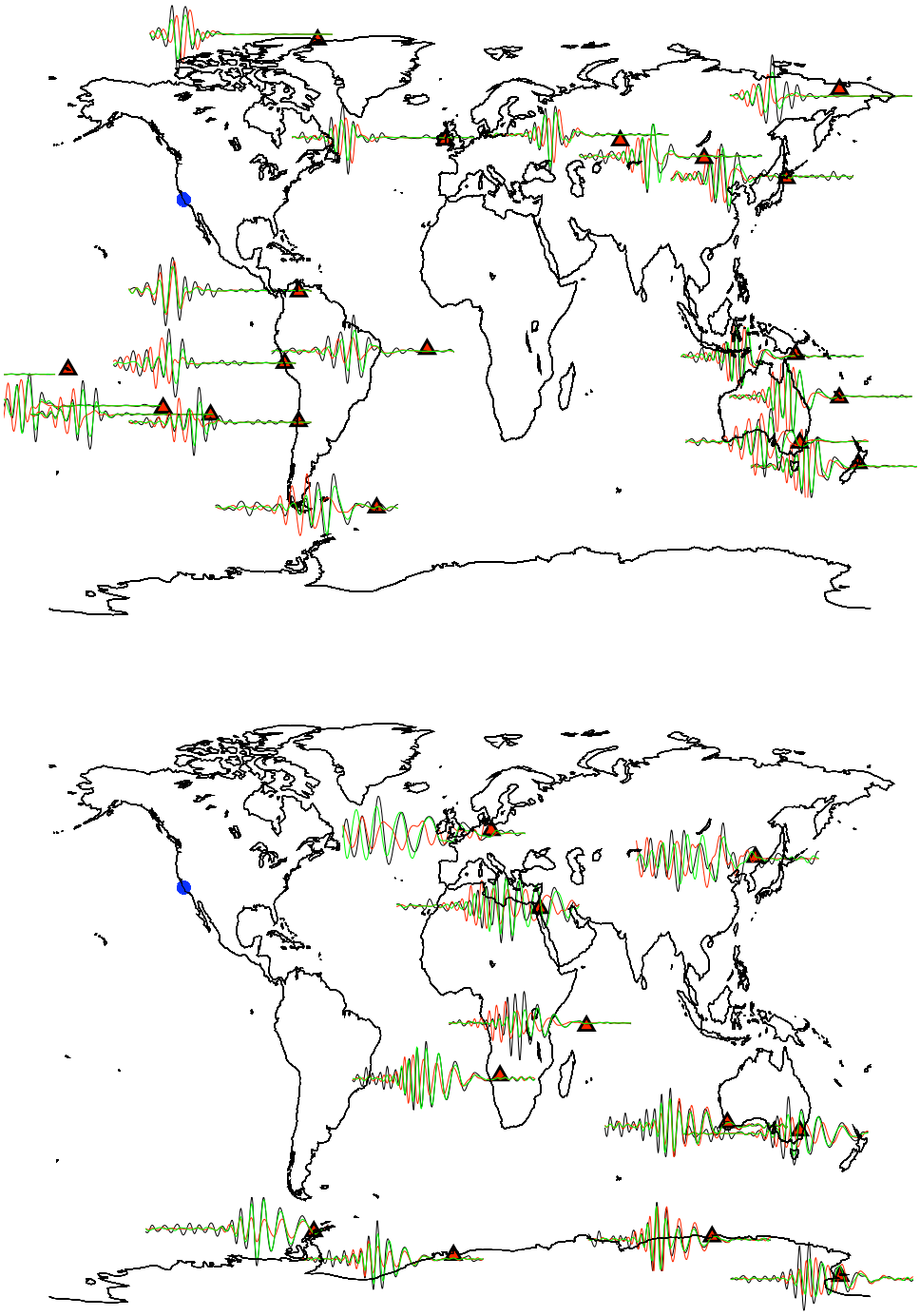

Figure 4.4: Observed minor arc (top) and major arc (bottom) Rayleigh waveforms (black) are compared to synthetic waveforms predicted by the starting model (red) and SEMum (green). The earthquake (blue) is the 2003 San Simeon earthquake and the station locations are marked by red triangles.

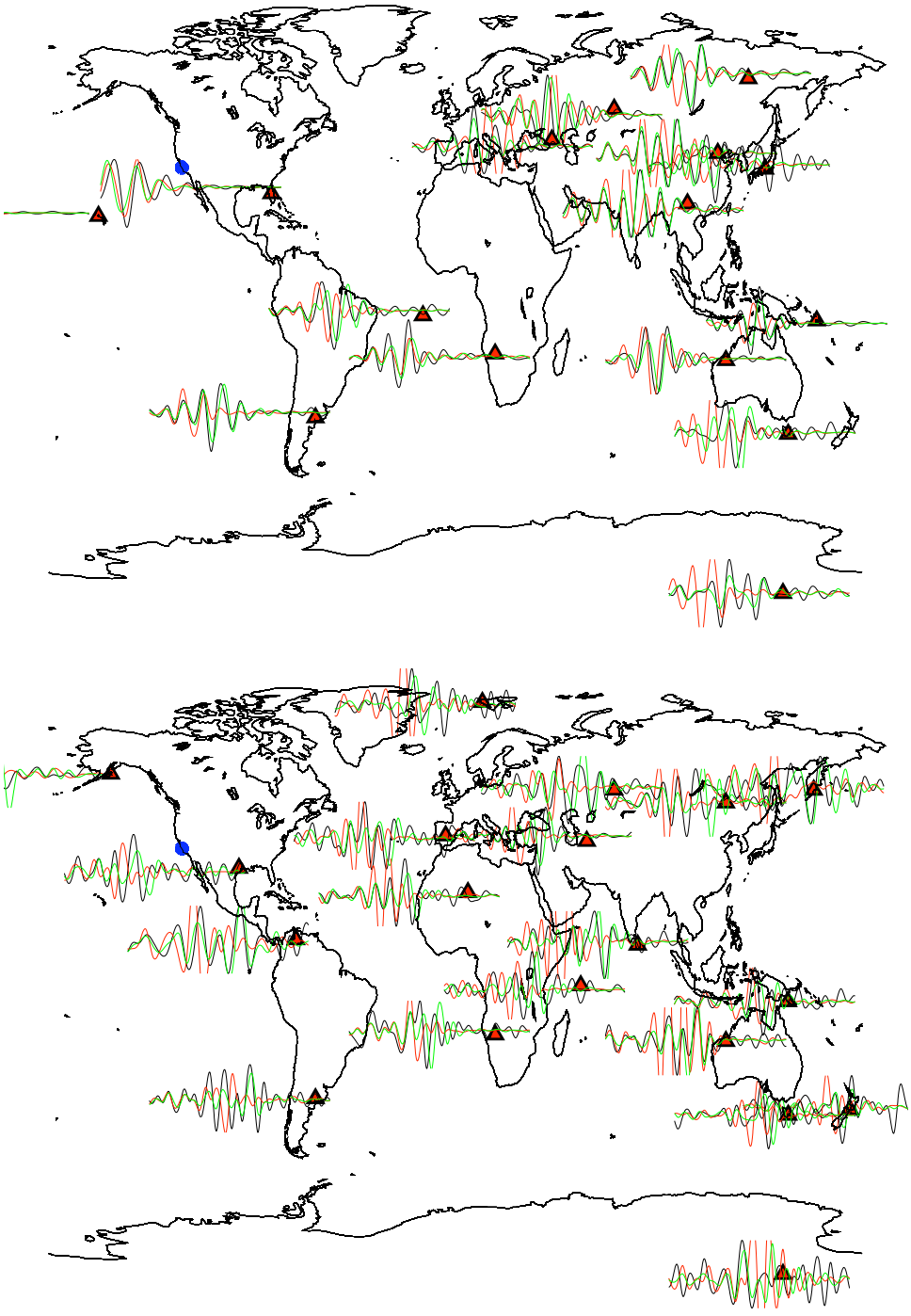

Figure 4.5: Observed minor arc (top) and major arc (bottom) Love waveforms (black) are compared to synthetic waveforms predicted by the starting model (red) and SEMum (green). The earthquake (blue) is the 2003 San Simeon earthquake and the station locations are marked by red triangles.

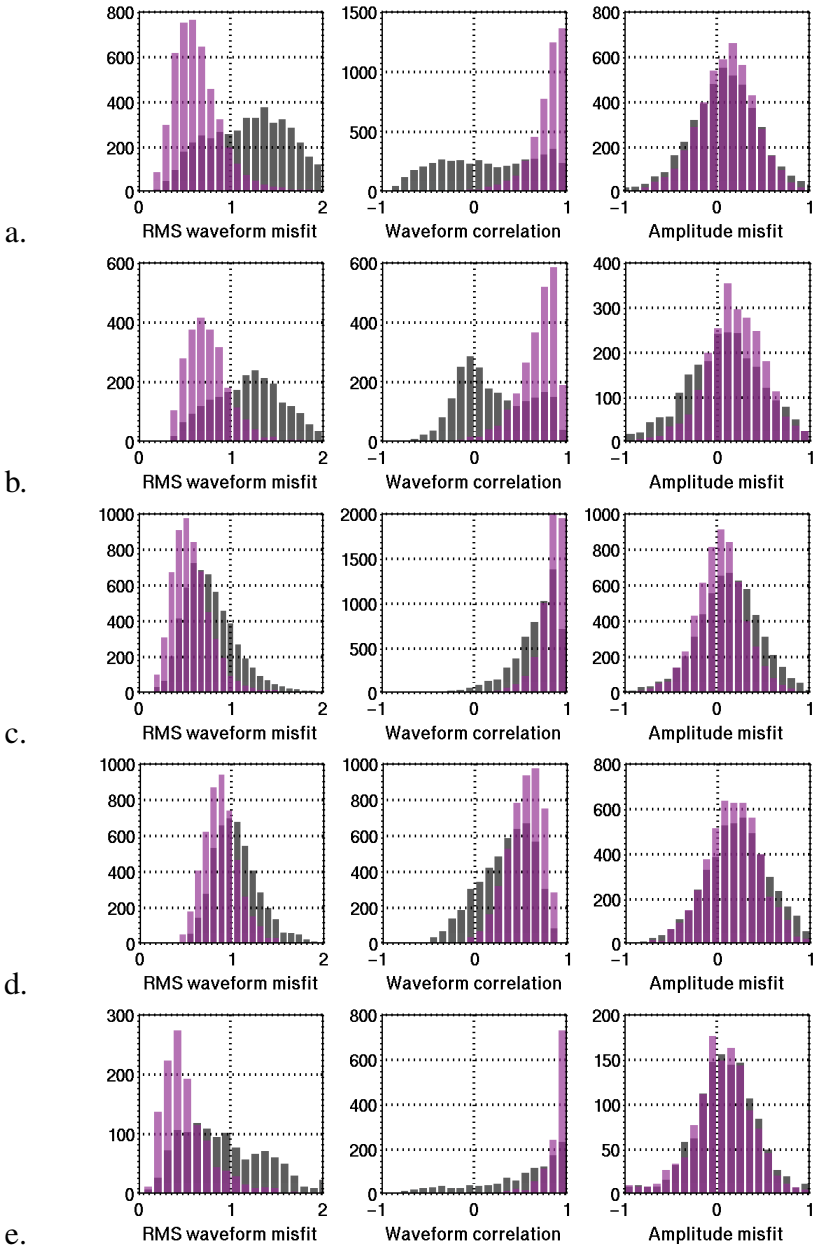

Figure 4.6: Measures of misfit between observed waveforms and those predicted by the starting model (gray) and SEMum (purple) for the vertical component. Left panels show histograms of root-mean-squared misfits normalized by the observed waveforms. The center panels show histograms of correlation coefficients between data and synthetics, which are only sensitive to phase alignment. The right panels show histograms of the natural logarithm of amplitude ratios between the data and synthetics (0=perfect fit). Different rows are for different wavepacket types: a. minor-arc Rayleigh waves; b. major-arc Rayleigh waves; c. minor-arc overtones; d. major-arc overtones; e. mixed.

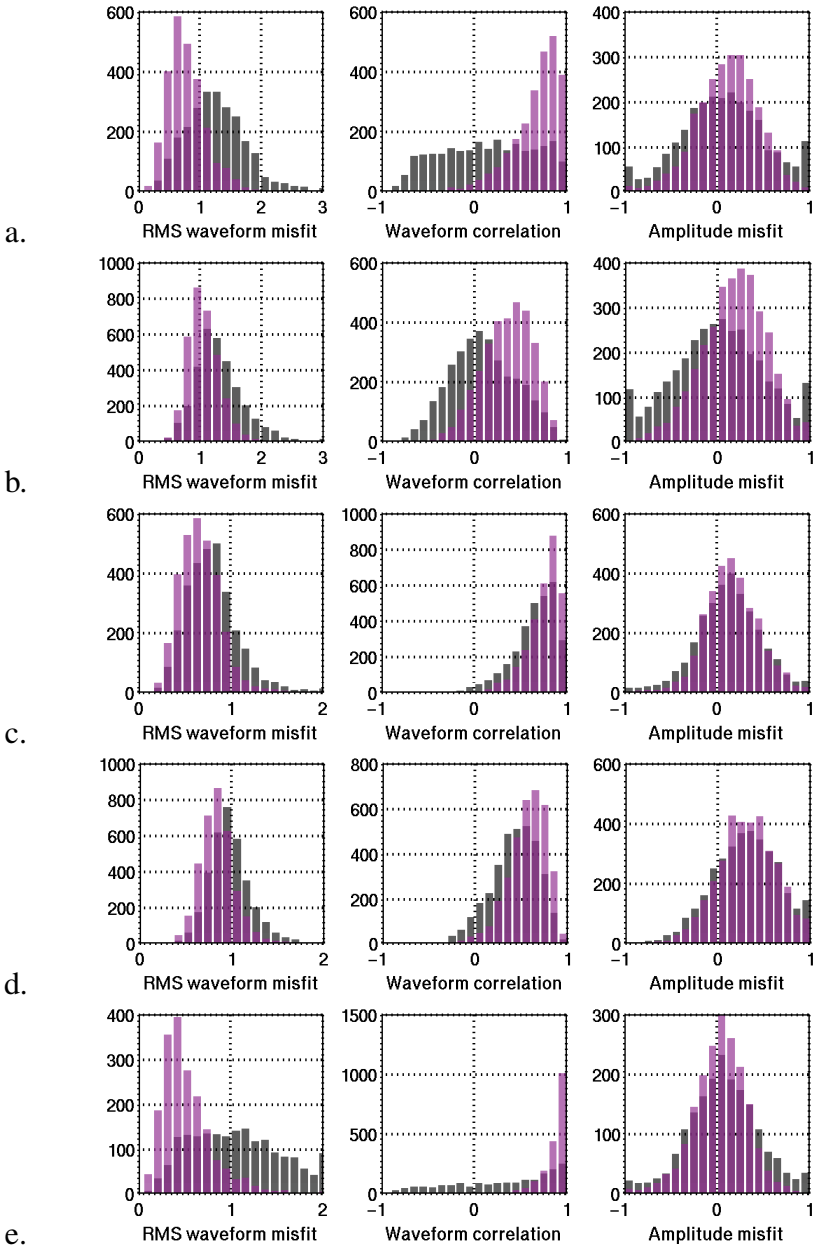

Figure 4.7: Measures of misfit between observed waveforms and those predicted by the starting model (gray) and SEMum (purple) for the transverse component. Left panels show histograms of root-mean-squared misfits normalized by the observed waveforms. The center panels show histograms of correlation coefficients between data and synthetics, which are only sensitive to phase alignment. The right panels show histograms of the natural logarithm of amplitude ratios between the data and synthetics (0=perfect fit). Different rows are for different wavepacket types: a. minor-arc Love waves; b. major-arc Love waves; c. minor-arc overtones; d. major-arc overtones; e. mixed.

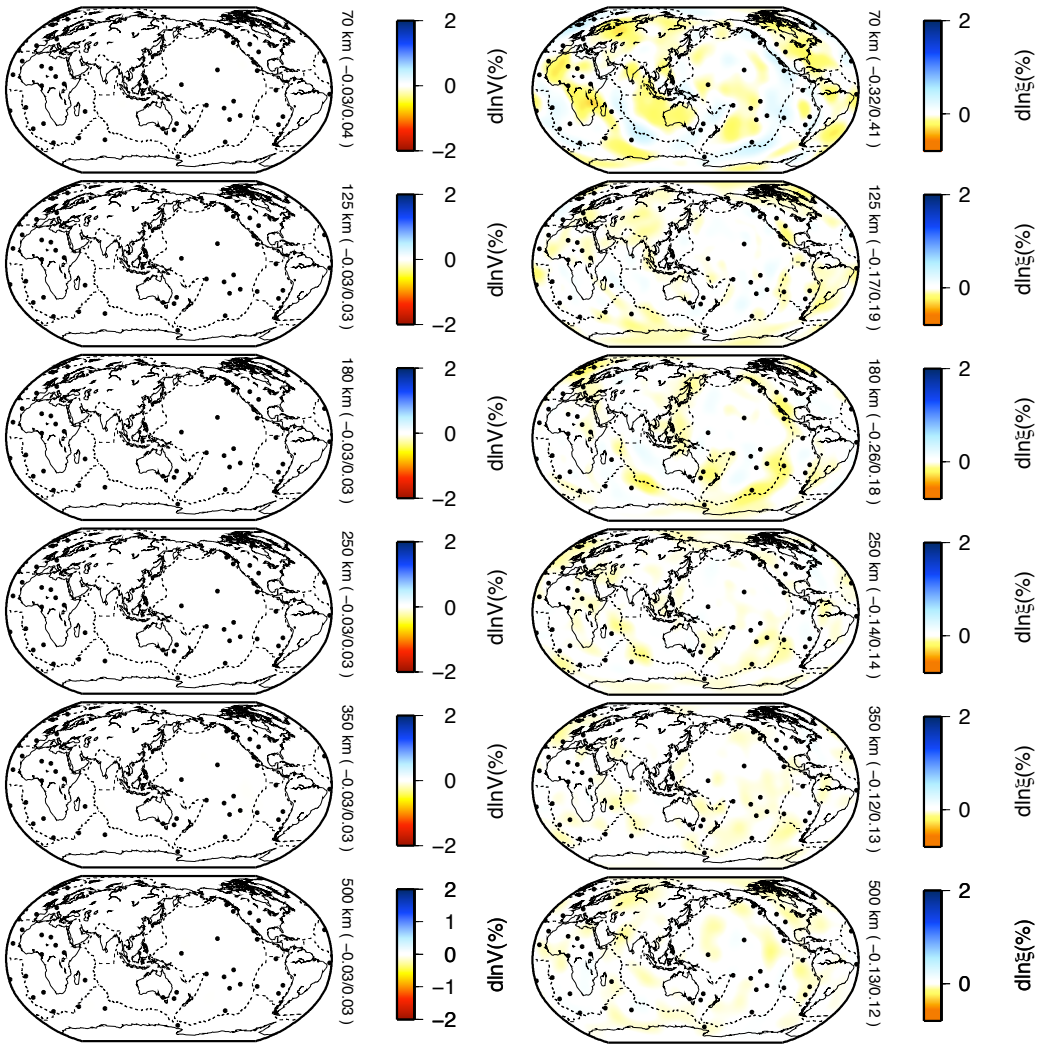

Figure 4.8: (left) Maps of output Voigt average shear wave-speed variations with respect to the average velocity at each depth that are retrieved for an input model with no V_S variations and ξ structure identical to that of SEMum. No significant contamination of V_S by anisotropic structure is therefore expected in SEMum. (right) Maps of radial anisotropy parameter ξ that are retrieved for an input model with no ξ variations and V_S structure identical to that of SEMum. Once again, no significant contamination of ξ by V_S structure is expected in SEMum.

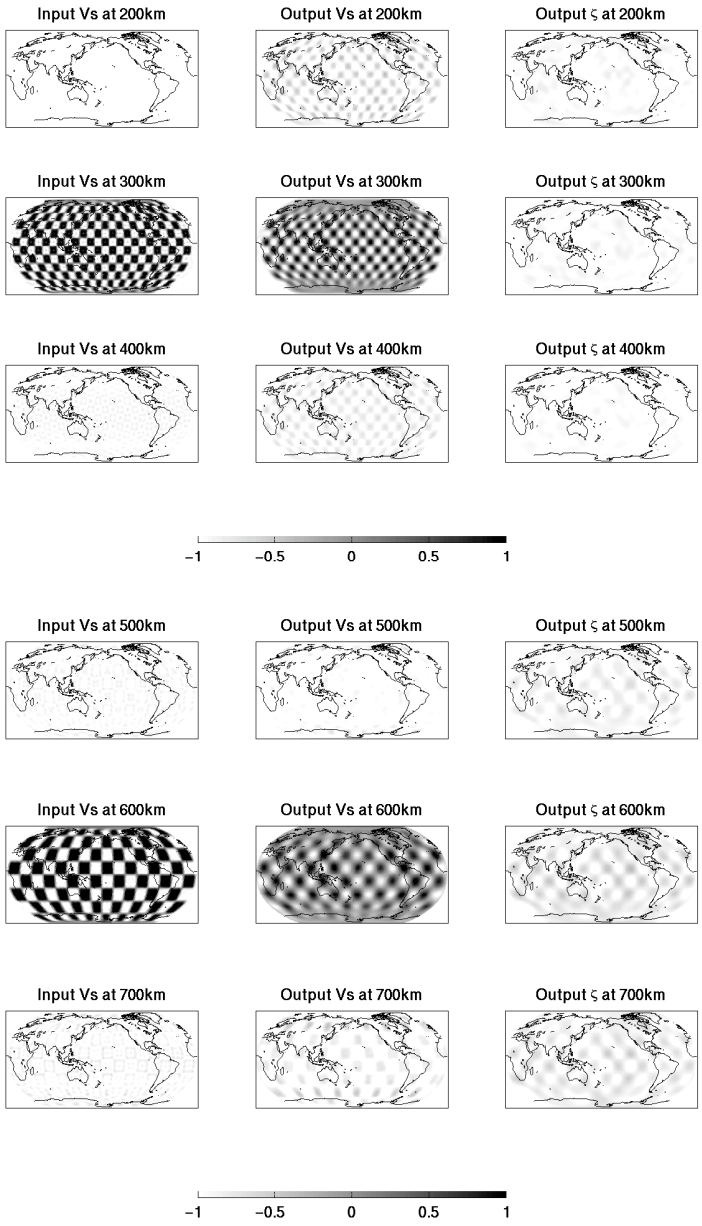

Figure 4.9: Tests of resolution of isotropic Vs structure. The input patterns are shown in the left column, the retrieved Vs pattern is shown in the center column, and the contamination of the anisotropic structure (ξ) is shown in the right column. These tests indicate that we robustly resolve anomalies of $\sim$1500 km across at 300 km depth, and $\sim$ 2500 km across at 600 km depth. Resolution is better at shallower depths. Furthermore, there is very little depth-smearing of structure ($< 100km$) and negligible mapping of Vs structure into ξ.

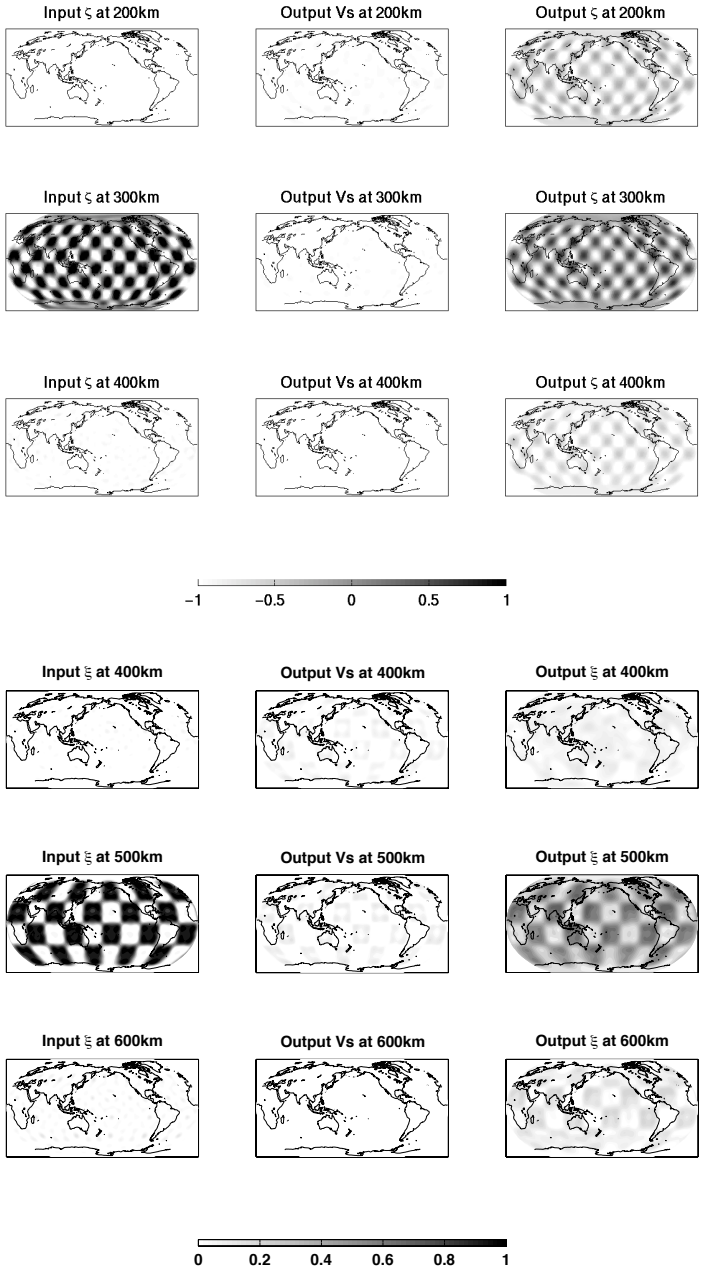

Figure 4.10: Tests of resolution of anisotropic parameter ξ. The input patterns are shown in the left column, the retrieved ξ pattern is shown on the right, and the contamination of Vs structure is shown in the center column. These tests indicate that we robustly resolve anomalies of $\sim$2500 km across at 300 km depth, and $\sim$ 4000 km across at 600 km depth. Resolution is better at shallower depths. While there is very little depth-smearing of structure ($< 100km$) and negligible mapping of ξ structure into Vs for well-resolved structures, both effects increase for shorter-lengthscale anomalies.

Chapter 5

A new upper mantle anisotropic model

5.1 Radial profiles of V_S and ξ

Figure 5.1 shows the retrieved profile of isotropic shear wave-speed and radial anisotropy of SEMum, compared to those of PREM, our starting model, and the latest 1D reference model developed by the Harvard group (REF: Kustowski et al., 2008). While the models show very good agreement at depths greater than 300 km, substantial differences exist at asthenospheric depths.

The V_S profile of SEMum is characterized by a rather narrow ($<$100 km) low velocity zone (LVZ) centered at a depth of $\sim$ 100 km, with slowest velocities of 4.4 km/s. The LVZ is bounded below by a rather steep velocity gradient, with velocities increasing by

$\sim$ 12.5 m/s/km down to $\sim$ 200 km depth. This velocity structure is not present in REF or our starting model. In PREM, the very large velocity jump associated with the 220 discontinuity, which is not thought to be a global feature, may well obscure a steep gradient that we observe. Indeed, the TNA model of Grand and Helmberger (1984), obtained by forward-modeling of waveforms that traverse the western United States is characterized by a very similar LVZ to that in SEMum, albeit with much lower minimum velocities as to be expected in a tectonically active region.

We leave for future work the intepretation of the radial velocity profile of SEMum in terms of thermal and compositional variations with depth. In particular, the inclusion of constraints from mineral physics (e.g. Cammarano et al., 2009; Xu et al., 2008; Cammarano et al., 2005) can shed light on whether the narrow asthenospheric LVZ of SEMum can be explained with temperature alone. A separate question is whether the large velocity gradients we find at the base of the LVZ are consistent with a purely thermal origin. Finally, is our velocity profile below 300 km consistent with a pyrolitic composition, or does it require enrichment in garnet-rich components as proposed by Cammarano and Romanowicz (2007).

We validate radial profiles of V_S and ξ of SEMum against measurements of frequencies of toroidal and spheroidal free oscillations on the first four overtone branches. Because we did not use any free oscillation frequencies in the inversion of SEMum, this represents an independent test of our model's predictive power. Figure 5.2 shows the predicted frequen-

cies of free oscillations for SEMum and PREM calculated using a modified MINEOS code (Woodhouse, 1998). On average, our model fits measured frequencies better than PREM, even though these were used in constructing PREM. The most dramatic improvement is in the fundamental mode spheroidal modes, which we match almost within measurement uncertainty at frequencies higher than 5 mHz, though this comes at the expense of slightly degrading the fits at longer periods (though we are always with 0.3% of the observed frequencies). Fits to the first overtone at long periods (3 mHz) for both spheroidal and toroidal modes are somewhat degraded, except for spheroidal modes at periods longer than 300 sec, where we note a modest improvement in fit. The fits for higher overtone branches are comparable to those of PREM.

No consensus exists concerning the radial profile of ξ in the upper mantle. The ξ profile of the model SAW642AN (Panning and Romanowicz, 2006) obtained by long-period waveform modeling using NACT mirrors that of PREM (see Figure 5.1), peaking at the top of the LVZ (below the fast lid associated with the lithosphere), and decreases down to unity by $\sim$ 220 km. Recent models obtained by the Harvard group (ND08: Nettles and Dziewoński, 2008; S362ANI: Kustowski et al., 2008), on the other hand, find anisotropy peaking at $\sim$ 120 km, decreasing above and below that depth, and nearly disappearing by $\sim$ 250 km. The ξ profile of SEMum is very different from that in PREM, showing peak values of ξ at a depth of 150 km, which is significantly deeper than the peaks in S362ANI and ND08. Like all of these models, we do not find that V_{SH} is substantially faster than V_{SV} on average at depths below 250 km.

The discrepancies between existing profiles of ξ can be due to a number of factors, including bias due to the use of different starting models, approximate treatment of kernels in a radially anisotropic medium, use of regional kernels, different approaches to performing corrections for crustal structure, as well as different regularization schemes and datasets used. We believe that our retrieved profile of radial anisotropy is likely to more closely represent the true variation of ξ in the mantle because we: 1. reduce bias by starting from a model found by a grid search to fit measured free oscillation periods; 2. reduce crustal contamination and inaccuracies inherent in approximate techniques by using the spectral element method for calculating wave propagation.

Independent indications of the likeliness of different radial anisotropy profiles can be gleaned from theoretical work. Becker et al. (2007) constructed models of radial anisotropy resulting from formation of lattice preferred orientation (LPO) due to mantle flow driven by prescribed plate velocities and by density differences scaled from variations of shear-wave velocity. They found that inclusion of lateral viscosity variations through a pressure, temperature and strain-rate dependent olivine creep law (assuming A-type slip systems, see Karato et al., 2008), significantly improved the fit to the seismic models. Whether or not the authors restricted LPO formation to dislocation creep or both dislocation and diffusion creep, radial anisotropy peaked at 150 km depth, deeper than that in S362ANI and ND08. This prediction, however, agrees with the depth of largest values of ξ in SEMum, providing further indication that we successfully characterize the profile of upper mantle anisotropy compared to previous studies.

Next, we describe the laterally-varying characteristics of our upper mantle anisotropic model SEMum. We analyze the model in the spatial (map) as well as the wavenumber domain, and consider separately the Voigt average shear velocity component and variations of radial anisotropy ξ.

5.2 Isotropic velocity variations

Figure 5.3 shows the isotropic shear wave-speed variations of SEMum with respect to the average velocity at each depth. The model confirms the long-wavelength upper mantle structures imaged previously with approximate techniques. The most prominent slow anomalies underly the mid ocean ridge (MOR) system down to a depth of less than 200 km. This confirms the findings of Zhang and Tanimoto (1992) but is inconsistent with the study of Su et al. (1992). The width of the low velocity zones associated with all the MORs widen with depth in the upper 150 km, though the widening is far greater beneath the faster-spreading East Pacific Rise system than it is under more slowly spreading Mid-Atlantic Ridge.

The back-arcs of all major ocean-ocean convergent boundaries are also characterized by slow velocities in the uppermost 200 km, though their signature is considerably weaker than that of the MORs. The back-arc of the Marianas subduction zone shows the most anomalously slow velocities at shallower depths while the low velocities associated with

back-arc spreading in the Tonga-Kermadec subduction zone increase in amplitude with depth and become dominant at 180 km. In contrast, subduction beneath South America shows no clear signature of a slow mantle wedge.

Finally, a number of localized low velocity features not clearly resolved in previous global shear wave-speed models can be see in the continents. At a depth of 70 km, a continuous band of low velocities can be seen running from the Tibetan plateau in the east, through the Hindu Kush, the Zagros Mountains, and terminating on the west beyond the Anatolian Plateau. At similar depths, we also image a low velocity channel running from the St. Helena hotspot underneath the Cameroon Volcanic Line and terminating in a broader low velocity zone underlying the Hoggar, Tibesti and Darfur hotpots. Finally, we find that the low velocities associated with Red Sea / East Africa rifting extend northward all the way to the Anatolian collision zone between 100-200 km depth.

Large-scale fast anomalies in the uppermost 200 km can be interpreted as signatures of either continental cratons and platforms or thickening oceanic lithosphere. Away from mid-ocean ridges, the ocean basins appear as seismically fast anomalies in the upper 100 km, with faster velocities persisting to greater depths with increasing age, consistent with cooling-induced lithospheric thickening (see, for example Shapiro and Ritzwoller, 2002). Seismically fast keels beneath stable cratonic regions were apparent in global tomographic models a quarter century ago (e.g. Woodhouse and Dziewonski, 1984), and remain one of the most prominent features of our tomographic model. Indeed, the biggest difference

between our model and other recent global tomographic studies is that the amplitude of the fast anomalies we observe beneath cratons is larger: up to 9% faster at 125 km depth. Despite their stronger amplitudes, however, we find that the signature of the cratonic keels weakens considerably below 200 km and disappears altogether around 250 km depth. This is consistent with the findings of Gung et al. (2003) and models based on heatflow measurements (e.g. Artemieva, 2006).

The spectral character of the velocity anomalies in the upper 200 km is shown in the left panel of Figure 5.4. In this depth range, the power peaks at degree 5, corresponding to the signature of the continent-ocean function, and falling off rapidly past degree 6 or 7. This confirms that the red spectrum of mantle heterogeneities discovered by (Su and Dziewonski, 1991) is a robust feature of the Earth and not an artifact due to the use of approximate forward modeling techniques. Power, including that at degree 5, decreases rapidly at depths below 200 km, consistent with the disappearance of the seismically fast continental keels and slow MORs.

Seismic structure in the 250-400 km depth range is weaker in amplitude has a decidedly whiter spectral character than more shallow structure. It is also uncorrelated with overlying structure, as can be seen in the radial correlation function in panel A of Figure 5.5. The most prominent fast anomalies appear to be associated with subduction of the Nasca slab beneath South America, the Australian-Indian plate beneath Java, and the Pacific plate beneath the Aleutians, Kuriles and Japan. Fast anomalies are also seen beneath Western Africa, though

they are rather weak and more diffuse than the overlying signature of the West African craton. Finally, fast anomalies are present in a few locations beneath the ridges encircling Antarctica, with the most prominent one being associated with the Australian-Antarctic discordance. In this depth range, strong ($\sim$ -3.5%) low velocities appear to concentrate in two regions: one centered in the south-central Pacific in the triangle formed by the Tahiti, Macdonald and Samoa hotspots and another centered beneath the Tanzanian segment of the East African Rift. Weaker anomalies are generally seen beneath the Pacific, and, to a lesser extent, the Indian ocean.

Fast velocity anomalies within the transition zone are dominated by the signature of subduction in the Western Pacific. These form a fast band running from Kamchatka in the northeast, over to Java in the west and beneath Fiji in the south-west. Additional strong fast velocities are seen beneath South America, associated with the subduction of the Nasca slab, and beneath the North American Cordillera, where they are likely to be associated with subduction of the Farallon slab. We image prominent slow anomalies in four broad locations of the transition zone. The first of these may be a continuation of the slow anomaly centered between Samoa and Tahiti. The second is a slow anomaly eastward of the Marianas/Japan/Kurile trenches, while a third stretches along the western margin of the Sumatra-Andaman/Java trench system. The fourth slow anomaly can be seen beneath the northwestern Atlantic abutting the North American shelf.

In the wavenumber domain, the combined signature of the seismic anomalies within the

transition zone presents itself as an increase in power at degrees 4-8 (see Figure 5.4), which is different from the dominantly degree 2 character of the anomalies inferred by Kustowski et al., 2008. This difference may be due to the fact that our dataset does not include body waves at frequencies shorter than 60 sec, which may make it difficult to retrieve the amplitude of the fast, subduction-related anomalies in the Western Pacific.

5.3 Depth to the Lithosphere-Asthenosphere Boundary

The recent study of compressional-to-shear (Ps) conversions beneath a globally distributed set of stations carried out by Rychert and Shearer (2009), has reignited a long-standing debate concerning the thickness of the lithosphere beneath continents (see Romanowicz, 2009). Ps receiver function techniques (Vinnik, 1977) are capable of detecting the depth and sign of sharp velocity contrasts beneath seismic stations. Rychert and Shearer applied the technique to a global dataset with the goal of identifying velocity-decreases with depth, which are thought to represent the boundary between the seismically fast lithosphere and slower asthenosphere (lithosphere-asthenosphere bounday: LAB). They found little variation in the depth of a discontinuity they associated with the LAB between cratonic regions ($\sim$ 95 km) and oceanic islands ($\sim$ 70 km). Beneath the oceans, these estimates of LAB depth are in agreement with other studies (Kawakatsu et al., 2009), and falsify the claims of McKenzie and Priestley (2008) that the LAB is undetectable with receiver-function meth-

ods. However, beneath coninents, their observation appears to conflict with the images of seismically fast keels extending beneath the cratons to a depth of at least $\sim$ 200 km (see, e.g. Gung et al., 2003).

Even when interpreted from global shear wave tomographic models, very different maps of LAB depth can be obtained when different available seismic models are used. Gung et al., 2003 pointed out that the tomographic models could be separated into distinct categories, with those derived from vertically-polarized shear waves showing cratonic keels to extend to shallower depths $\sim$200 km than models including horizontally-polarized waves. Based on this difference and maps of variations of radial anisotropy that showed regions of $V_{SH} > V_{SV}$ beneath cratons, Gung et al. (2003) argued that the LAB beneath cratons was likely to be in the $\sim$200-250 km range, and that the deep tectosphere proposed by Jordan, 1978 does not extend down to 400 km. This agrees with arguments put forth by Ricard et al., 1996 on the basis of the ability of the 3SMAC model to predict seismic data.

Resolution tests show that our model of variations of isotropic shear wave-speed is not biased by anisotropic structure, making it suitable for determining LAB depth without contamination related to the influence of anisotropy. A number of methods have been used to estimate LAB depth from tomographic models. Weeraratne et al. (2003) chose the depth of the largest negative gradient of velocity with depth as a proxy for the location of the LAB, while Artemieva (2009) and Conrad and Lithgow-Bertelloni (2006) associated the LAB with the 2% fast isosurface in recent tomographic models. Pasyanos (2009) inverted

group velocity dispersion data directly for radial profiles of velocity with a variable depth to LAB. Other studies have used theoretical or empiricial relationships relating seismic velocity to pressure and temperature, and then extrapolated conductive profiles within the lithosphere to the depth at which the intersect the mantle adiabat (Priestley and McKenzie, 2006), which depth is then taken to be the LAB. Finally, changes in the direction of azimuthal anisotropy have been associated with the base of the cratonic lithosphere beneath North America (Marone and Romanowicz, 2007) and Africa (Sebai et al., 2006).

We choose the simple, gradient-based method of Weeraratne et al. (2003), since it does not rely on the arbitrary choice of a special "LAB" velocity anomaly threshold. Furthermore, associating the LAB with the region of the most negative velocity gradient is a reasonable approach for identifying a velocity jump in a smoothly parameterized model, and is not subject to the either the uncertainties associated with relations between shear wave-speed and temperature/composition or the extrapolation of conductive thermal profiles through the lower crust, whose abundances of radiogenic isotopes is poorly known. Figure 5.6 shows the inferred LAB depth obtained by extracting the absolute isotropic shear wave-speed profile at each point on the Earth, and finding the depth at which the gradient of velocity is most negative, with the constraint that this depth fall between 50 and 300 km depth.

Figure 5.6 shows a strongly bimodal distribution of LAB depths. Beneath the oceans, lithospheric thickness ranges from 50 up to 80 km, with regions away from MORs showing

thicker lithosphere. Beneath continents, a much greater range of lithospheric thicknesses is apparent. Shallowest LAB ($\sim$ 80 km) is found beneath north and east Africa, western Europe, far eastern Asia and Australia. Somewhat deeper ($\sim$ 100 km) LAB can be seen beneath most of central North and South America, in central Siberia, Iran, Iraq and stable Saudi Arabia, as well as in western and southern Africa. In these continental regions, it may not be appropriate to associate the LAB with the depth of the most negative gradient of velocity, since negative gradients exist at both $\sim$ 100 and 250 km depth (see discussion of regional profiles). The real LAB, therefore, is likely to be at 250 km depth, while the negative gradient of velocity at $\sim$ 100 km may be the origin of the signal observed by Rychert and Shearer (2009) that caused them to mistakenly interpret their results as evidence for anomalously thin lithosphere beneath stable continents (see Romanowicz, 2009).

Thick lithosphere is found beneath Quebec, eastern North America, the Sao Francisco craton, the eastern portion of the East Siberian craton, the western, archean portion of the Australian craton, and in the broad region of continental collision between India and Asia. Thickest lithospheric regions are found beneath northern North America, northern Greenland, the East European craton, the western portion of the East Siberian craton, the West African, Congo and northern Kalahari cratons, the Amazonian and Australian cratons, as well as the craton beneath Eastern Australia.

Our map of LAB depth is broadly consistent with the seismologically-based estimates of Pasyanos (2009), McKenzie and Priestley (2008) and Figure 5b,c of Artemieva (2009).

However, a detailed examination of our inferred LAB depths shows a number of important differences with the results of Priestley and McKenzie (2006). The most important of these differences is that Priestley and McKenzie (2006) find that the regions of thick lithosphere associated with individual cratons form continuous, very large provinces of very thick lithosphere, which they term "cores". In particular, the Congo, Kalahari and Tanzanian cratons of Africa appear to be one "core", and the East European craton and the East Siberian craton form an enormous "North Eurasian core". Our map of inferred LAB topography shows that these cratons are in fact distinct even at depth, and that they are separate by regions of much thinner ($\sim$ 100-125 km thick) lithosphere.

These results also agree with the heatflow-based TC1 model (Artemieva, 2006), which shows thick lithosphere in all the regions where we infer a deep LAB, except for beneath Mexico and the Celebes Sea, where our inferences are very likely corrupted by the signature of active subduction in these regions. The most striking difference between our inferred map of the LAB is that the deep cratonic keels are of much larger scale than those present in TC1.

5.4 Variations of radial anisotropy

Figure 5.3 shows the variations of the anisotropic parameter ξ with respect to isotropy at a variety of depths. Regions where $\xi > 1.0$ (shown in blue hues) are ones in which horizon-

tally polarized waves travel more rapidly than vertically polarized ones, i.e. $V_{SH} > V_{SV}$, and ones with $\xi < 1.0$ (shown in orange hues) have $V_{SV} > V_{SH}$. If this seismic anisotropy is due to lattice preferred orientation (LPO) of olivine crystals induced by flow-driven deformation, then blue regions of Figure 5.3 are ones in which the direction of the time-integrated longest finite strain ellipsoid is in the horizontal plane (e.g. see Ribe, 1989, 1992). However, because the dominant slip systems that give rise to LPO are themselves sensitive to temperature, pressure, strain-rate and volatile-content, a variety of slip systems might be operative in the upper mantle, complicating the interpretation of anisotropy (see Karato et al., 2008).

Before proceeding to describe and discuss the spatial characteristics of variations in ξ, it is interesting to consider the spectral character of the model and compare it with that of the isotropic velocity variations. The right panel of Figure 5.4 shows the power of the anisotropic model as a function of angular degree, and colored on a logarithmic scale. At a depth of 100 km, the spectrum is rather white, and is markedly different from the red spectrum of isotropic velocity variations. Below about 125 km, almost the entire power of the anisotropic model at other depths is contained in degrees 2-6, even though the model parameterization allows for structure up to degree 24. Finally, very little power is present at depths greater than 300 km, confirming previous results of Panning and Romanowicz (2006) and Kustowski et al. (2008) that lateral variations of ξ are not strongly required by the data at these depths.

It is immediately apparent that the uppermost $\sim$ 200 km are characterized by $V_{SH} > V_{SV}$, as seen in the radial profiles of ξ, presented earlier. This is consistent with the dominantly horizontal deformation induced by the motion of lithospheric plates over the asthenosphere. Indeed, our model does not show any large regions with $V_{SV} > V_{SH}$ until below 200 km depth. That is not to say that the model in the upper 200 km is featureless. In fact, substantial differences in the anisotropic signature of continents and oceans are clearly present in this depth range.

First, continental regions appear to have larger values of ξ in the uppermost 100 km than do oceanic regions, which are essentially isotropic away from the MORs. This observation is complicated somewhat by our smooth parameterization of crustal structure, which can only match the seismic response to that of a layered crust with the introduction of spurious anisotropy. However, we believe that this effect is not dominant at a depth of 100 km. A possible explanation is that since seismic anisotropy depends not on the present but rather the time-integrated finite strain, the strength of anisotropy in the shallow continental lithosphere is the result of it having been subjected to more deformation over its considerably older age than has the oceanic lithosphere.

The second feature of interest that can be seen in the 70 km map of Figure 5.3 is that the mantle wedges of the Western Pacific have decidedly greater values of ξ than do the surrounding oceans. This is also the case in the S362ANI model of Kustowski et al. (2008). It is not immediately apparent why the mantle wedges should have ξ larger than 1.0 when

the opposite sense of anisotropy is predicted by Becker et al. (2007) based on A-type slip in olivine (alignment of fast axis with the direction of flow). This prediction is based on the preponderance of vertical deformation associated with subduction. One possibility is that the A-type fabric might not be dominant in subduction zones, and instead the B-type or C-type fabrics dominate, aligning the fast axis perpendicular to the vertical flow. This may be a plausible explanation, since mantle wedges have high water content (e.g. Hirschmann, 2006) favoring B- and C-type fabric formation (Katayama and Karato (2006)).

Mid ocean ridges at depths shallower than 100 km appear to have somewhat larger ξ values than the ocean basins, though their signature is less strong than that associated with the subduction zones. This character of MORs is also seen in S362ANI, and is also seen in the modeling of Becker et al. (2007). It results from A-type olivine fabric formation within a dominantly horizontal flow induced in the vicinity of spreading centers by the motion of the overriding oceanic lithosphere. However, it is surprising that the strength of the MOR ξ anomalies appears to be comparable across all the MORs, regardless of the spreading rate, which is predicted to be strongly correlated with ξ by Becker et al. (2007).

Finally, a band of anomalously high ξ and trending northwest-southeast across central Pacific can be seen in the 70 km map of Figure 5.3. We do not have any ready explanation for this feature, and note that it has not been previously reported. However, we note that it may be associated with the strong $\xi > 1.07$ anomaly centered beneath Hawai'i, first imaged by Ekstrom and Dziewonski (1998) and seen in the models of both Kustowski et al. (2008)

and Panning and Romanowicz (2006).

At 125 km, the ocean basins become the locus of highest values of ξ, while the continents appear more isotropic than at shallower depths. Greatest anisotropy is seen under the Pacific, centered beneath Hawai'i. However, we observe a second maximum beneath the Indian ocean, centered south of India on the equator. This strong $V_{SH} > V_{SV}$ anomaly is clearly imaged by Gung et al. (2003), but is less strong in both Kustowski et al. (2008) and Panning and Romanowicz (2006). At this depth, the MORs and subduction zones are not easily distinguished, and are characterized by ξ values in the 1.04-1.07 range.

By 180 km, the continents appear to be nearly radially isotropic, while the ξ values underneath the oceans increase further, reaching a maximum of ~ 1.12 beneath both the Pacific and the Indian Ocean, and somewhat lower values beneath the Atlantic Ocean. The most notable feature of the variations in radial anisotropy in this depth range is the emergence of three nearly isotropic regions: one beneath the backarc associated with subduction beneath Tonga-Kermadec, a second one near the western edge of the Southeast Indian Ridge, and a third one in the general vicinity of the triple junction among the East Pacific Rise, the Pacific-Antarctic Ridge, and the Juan Fernández Ridge.

These three isotropic regions become more anomalous with increasing depth and by 250 km show clear evidence of $\xi < 1.0$. Other regions with $\xi < 1.0$ can also be seen at a depth of 250 km: a band running along the western margin of both North and South America from the Yukon in the north to central Chile in the south, and another, east-west trend-

ing band stretching from Iran in the west through China, Mongolia and Manchuria in the east. All of these regions appear to be associated with either spreading or subduction, and it is likely that their anisotropic signature is indicative of the prevalence of vertical flow. This can be seen in another way by looking at the cross-correlation between the isotropic and anisotropic structure shown in panel C of Figure 5.5: anisotropic structure below 200 km depth is moderately-well correlated with seismic structure in the upper 200 km, because the regions of anomalous $V_{SV} > V_{SH}$ anisotropy are preferentially located in regions associated with either spreading centers or subduction/convergence zones which are characterized by shallow low isotropic velocity anomalies. Beneath the MORs, we expect this flow to be upward, while it is reasonable to expect flow to be downward in regions of convergence/subduction. We note that these regions are broadly consistent with the models of Gung et al. (2003) and Panning and Romanowicz (2006), and to a lesser extent that of Kustowski et al. (2008).

At this depth, the character of anisotropy beneath the oceans also changes substantially; whereas the mantle beneath Hawai'i hosted largest ξ anomalies at 150 km, now it is conspicuously isotropic, separating broad swaths with larger ξ values to the east and the west. Furthermore, large values of ξ appear to persist to greater depth beneath the Indian Ocean and the western margin of the North Atlantic, than they do beneath the Pacific Ocean. The substantial differences in the ξ model between the upper 200 km and deeper structure is clearly seen in the radial correlation functions shown in panel B of Figure 5.5. No substantial lateral variations of radial anisotropy are found below $\sim$ 300 km.

5.5 Comparison with regional models

5.5.1 Africa

Africa is the site of four main cratons, several hotspots and active continental rifting. As such, the upper-mantle structure beneath Africa has been re-examined in the last few years by a number of continental-scale tomographic studies (e.g. Priestley et al., 2008; Pasyanos and Nyblade, 2007; Sebai et al., 2006). We compare our findings with inferences made in these studies and focus our attention on three salient tomographic features: 1. the differences in depth extent of seismically fast keels that underly cratons; 2. the depth extent and morphology of seismically slow anomalies beneath the East African Rift; and 3. the relationship between upper mantle velocity and Africa's hotspots.

Even though they were first imaged a quarter century ago (Woodhouse and Dziewonski, 1984), controversy still brews concerning the depth extent of the seismically fast keels beneath the West African, Congo, Tanzanian and Kalahari cratons. Based on waveform inversion of long period Rayleigh waves, Priestley et al. (2008) argue that the fast roots extend to depths of 225-250 km beneath all but the Kalahari craton, below which they retrieve fast anomalies only down to $\sim$170 km. This finding is in conflict with the study of Sebai et al. (2007), which found fast anomalies beneath the Tanzanian craton to be of anomalously shallow extent ($\sim$ 180 km), in agreement with earlier findings by Weeraratne et al. (2003) which study was focused on Tanzania. Finally, Pasyanos et al. (2007) use

a very large dataset of group velocity dispersion measurements to image both crustal and upper mantle structure beneath Africa; they find that the Congo craton is the anomalous one, with a weak signature in the upper mantle.

Figure 5.7 shows map views of our model at 6 depths. At 150 km depth, all four African cratons are clearly seen to be underlain by fast anomalies. However, by 200 km, the signature of the Tanzanian craton is gone, and the fastest anomalies have shifted northeastward into Mozambique. This is consistent with the findings of Pasyanos et al. (2007) and Priestley et al. (2008) concerning the Kalahari craton, and confirms the shallow extent of the Tanzanian craton, as found by Weeraratne et al. (2003) and later Sebai et al. (2007). However, contrary to the findings of Pasyanos et al. (2007), we see a robust signature of the Congo craton extending down to $\sim$ 220 km.

The most pronounced slow anomalies shown in Figure 5.7 are associated with the Red Sea and the East African Rift. At depths shallower than 150 km, these trend northwest-southeast and are concentrated beneath the Red Sea and the Ethiopian segment of the East African Rift. Starting at $\sim$ 200 km, however, they assume a north-south trend and move progressively southward with depth, extending into Tanzania, where Weeraratne et al. (2003) found evidence for the presence of a mantle plume. This behavior is also seen by Sebai et al. (2007) and Pasyanos et al. (2007), but is not present in the model of Priestley et al. (2008), where the southern East African Rift is underlain by fast velocities at depths below 200 km. In the transition zone, we find slowest velocities beneath Tanzania, where

they assume a circular morphology consistent with the presence of a deep plume.

We observe secondary slow anomalies trending from St. Helena hotspot, through Mt. Cameroon and the Tibesti hotspot. These slow anomalies separate the fast keels of the West African and Congo cratons, and are also present beneath the Darfur and Hoggar hot spots. The upper mantle signature of the African hotspots is present in both the model of Priestley et al. (2008) and that of Pasyanos et al. (2007), but is absent in the tomography of Sebai et al. (2007).

5.5.2 South America

The South American continent comprises two main cratons: the Amazonian craton which stretches from southeastern Venezuela down to northeastern Bolivia, and the Sao Francisco craton in eastern Brazil. The Amazonian craton is itself separated by Amazonian rifting into a northern Guyana and southern Guapore shields. Further south, the Parana basin is the site of one of a major Large Igneous Provinces (LIP). Active subduction of the Nasca plate dominates the tectonics of the western margin of the continent forming the Andean Cordillera. The strike of this subduction changes dramatically between Chile and Peru, and is associated with a change in the morphology of the Wadati-Benioff zone (see Lekic, 2004).

Figure 5.8 shows map views of our model at 6 depths. In the uppermost mantle, we find

slowest velocities beneath the East Pacific Rise, and along the Carnegie and Cocos Ridges, which meet at the Galapagos hot spot. Other slow velocities are observed in the vicinity of the San Felix and Juan Fernandez hotspots, though these cease to be anomalously slow between 150 and 200 km depth. The Mid Atlantic Ridge appears to be characterized by moderately slow velocities to a depth of less than 200 km. At 75 km depth, all of South America, except the Altiplano, is underlain by seismically fast anomalies, which, by 150 km depth appear to be centered beneath the Amazonian and Sao Francisco cratons. Unlike the regional study of Heintz et al. (2005), we do not image a less fast band along the Amazonian rift separating the Guyana and Guapore shields. The seismic signature of both cratonic keels narrows and shifts to the East with increasing depth, and disappears altogether deeper than $\sim$ 200 km.

We image the Nasca slab at 150 km depth, though at a depth of 200 km one of the most prominent features is not the slab itself, but, rather, a slow anomaly centered immediately to the east of the bend in the trench. This slow anomaly is also present in the model of Heintz et al. (2005), and might obscure the fast anomalies associated with the slab. At greater depths, this anomaly spreads to the southeast, where it underlies the Parana LIP. Heintz et al. (2005) also observe slow velocities, though in a more restricted region, that they interpret at a mantle signature of the Parana LIP. In the transition zone, a broad, fast, north-south oriented feature is seen, probably due to the presence of the Nasca slab; deep seismicity is seen throughout the region covered by the fast anomaly. At depths below 500 km, a slow anomaly is present beneath the eastern edge of the Parana LIP, in agreement

with P and S-wave regional traveltime tomography of Schimmel et al. (2003).

5.5.3 North America

North American upper mantle has been mapped by a number of recent surface wave studies (Godey et al., 2004; Marone et al., 2007; Nettles and Dziewoński, 2008; Bedle and van der Lee, 2009; *Yuan and Romanowicz, in prep.*). Figure 5.9 shows maps of the isotropic shear wave-speed variations of SEMum. The most prominent seismic feature in the 200 km beneath North America, and one that is imaged by all of the recent tomographic studies, is the sharp contrast between the tectonically active and seismically slow western region and the seismically fast, stable continental platform to the east. However, the details of velocity variations within each region differ between models.

At 75 km, our model shows two regions of especially fast velocities beneath the stable continent: a northwestern one in the vicinity of the Slave craton, and a larger, faster one centered on the southern shore of Hudson Bay in the location of the Superior craton. We image a third craton beneath northwest Greenland. The craton locations are broadly consistent with the morphology of fast anomalies imaged in the aforementioned regional studies. By 150 km, the fastest anomalies appear to merge, shifting somewhat northward, directly beneath Hudson Bay. At 200 km, the fastest velocities are seen in a circular region centered on the western shore of Hudson Bay, and persist until $\sim$ 250 km before becoming indistin-

guishable from ambient mantle. The Greenland craton loses its fast signature between 200 and 250 km depth.

A number of smaller-scale features can be seen in the seismically slow western portion of the continent. The most striking of these is a less-slow band at 75 km which stretches from the California coast toward the Pacific. We see a sharp drop of velocities across the Mendocino Transform Fault that separates the Pacific plate from the Juan the Fuca plate to the north. The southern edge of this band occurs at the tip of active rifting occurring in northern Gulf of California. Because this feature appears to be confined to the strike-slip San Andreas Fault plate boundary, and its signature disappears below 150 km depth, we interpret this feature as the manifestation of colder oceanic lithosphere that is no longer subject to active spreading occurring to the north and the south.

In the east, slow velocities are seen in a narrow band around the Mid Atlantic Ridge. Finally, a small, circular low velocity anomaly is imaged in the vicinity of Bermuda. This anomaly may be associated with a weak, northwest-southeast trending band of slow anomalies that splits the domain of fast anomalies running from northern Quebec to south of the Great Lakes, before petering out near Lake Erie. Though this feature appears to persist until a depth of 200 km, it is not clearly seen in any of the regional models.

The slow anomalies seen beneath the Basin and Range disappear between 200 and 250km, which is somewhat shallower than the signature of the slow anomalies further to the west and south. Nevertheless, our model shows that western North America is clearly noma-

lously slow to a depth of 200-250 km, which is also found by Nettles and Dziewoński, 2008 and Bedle and van der Lee, 2009 but is opposite to the maps of Godey et al., 2004.

In the transition zone, we image a northwest-southeast trending fast anomaly that stretches from the Cascadia subduction zone down to the Gulf of Mexico. We interpret this to be a signature of the Farallon slab. The location of this fast anomaly is roughly consistent with the images of the slab-related fast anomalies imaged using the finite-frequency, teleseismic P-wave traveltime model of Sigloch et al., 2008. Two strong slow anomalies are also seen in this depth range: one beneath the central segment of the East Coast of North America, stretching from Massachusetts in the north, down to southern Virginia, and a second, smaller anomaly beneath western/central California.

5.5.4 Australia

A favorable distribution of earthquakes that occur at a large range of depths along the Tonga-Kermadec and Vanuatu subduction zones to the east and the Solomon Islands, Papua New Guinea, Banda Sea and Java subduction zones to the north, has aided the development of tomographic models of the mantle structure beneath Australia. We will compare our inferred velocity structure beneath Australia with three recent surface-wave based tomographic studies of the continent's upper mantle structure (Simons et al., 2002; Fishwick et al., 2005; Fichtner et al., 2009b). All three of these studies use only vertical component

seismograms, and are thus models of vertically-polarized shear wave-speed variations. The model of Fichtner et al., 2009b (henceforth FAU) is, like our model, developed using the spectral element method, though there are a number of important differences between our approaches: 1. we use 3 component data, whereas FAU uses only vertical component seismograms; 2. we initialize our inversion with 1D model, whereas FAU start from a 3D model that shares much of the features of their final model; 3. we use approximate finite frequency kernels calculated using NACT as opposed to the adjoint kernels used by FAU; 4. our misfit function is a waveform difference calculated point-by-point in the time domain, whereas FAU use a more complicated technique that calculates time-frequency misfits.

Figure 5.10 shows map views of our model at a variety of depths. At 75 km depth, we see very low velocities associated with spreading occurring along the Pacific-Antarctic and Southeast Indian Ridges, as well as the Tonga-Kermadec back-arc. All of Australia is characterized by faster-than-average velocities, except the easternmost margin and the south-east region near Tasmania. Simons et al., 2002 (henceforth SAU) and Fishwick et al., 2005 (henceforth FSW) both find low velocities beneath Tasmania at this depth, though FAU does not. The fast anomalies in the bulk of the continent show a less-fast central region, flanked by fast anomalies to the north, east and west (but not south), consistent with findings of FAU and FSW but not SAU, whose model appears more or less-uniformly fast in the entire region west of the Tasman Line. FSW argue that these lower velocities in the central portion of Australia are confirmed by body wave data.

At 150 km, central and western Australia (west of the Tasman Line) is seismically fast, with the fastest velocities concentrated in an east-west elongated region. This fast anomaly has a similar shape and amplitude in all of the regional studies. At this depth, we also start to image the subducting slabs beneath Java, the Banda Sea and Vanuatu, though the Tonga slab is not seen to be anomalously fast. This may be due to the strength of the low velocities associated with back-arc spreading, whose amplitude increases with depth, peaking between $\sim$ 150-200 km depth. Of the three regional studies, only the model of FAU extends sufficiently far east to cover the Vanuatu subduction zone; however, they do not image any increased velocities corresponding to subducting slabs. The slow anomalies seen in the MORs south of Australia cease to be continuous in this depth range. In fact, by 200 km, only a narrow sliver of low velocities persists along the northern edge of the spreading center.

By 200 km depth, the fast anomalies beneath central Australia have somewhat shrunk in their eastern reach, and only the central region appears anomalously fast at $\sim$250 km depth. All three regional models find fastest anomalies at 250 km depth to be in north-central Australia, consistent with the location of the fast anomaly present in our model. However, we are unable to resolve fast velocities in the southwestern corner of Australia, which are especially prominent in SAU and FSW, and somewhat weaker in FAU; this may be due to contamination by small-scale variations of radial anisotropy. At 250 km, two fast anomalies appear, one at each end of the Australian-Antarctic discordance, which is a site of unusual topography, unique geochemistry Christie et al. (1998) and anomalous seismic

upper mantle structure (Forsyth et al., 1987; Ritzwoller et al., 2003). While at 250 km, the eastern anomaly appears to be stronger than the western one, the western one becomes dominant by 350 km depth, and both disappear in the transition zone.

The greatest differences among the regional models and the results of our study are apparent at depths below 300 km. Aside from the fast anomalies associated with the Australian-Antarctic discordance, the only prominent fast velocities in our model at these depths are the images of the subducting slabs beneath Java, Banda Sea and Papua New Guinea. Aside from a strong low velocity anomaly beneath the southern tip of the southern island of New Zeland, the map is rather bland. This is broadly consistent with the results of FSW. However, FAU finds that almost the entire region is seismically fast at these depths, and interprets these fast anomalies as the northward extension of North Australian craton! Our model presents no evidence that would warrant such a conclusion.

5.5.5 Eurasia

Eurasia is the site of active continental collision (Tibet and the Mediterranean), active rifting (Lake Baikal), and its southern and eastern margin host significant shallow and deep seismicity. Nevertheless, continent-scale shear wave-speed tomography is made difficult by the fact that most of the continental interior is aseismic, and seismic station coverage is sparse in Russia and the Central Asian republics. However, when a global dataset is used,

surface wave and overtone coverage across Asia is excellent, allowing for higher-resolution parameterization to be used within Asia (as done by Kustowski et al., 2008), or for smaller-scale features to be robustly imaged within a more-densely parameterized global model (as is the case in our study). Furthermore, the last decade saw the development of a number of large-scale regional studies of vertically-polarized shear wave-speed variations (e.g. Lebedev and Nolet, 2003; Friederich, 2003; Priestley et al., 2006; Boschi et al., 2004).

Figure 5.12 shows map views of our model at a variety of depths. The structure of the uppermost mantle at 75 km depth beneath the northern part of the continent shows a large domain of fast velocities stretching from eastern Siberia all the way to the western margin of the East European craton. A band of somewhat slow $\sim$ -2% anomalies that extend from Tibet in the east to the Anatolian Convergence Zone in the west separate the fast velocities in the north from smaller but prominent fast anomalies that can be seen beneath the stable part of Saudi Arabia and India. This structure is clearly seen in the model of Kustowski et al. (2008), and the slow anomalies beneath Anatolia are seen in the model of Boschi et al. (2004). Small amplitude ($\sim$ 2%) fast anomalies are imaged beneath the Tarim and Sichuan basins, bounding the low velocities of Tibet to the north and south, respectively. These small features are also imaged by Priestley et al. (2006) and Friederich (2003). Like Kustowski et al. (2008) and Priestley et al. (2006), we also image a prominent slow anomaly beneath the Altai Mountains of Mongolia at this depth, though this anomaly is not clearly seen in the model of Friederich (2003). Slow velocities are also seen in the mantle wedges of all the subduction zones in the east of the continent.

At a depth of 150 km, Tibet is seen to be underlain by very fast velocities, which is consistent with all the aforementioned studies. Anomalously fast mantle is once again imaged beneath the Tarim and Sichuan basins, India, and Arabia. In the north, the fast anomalies are clearly strongest beneath the East European and Siberian cratons, and are separated by a band of somewhat less fast velocities. This clear separation of the two largest Asian cratons is not obvious in either the Priestley or Kustowski tomography. The slow velocities that are present beneath the Altai Mountains have shifted northeastward with depth, so that they are now centered to the east of Lake Baikal. This is seen in Kustowski and Priestley tomography, but is a bit west of the structure imaged by Friederich, who found slowest velocities at this depth to be precisely beneath Lake Baikal. In the west, a notable, fast anomaly appears to be associated with the Hellenic Arc, consistent with the results of Boschi et al. (2004).

By 250 km depth, we see a weakening of seismic signature beneath all the cratons, with the substantial fast anomalies only persisting beneath the East European Craton. Nevertheless, smaller-amplitude fast anomalies are still seen beneath the Siberian and Arabian cratons, though their shape is considerably altered: fragmented beneath Siberia and elongated in the north-south direction under Arabia. Remarkably, the remaining small-scale fast anomalies beneath Siberia are found at identical locations by Priestley et al. (2006). Fast velocities are also seen beneath Tibet, in agreement with all the regional studies. Finally, the low velocities to the west of Lake Baikal persist at this depth.

The pattern of seismic anomalies changes drastically by 350 km depth. No signature of fast cratonic keels is seen at this depth, and the most prominent structure is a broad zone of fast velocities extending from the Himalayan front northward into central Siberia. Unlike Kustowski et al. (2008), we do not image slow velocities in beneath Tibet at this depth. Furthermore, unlike Friederich (2003), who trace anomalously low velocities beneath Lake Baikal into the transition zone, we cease to resolve a clear low velocity zone associated with the Baikal by 350 km depth.

Within the transition zone, we image a band of fast velocities stretching from Italy into Iran, which was seen by Kustowski et al. (2008), and interpreted to be associated with cold, subducted material, which also elevated the 400 km discontinuity. In the east, fast velocities are seen along the entire continental margin, which is probably a signature of subduction of oceanic lithosphere. These fast velocity anomalies persist to the base of the transition. In this depth range, low velocities appear to underly most of central and western Russia, as well as southern India and Arabia. This is broadly consistent with the transition zone images of Kustowski and Friederich, though significant differences in details can be seen.

5.6 A regionalized model

A number of regionalized models have been developed over the years (Jordan, 1981; Nataf and Ricard, 1996; Gudmundsson and Sambridge, 1998) which divide the surface into provinces based on surface tectonics: whether they are part of the continent or ocean, their age, and their level of volcanic and seismic activity. Because seismic structure was found to correlate with surface expressions of tectonics (e.g. review by Romanowicz, 1991), the seismic structure of the upper mantle could be inferred from geological and geophysical observations made at the surface (e.g. Nataf and Ricard, 1996; Gudmundsson and Sambridge, 1998). Part of the motivation for this work was that global tomographic models of upper mantle velocity available ten years ago did not have amplitudes large enough to be consistent with variations seen from local and regional studies (see Gudmundsson and Sambridge, 1998). Thus, observations from the surface would be related to regional and local studies of seismic structure and then extrapolated across the globe. Ricard et al., 1996 found that the 3SMAC upper mantle model was able to provide a good fit to observed Love and Rayleigh phase velocities.

Here, we turn this reasoning on its head, and ask the question: Is our global tomographic model sufficiently accurate to take advantage of correlations between tectonics and seismic structure in order to improve our knowledge of tectonics. Indeed, surface observations of tectonics are themselves associated with inaccuracies. For example, inferences on the location of cratons might be biased by surface observations if portions of the crys-

talline basement is obscured by younger sediments. Similarly, creating a regionalized seismic model from expressions of surface tectonics involves an extrapolation step in which structures at the surface are interpreted as vertical extensions of deeper structure (and vice versa); however, the actual architecture of a continental platform, for instance, might involve non-vertical structures. By developing a tectonic regionalization based on a global seismic tomographic model, we might be able to better understand tectonic processes by which continents are put together and their relationship to surface geology, seismicity and volcanism.

In order to do this, we begin by extracting the absolute isotropic shear velocity profile below each point on the surface, sampled every 25 km in depth and 2 degrees laterally. Because the uppermost 300 km is the site of largest seismic anomalies as well as most strongly correlated with surface tectonics, we restrict the depth range of the velocity profiles to be 50-300 km. Then, we calculate the euclidean distance between each pair of profiles. Similar profiles are merged into clusters, and the distance between two clusters is taken to be the greatest of all the pairwise distances between profiles within the clusters. The maximum differences within a cluster are smaller than those between clusters. This is continued until a desired number of clusters is obtained. We then map the locations of each cluster of profiles on the surface, and compare our seismic regionalizations to surface tectonics.

We start by allowing only two clusters (see top panel of Figure 5.13), which should allow

us to identify which areas are the most different from a seismological viewpoint. What we obtain is one cluster that covers $\sim$ 75% of the surface including all of the oceans as well as what Jordan (1981) might term the "tectonic" continent, in which significant deformation, seismicity and volcanism are present, such as northeastern Africa, the southern Europe, the western portion of North America, or much of the areas underlying China and the vicinity of the Baikal Rift. The average velocity profile within this cluster shows a pronounced low velocity zone, with a velocity minimum of 4.35 km/s reached at a depth of 110 km. The other cluster covers stable continental platforms, as well as the very oldest ocean in the northwestern Pacific. Remarkably, it is characterized by two minima, one at 100-150 km depth and another at $\sim$250 km depth.

Allowing for an additional cluster (second row of Figure 5.13) separates the continental collision associated with Tibet from the rest of the continental profiles. The distinguishing features of Tibet when compared to other continental regions are its thick crust, the slow velocities seen beneath it down to $\sim$150 km depth, and high velocities between 150 and 250 km depth. These features can be seen in velocity profiles shown in Figure 5.13. The addition of a fourth cluster separates the oceans into a young region associated with spreading centers, and an older region further away from them. The difference in seismic velocity profiles that distinguishes these two regions is the depth and minimum velocity associated with the low velocity zone; younger oceanic lithosphere is underlain by asthenosphere that has a minimum velocity of 4.25 km/s at 100 km, while the asthenosphere beneath older oceanic lithosphere has minimum velocities of 4.4 km/s, which is reached in the 100-125

km depth range.

This means that the difference between stable and tectonic active continental regions is the strongest as far as mantle seismic structure is concerned, followed by the difference between mantle underlying old and young oceanic lithosphere. Cratons are distinguished from surrounding stable continental structures only by allowing the creation of a fifth cluster. Finally, by allowing for a 6th cluster, we distinguish areas of anomalously low velocities beneath 150 km, which is the first cluster that is not related to surface tectonics in a straightforward way.

We find that a regionalization based on 6 clusters is informative without being too cluttered. In this regionalization, which is shown in Figure 5.14, we identify all the world's major cratonic areas, including smaller ones such as the Arabian, Sao Fernando and the Indian cratons. These all belong to a single cluster (or region), which we denote CR1 and shown in green in Figure 5.14. CR1 is characterized by the fast upper mantle seismic velocities of $\sim$4.7 km/s and is anomalously fast down to a depth of $\sim$ 250 km (see Figure 5.15). This region is surrounded by a second region (CR2), which appears to comprise other stable regions with similar, but $\sim$ 100 m/s slower velocity profiles. CR2, which is shown in cyan in Figure 5.14, also includes the very oldest oceanic crust. Though CR2 also has fast velocities extending to $\sim$200 km, no large negative gradient bounds it at the bottom, which is why our gradient-based approach to determining the depth to the LAB did not find CR2 to be associated with great lithospheric thicknesses. Both of these clusters have local

velocity minima around a depth of 100-120 km, with small negative velocity gradients with depth that peak at ∼100 km. These might be associated with the transition from chemical- to thermal lithosphere (Lee et al., 2005), and might explain the observations of Rychert and Shearer (2009) as proposed by Romanowicz (2009).

Three of the clusters are clearly associated with oceanic crust, though they are, on occasion, found beneath continents. The slowest of these (OR1), shown in purple in Figure 5.14, is found beneath the world's MORs as well as the back-arcs of subduction zones. Beneath continents, it is found in the Red Sea and the Ethiopian segment of the East African Rift, the Cameroon Volcanic Line, the Anatolian Convergence Zone, to the southwest of the Baikal Rift, western North America. The velocity profile beneath this region features a very prominent low velocity zone a very similar shape to that found beneath the slowest regions, but is ∼75 m/s on average faster at all depths. It features a prominent low velocity zone with a minimum velocity of ∼4.25 km/s found at a depth of 100 km.

At the margins of the areas covered by this cluster, we find an interesting region (OR2), shown in red in Figure 5.14. This region can be seen beneath the Arctic, beneath the Coral and Tasman Seas, in a narrow region of central South America, west of the Baikal Rift, as well as in northwest-southeast trending bands across the Indian and Pacific basins, one of which passes in the vicinity of Hawai'i, and another one near the Samoan and Tahiti hotspots. This region is characterized by higher velocities in the upper 100 km than seen in OR, but velocities below 150 km that are ∼50 m/s slower than those belonging to OR1.

A somewhat less-well pronounced low velocity zone appears to be associated with OR2, and the slowest velocities of $\sim$4.35 km/s occur at 125 km, which is somewhat deeper than in OR1. Thus, OR2 appears to be distinguished from OR1 by a faster asthenosphere and anomalously low velocities at depth.

Though seen along the margins of CR2, the final oceanic region (OR3), can be most strongly associated with old oceanic crust, and is shown in dark blue in Figure 5.14. Its velocity profile falls near the middle between the cratonic profile of CR1 and the slow velocities associated with OR1. It shows a weak low velocity zone, in which minimum velocities of $\sim$4.43 km/s are observed between 90-125 km depth.

We wish to stress that a clustering based solely on similarities in profiles of absolute shear wave-speed does a remarkable job of identifying Earth's tectonic provinces. This is not simply a different way of looking at the known correlations between upper mantle seismic structure and surface tectonics. Instead, it demonstrates that seismic structure within a tectonic setting is more similar to other structures in a similar tectonic setting - whether they are geographically close or on a different continent - than it is to much less distant locations that happen to belong to a different tectonic setting. Finally, this preliminary work paves the way for interpreting the regional profiles in terms of thermal profiles and chemical heterogeneity.

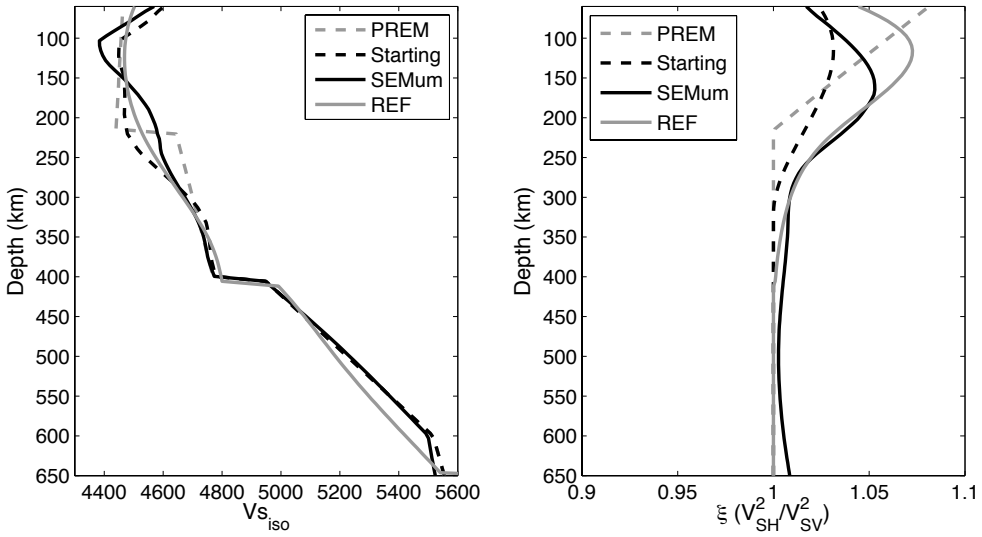

Figure 5.1: (left) Profiles of isotropic shear wave-speed in our starting model, in SEMum, PREM and REF. (right) Profiles of ξ.

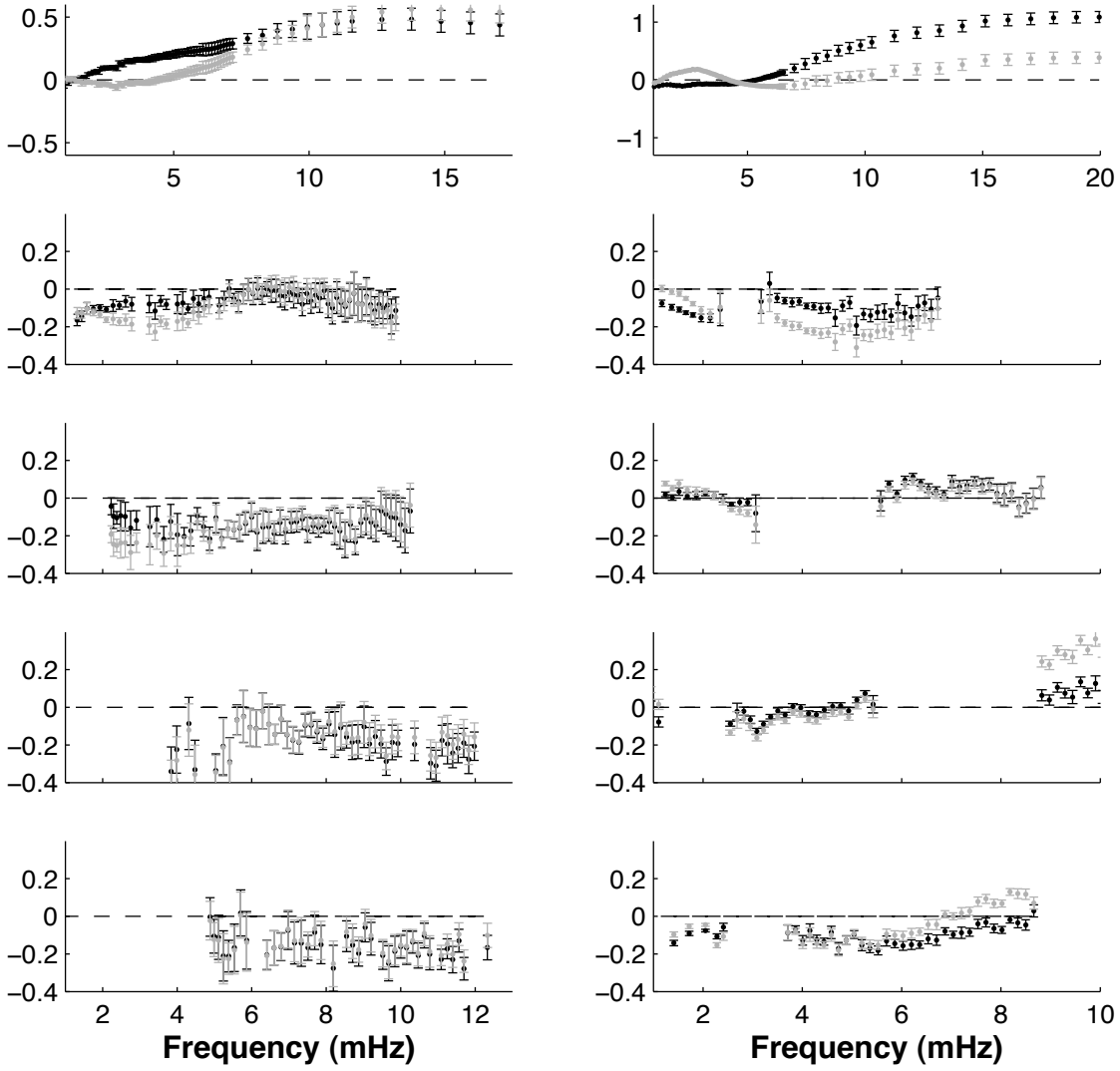

Figure 5.2: Predictions of toroidal (left column) and spheroidal (right column) eigenfrequencies of free oscillation for the fundamental branch (top), and first through fourth overtones. The y-axis denotes percent difference between observed frequencies and predictions of PREM (black) and SEMum1D (gray).

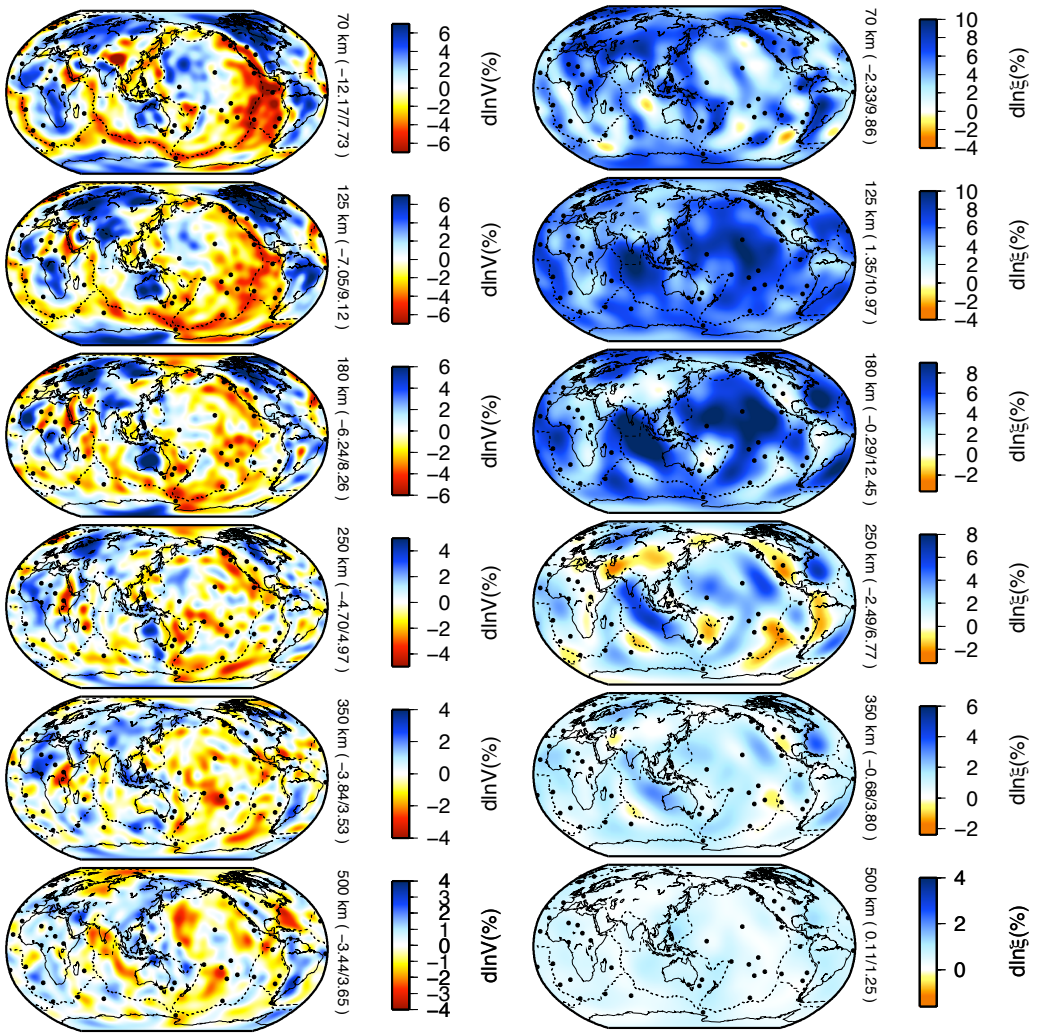

Figure 5.3: (left) Maps of the Voigt average shear wave-speed variations with respect to the average velocity at each depth. Note that the limits of color scales change with depth and that the colors saturate in certain regions. (right) Maps of radial anisotropy parameter ξ, showing regions in which horizontally polarized waves are faster (blue) and slower (orange) than vertically polarized wavs. Note the asymmetry of the colorscale. Black circles indicate locations of hotspots from Steinberger, 2000.

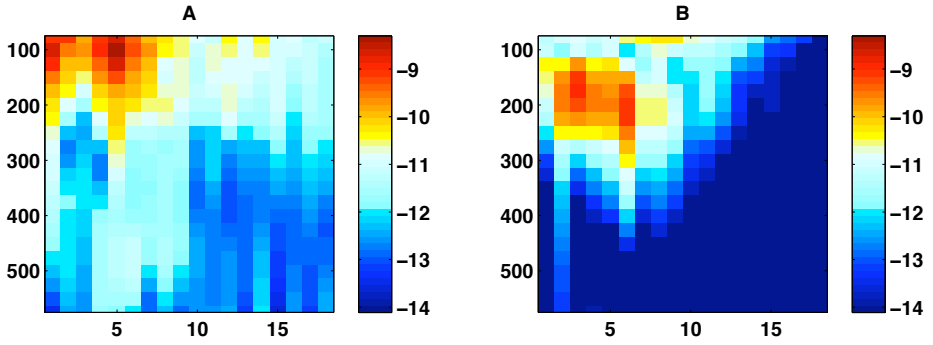

Figure 5.4: Power of the V_{Siso} (left) and ξ (right) model as a function of depth and angular degree (wavenumber). The colorscale is logarithmic.

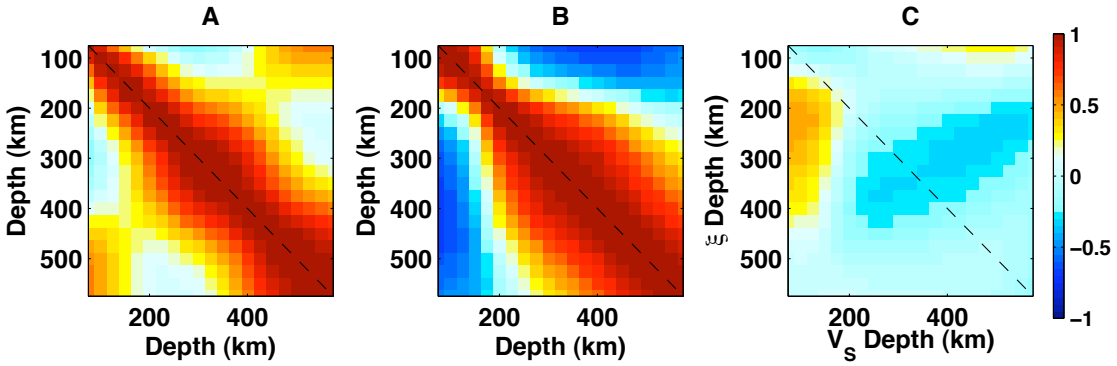

Figure 5.5: A. Radial correlation function of the V_{Siso} anomalies. B. Radial correlation function for ξ anomalies. C. Cross-correlation between the variations of V_{Siso} and ξ.

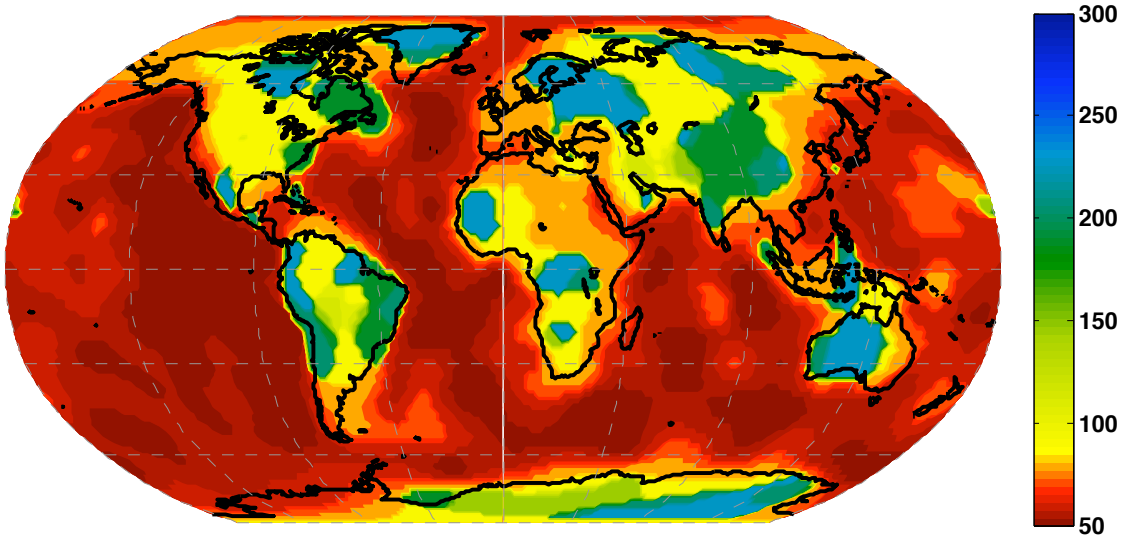

Figure 5.6: Map of lithospheric thickness developed by associating the LAB with the maximum negative gradient of velocity with depth. Note that all major cratons are identified with $\sim$230 km thick lithosphere.

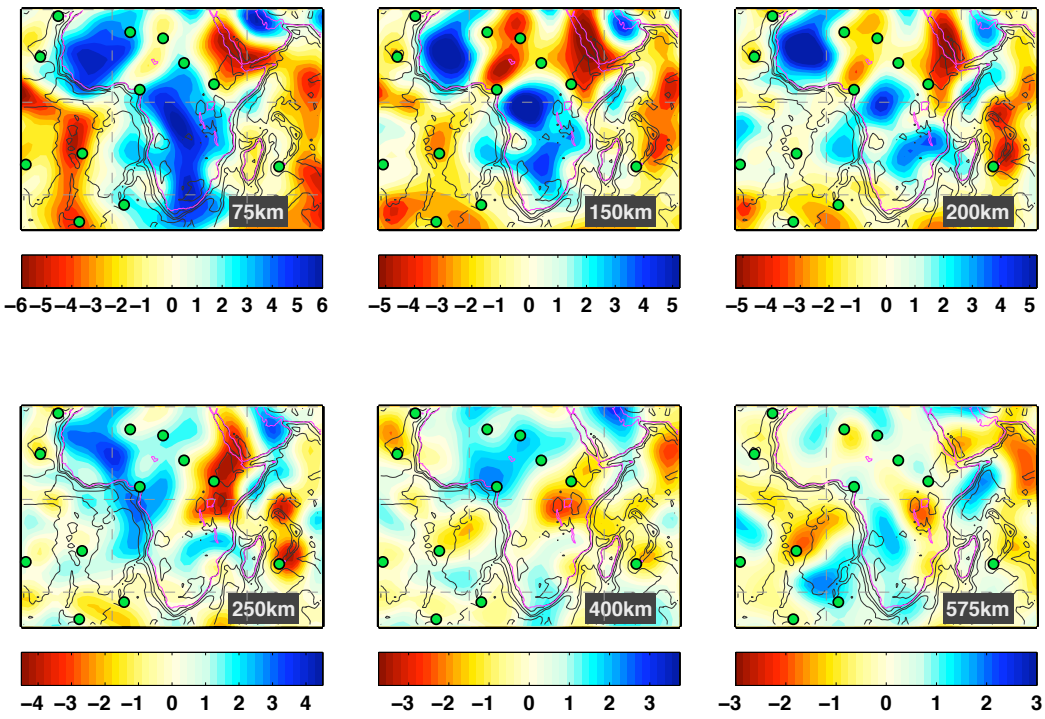

Figure 5.7: (left) Maps of the Voigt average shear wave-speed variations in Africa and surrounding oceans with respect to the average velocity at each depth. Note that the limits of color scales change with depth and that the colors saturate in certain regions.

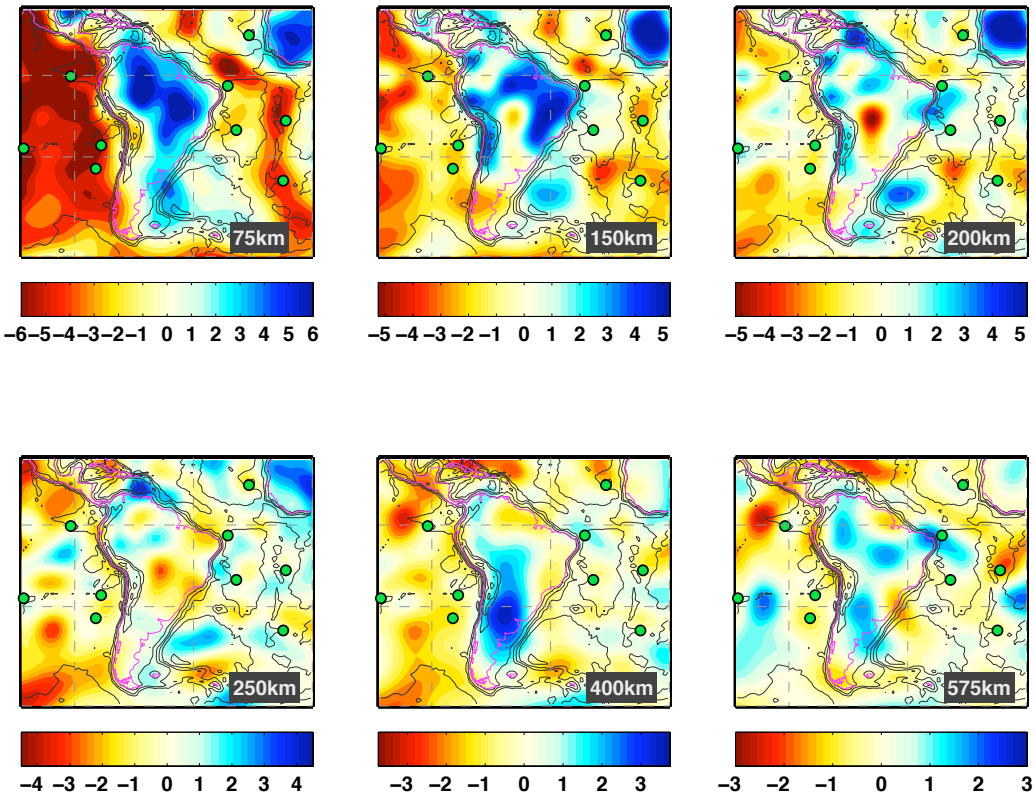

Figure 5.8: Maps of the Voigt average shear wave-speed variations in South America and surrounding oceans with respect to the average velocity at each depth. Note that the limits of color scales change with depth and that the colors saturate in certain regions. Green circles indicate locations of hotspots from Steinberger, 2000

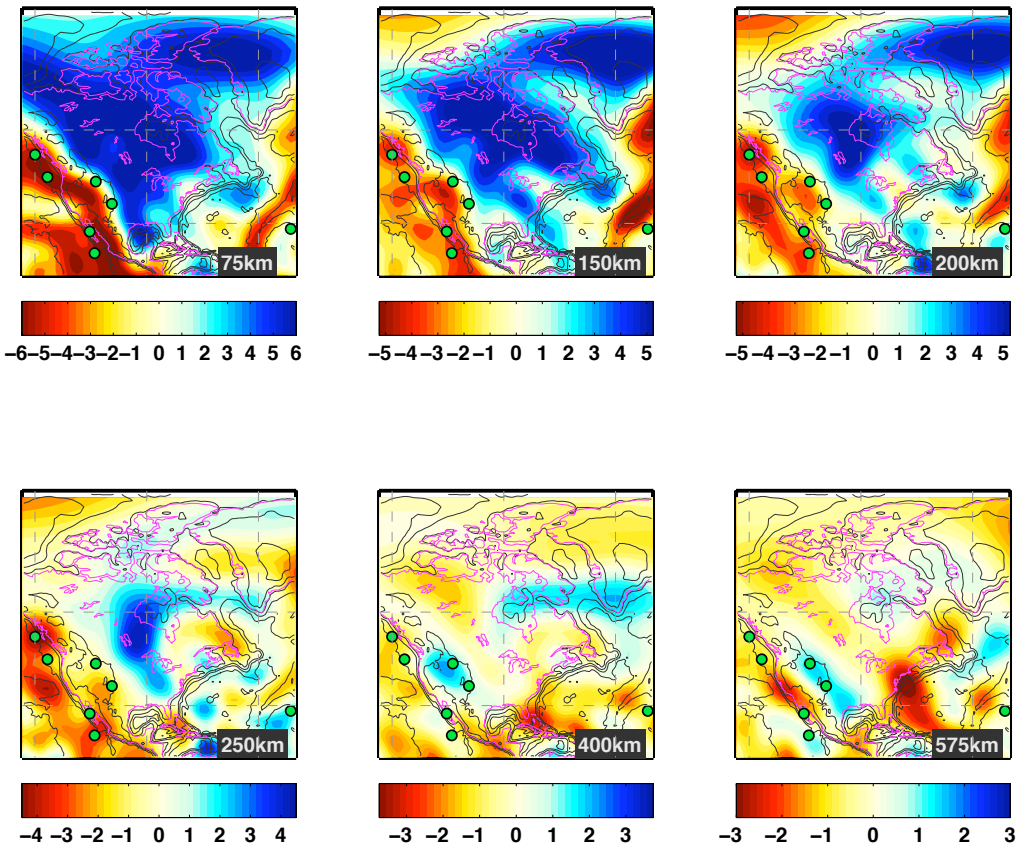

Figure 5.9: Maps of the Voigt average shear wave-speed variations in North America and surrounding oceans with respect to the average velocity at each depth. Note that the limits of color scales change with depth and that the colors saturate in certain regions. Green circles indicate locations of hotspots from Steinberger, 2000

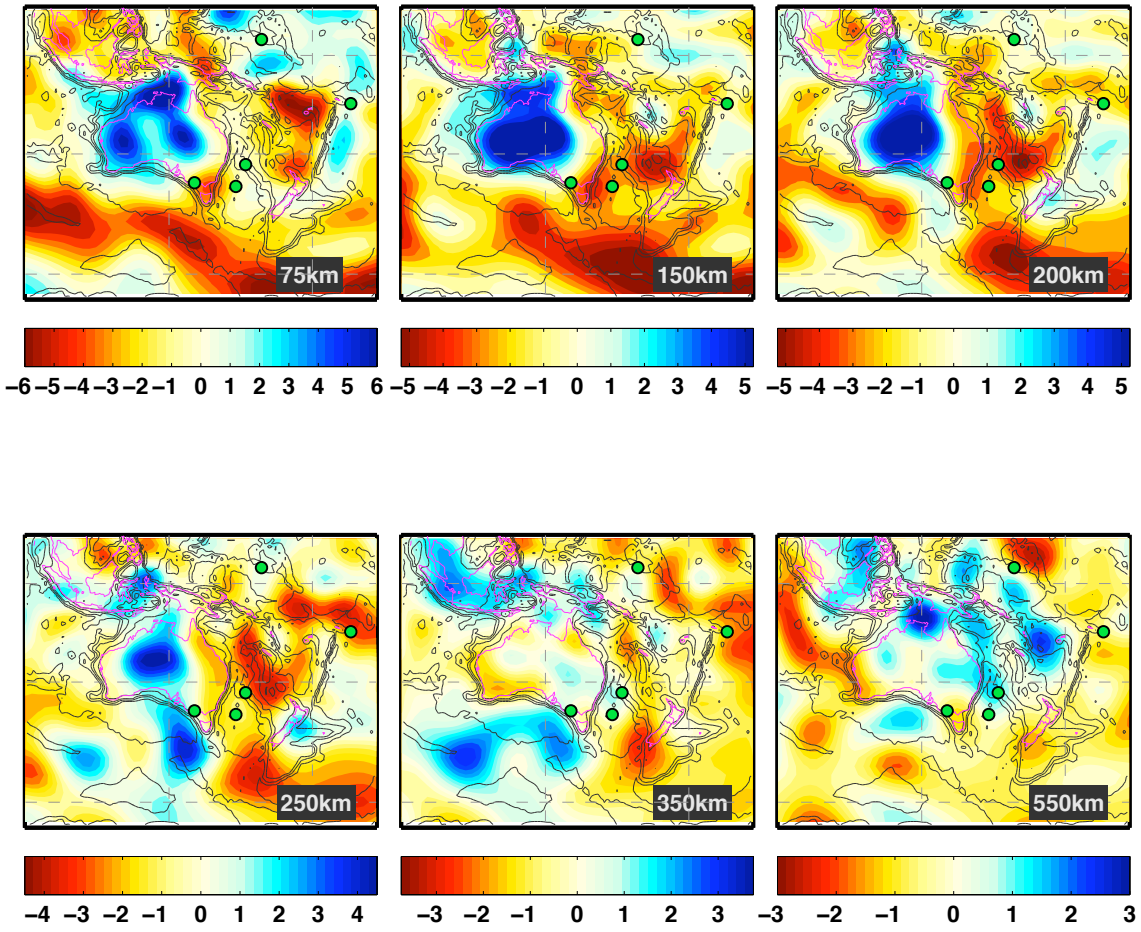

Figure 5.10: Maps of the Voigt average shear wave-speed variations in Australia and surrounding oceans with respect to the average velocity at each depth. Note that the limits of color scales change with depth and that the colors saturate in certain regions. Green circles indicate locations of hotspots from Steinberger, 2000

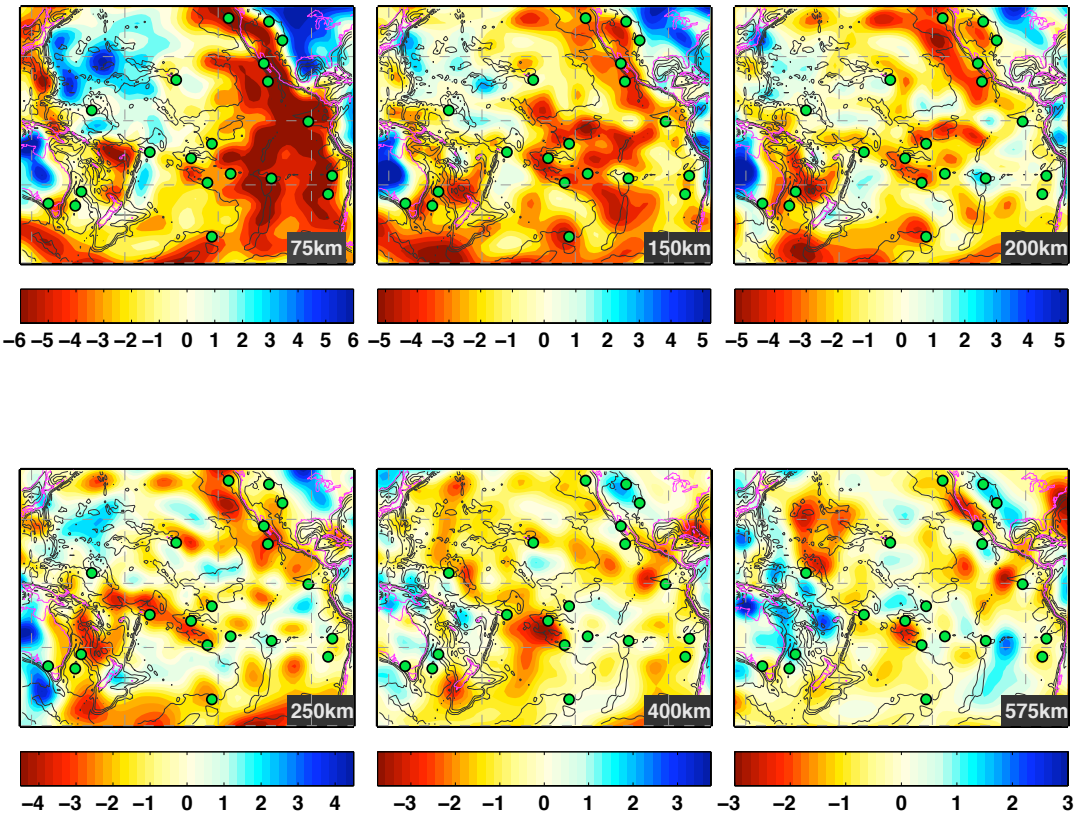

Figure 5.11: Maps of the Voigt average shear wave-speed variations in the Pacific basin with respect to the average velocity at each depth. Note that the limits of color scales change with depth and that the colors saturate in certain regions. Green circles indicate locations of hotspots from Steinberger, 2000

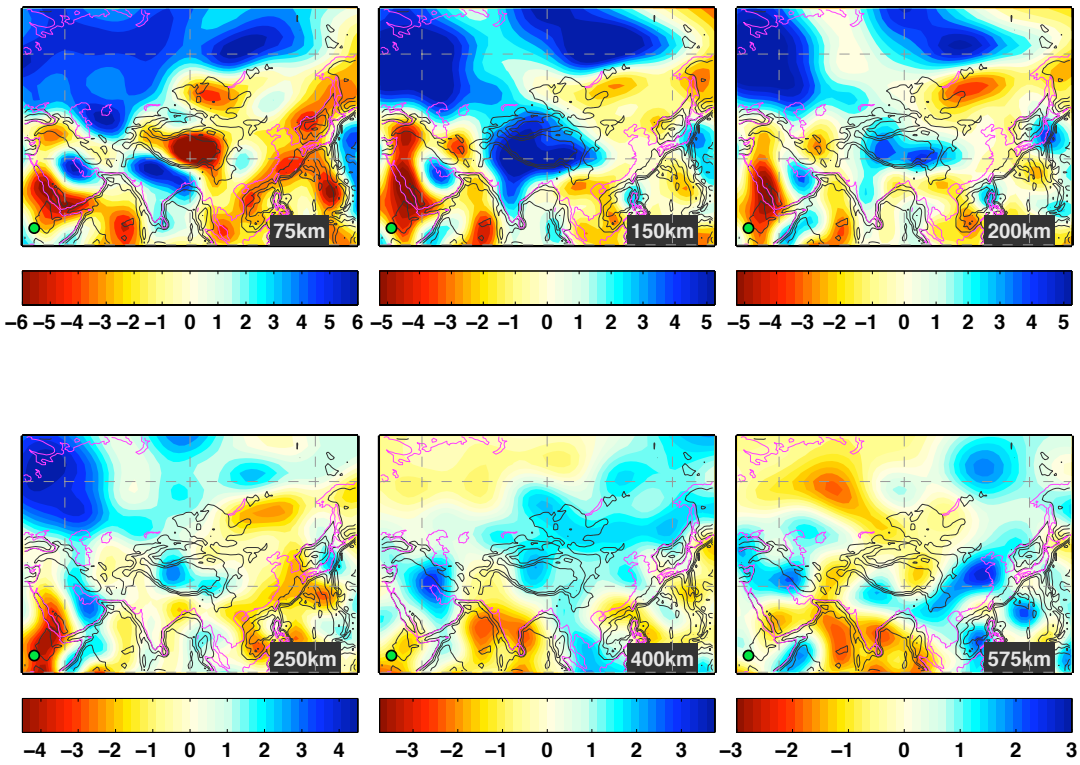

Figure 5.12: Maps of the Voigt average shear wave-speed variations in Asia and surrounding oceans with respect to the average velocity at each depth. Note that the limits of color scales change with depth and that the colors saturate in certain regions. Green circles indicate locations of hotspots from Steinberger, 2000.

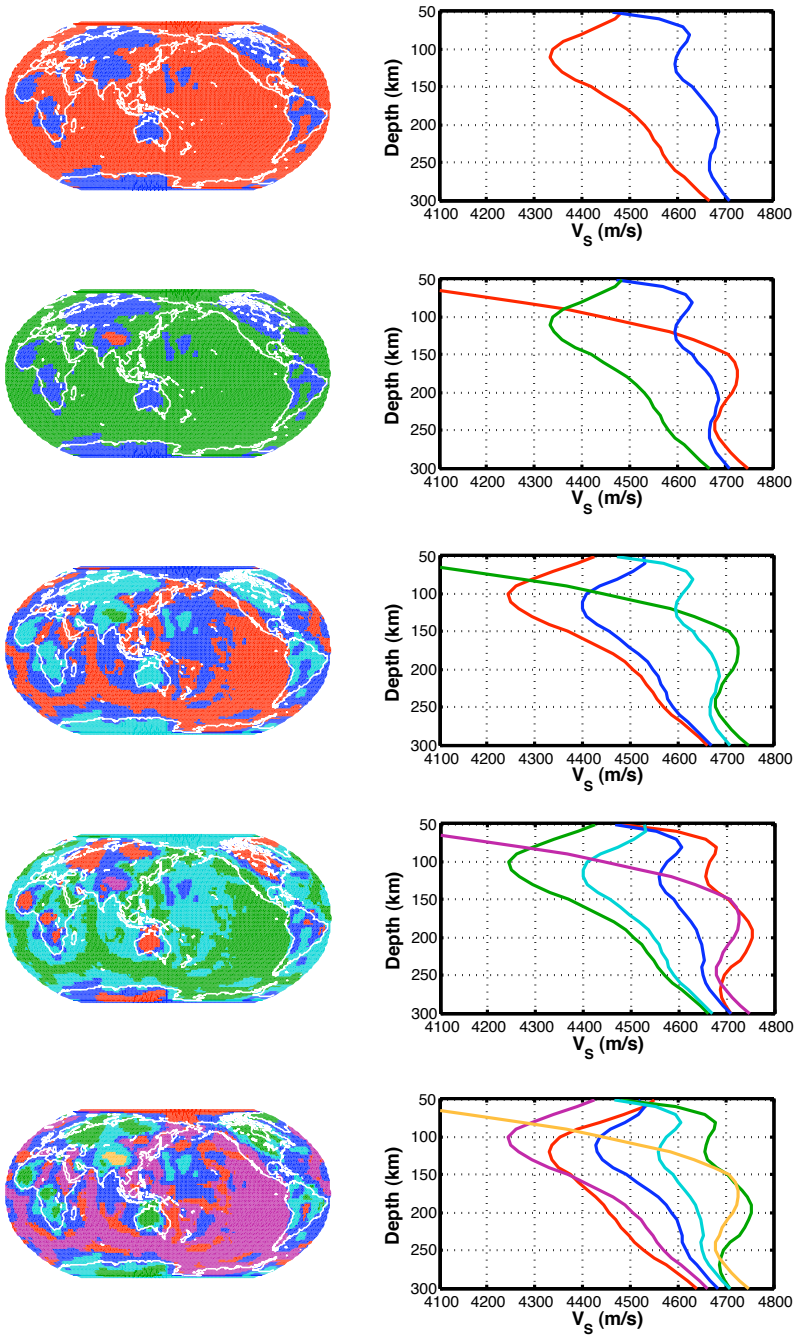

Figure 5.13: (left) Maps showing the changes in the surface extent of regions as more clusters are allowed to form. The number of clusters increases from 2 to 6 going from top to bottom. (right) The profiles of isotropic shear wave-speed associated with each region shown on the left.

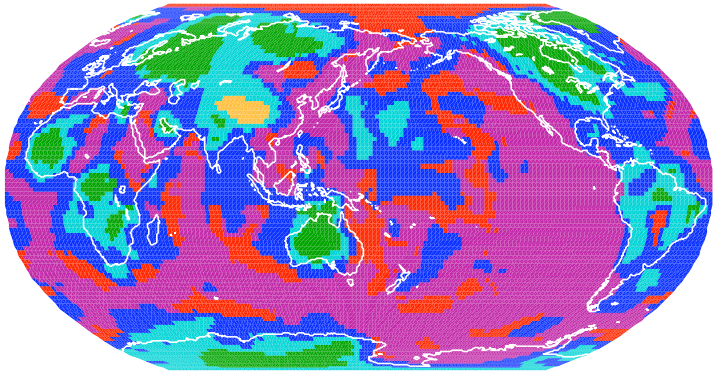

Figure 5.14: Maps showing the surface extent of the 6 regions we have divided the upper mantle into based on similarity between profiles of isotropic wave-speed. The colors correspond to the lines shown in Figure 5.15.

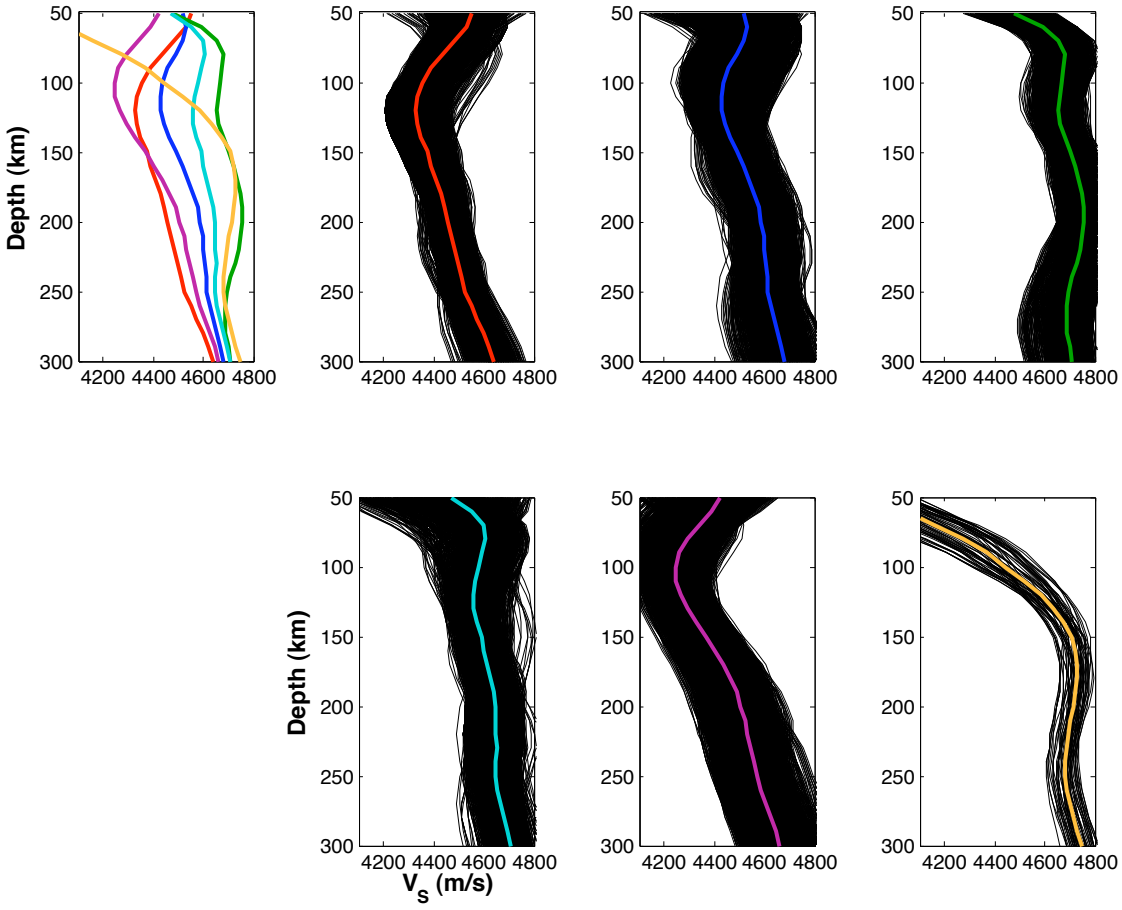

Figure 5.15: Absolute isotropic shear wave-speeds of model SEMum plotted against depth on the y-axis. The colored lines indicate the harmonic mean of the velocity profiles within each of the 6 clusters shown in Figure 5.14. The black lines indicate all the velocity profiles within a given cluster, whose harmonic mean is the representative (colored) profile for that cluster.

Chapter 6

Conclusion and Perspectives

6.1 Upper mantle elastic structure

In Chapters 4 and 5, we developed and applied a new hybrid method of tomography, which allowed us to leverage accurate, fully-numerical wave propagation modeling techniques in order to image the anisotropic structure of the Earth's mantle. This new method reduces the contamination of mantle structure that besets widely used approximate methods, especially due to inaccurate treatment of crustal effects, as discussed in Chapter 3. Our tomographic model is by no means an end in and of itself. Instead, its creation is important for three distinct reasons:

1. We have validated a new way of tomographically mapping the Earth's interior, which

can be applied to a bigger and higher-frequency dataset in order to not only better image the upper mantle, but also gain new insights into the structure of the lower mantle and make more robust regional and small-scale models of elastic structure.

2. For the first time, we have demonstrated that the long-wavelength mantle structure imaged using approximate semi-analytic techniques is robust and representative of the Earth's true structure.

3. We have imaged structures in the upper mantle that were not clearly seen in previous global tomographic models, providing new constraints on the temperature, composition as well as flow in the mantle. Furthermore, by applying clustering analysis to the absolute shear wave-speed profiles, we have created a new way of exploring the relationship between surface expressions of tectonics and their elastic signature in the upper mantle.

One of the main goals of seismic tomography is to image the interior structure of the Earth so as to improve our knowledge of Earth's temperature, composition, and dynamics. Variations of shear wave-speed that we have mapped within the upper mantle arise from variations in composition and temperature. Constraints from mineral physics can inform interpretations of observed velocities in terms of temperature and abundances of major mantle mineral phases. The average profile of shear wave-speed of SEMum is characterized by a more prominent low velocity zone which is bounded by steeper velocity gradients with depth than those present in other 1D models of the Earth (e.g. Dziewonski and Anderson,

1981; Montagner and Kennett, 1996; Kustowski et al., 2008). Understanding the implications of this structure requires analyses similar to those used by several recent studies to interpret Earth's average 1D shear wave-speed structure in terms of chemistry and composition (Cammarano et al., 2005; Cammarano and Romanowicz, 2007; Cammarano et al., 2009; Xu et al., 2008; Ritsema et al., 2009).

By applying an agglomerative clustering technique to the profiles of absolute shear wave-speed beneath a grid of points on the surface of the Earth, we have been able to explore the similarities of seismic structure in the upper mantle. We found that defining the distance between clusters to be the maximum Euclidean distance between their constituent profiles results in clusters that bear close resemblance to surface expressions of tectonics. Creating 4 clusters enabled us to differentiate among regions of old and young oceanic lithosphere as well as tectonically stable and active continents. Additional clusters distinguished stable younger continental regions from older Proterozoic/Archean cratons, and identified regions of anomalously low velocities at depths greater than 150 km, which were predominantly located beneath oceanic lithosphere. The relationship of this last cluster to models of plume flux (e.g. Sleep, 1989) and residual basement depth (e.g. Muller et al., 2008) should be analyzed in order to elucidate the character of this region, which is not clearly related to surface expressions of tectonics. Furthermore, by extracting the average seismic profile of each cluster, we constructed velocity profiles that were representative of each tectonic region. The thermochemical character of each of these profiles can be analyzed using the same mineral-physics techniques that are applied to the analysis of the average velocity

structure of the Earth.

The Earth's geoid and dynamic topography provide constraints on the density anomalies and flow within the Earth (e.g. Hager, 1984; Forte et al., 1993), which are, in turn, related to tomographic models of shear wave-speed through a non-linear relationship between velocity and density perturbations. This is what motivated Simmons et al. (2006) to attempt to improve constraints on mantle structure by supplementing seismic data with models of dynamic topography and free-air gravity. However, the problem of such an approach is that poorly-constrained density-to-velocity scalings need to be determined; Simmons et al. (2006) invert for scaling coefficients that vary only with radius. indeed, as velocity anomalies can be due to both temperature and compositional variations, it is likely that multiple density-to-velocity scaling factors are relevant at any location in the mantle.

More direct constraints on flow in the mantle can be provided by anisotropic structure. Becker et al. (2007) demonstrated that a synthetic model of 3D variations of ξ expected for A-type olivine fabric formation in an upper mantle flow field driven by plate motions and density anomalies scaled from a tomographic V_S model can reproduce some of the major features of observed anisotropic structure. This indicates that though variations of ξ result from a time-integrated history of deformation (see, e.g. Ribe, 1992), the dominant signal may nonetheless arise due to deformation in Mesozoic/Cenozoic flow. By comparing the variations of ξ against global models of free-air gravity and dynamic topography, especially at intermediate lengthscales that are sensitive to upper mantle density / flow variations, we

can leverage SEMum to better map mantle flow.

6.2 Upper mantle anelastic structure

Mapping 3D variations of seismic attenuation within the mantle is important for discriminating between chemical and thermal heterogeneity as well as interpreting models of elastic structure derived from data at different frequencies. While mapping of 3D elastic structure of the upper mantle has benefited from approximate first-order perturbation techniques, modeling of the 3D distribution of seismic attenuation has lagged behind due to difficulties in accounting for purely elastic effects of scattering at sharp interfaces and (de)focusing, which can obscure the anelastic signal. SEMum allows us to more accurately model this elastic effects in two ways:

1. It provides improved phase alignment that is crucial for extracting the signal of attenuation, which is predominantly contained in waveform amplitudes;

2. By imaging sharper and stronger variations of shear wave-speed, SEMum more accurately predicts purely elastic effects on waveform amplitudes, allowing for purely elastic effects to be disentangled from the signal due to attenuation.

The most recent upper mantle Q model from the Berkeley group, QRLW8 (Gung and Romanowicz, 2004), was derived from long period seismograms in the time domain, com-

prising both fundamental mode surface waves and overtones. It was developed using an iterative waveform inversion technique, in which elastic and anelastic structure is solved for in successive steps. Until now, the theoretical framework for both the forward and inverse parts of our inversions has been the non-linear asymptotic mode coupling theory with focusing (Romanowicz, 1987; Li and Romanowicz, 1995), which limits our ability to retrieve 3D Q structure at wavelengths shorter than degree 8 in a spherical harmonics expansion of the model. In order to make further progress, it is therefore necessary to not only obtain better constraints on lateral gradients of elastic structure - which SEMum provides - but also to utilize a more accurate forward modeling theory.

The hybrid tomographic technique developed in Chapter 4 provides a solution to this challenge. Using SEM to forward model wave propagation through the Earth will allow us to account accurately, for the first time, for the effects of scattering and (de)focusing. Therefore, we intend to apply the same hybrid method to the creation of a new model of upper mantle attenuation.

Bibliography

Amante, C., Eakins, B. W., Aug. 2008. Etopo1 1 arc-minute global relief model: Procedures, data sources and analysis. National Geophysical Data Center, NESDIS, NOAA, U.S. Department of Commerce, Boulder, CO.

Anderson, D., 1961. Elastic wave propagation in layered anisotropic media. J. geophys. Res 66 (9), 2953–2963.

Anderson, D., 1976. The earth as a seismic absorption band. Science 196, 1104–1106.

Anderson, D., Given, J., 1982. Absorption band q model for the earth. J. Geophys. Res. 87, 3893–3904.

Anderson, D., Hart, R., 1978. Q of the earth. J. Geophys. Res. 83, 5869–5882.

Anderson, D., Minster, J., 1979. The frequency dependence of q in the earth and implications for mantle rheology and chandler wobble. Geophys. J. R. Astr. Soc. 58, 431–440.

Artemieva, I., 2006. Global $1\times$ 1 thermal model TC1 for the continental lithosphere: implications for lithosphere secular evolution. Tectonophysics 416 (1-4), 245–277.

Artemieva, I., 2009. The continental lithosphere: Reconciling thermal, seismic, and petrologic data. Lithos 109 (1-2), 23–46.

Backus, G., 1962. Long-wave elastic anisotropy produced by horizontal layering. Journal of Geophysical Research 67, 4427–4440.

Backus, G. E., Gilbert, J. F., 1970. Uniqueness in the inversion of inaccurate gross earth data. Phil. Trans. R. Soc. London 266, 123–192.

Bassin, C., G. L., Masters, G., 2000. The current limits of resolution for surface wave tomography in north america. EOS Trans. AGU 81.

Becker, T., Boschi, L., 2002. A comparison of tomographic and geodynamic mantle models. Geochem. Geophys. Geosyst 3 (1), 1003.

Becker, T., Kustowski, B., Ekstrom, G., 2007. Radial seismic anisotropy as a constraint for upper mantle rheology. Earth and Planetary Science Letters.

Bedle, H., van der Lee, S., 2009. S velocity variations beneath North America. Journal of Geophysical Research-Solid Earth 114 (B7), B07308.

Boschi, L., Ekström, G., 2002. New images of the earth's upper mantle from measurements of surface wave phase velocity anomalies. J. Geophys. Res. 107.

Boschi, L., Ekstrom, G., Kustowski, B., 2004. Multiple resolution surface wave tomography: the Mediterranean basin. Geophysical Journal International 157 (1), 293–304.

Bozdağ, E., Trampert, J., Mar. 2008. On crustal corrections in surface wave tomography. Geophys. J. Int. 172, 1066–1082.

Cammarano, F., Deuss, A., Goes, S., Giardini, D., Jan. 2005. One-dimensional physical reference models for the upper mantle and transition zone: Combining seismic and mineral physics constraints. J. Geophys. Res. 110 (B01306).

Cammarano, F., Romanowicz, B., 2007. Insights into the nature of the transition zone from physically constrained inversion of long-period seismic data. Proceedings of the National Academy of Sciences 104 (22), 9139.

Cammarano, F., Romanowicz, B., Stixrude, L., Lithgow-Bertelloni, C., Xu, W., 2009. Inferring the thermochemical structure of the upper mantle from seismic data. Geophysical Journal International 179 (2), 1169–1185.

Capdeville, Y., Chaljub, E., Vilotte, J. P., Montagner, J. P., Jan. 2003. Coupling the spectral element method with a modal solution for elastic wave propagation in global earth models. Geophys. J. Int. 152, 34–67.

Capdeville, Y., Marigo, J., 2007. Second order homogenization of the elastic wave equation for non-periodic layered media. Geophysical Journal International 170 (2), 823–838.

Cheng, H.-X., Kennett, B., 2002. Frequency dependence of seismic wave attenuation in the upper mantle beneath the australian region. Geophys. J. Int. 150, 45–57.

Chevrot, S., Zhao, L., Apr. 2007. Multiscale finite-frequency rayleigh wave tomography of the kaapvaal craton. Geophys. J. Int. 169, 201–215.

Chiao, L., Kuo, B., 2001. Multiscale seismic tomography. Geophysical Journal International 145 (2), 517–527.

Christie, D. M., West, B. P., Pyle, D. G., B., H. B., 1998. Chaotic topography, mantle flow and mantle migration in the Australian-Antarctic discordance. Nature 394, 637–644.

Conrad, C., Lithgow-Bertelloni, C., 2006. Influence of continental roots and asthenosphere on plate-mantle coupling. Geophys. Res. Lett 33 (5).

Dahlen, F., Hung, S., Nolet, G., 2000. Fréchet kernels for finite-frequency traveltimes-I. Theory. Geophysical Journal International 141 (1), 157–174.

Dahlen, F., Tromp, J., 1998. Theoretical Global Seismology. University Press, Princeton.

Dalton, C., Ekstrom, G., 2006. Constraints on global maps of phase velocity from surface-wave amplitudes. Geophysical Journal International 167 (2), 820–826.

Dalton, C. A., Ekström, G., 2006. Global models of surface wave attenuation. J. Geophys. Res. 111, B05317,doi: 10.1029/2005JB003997.

Durek, J., Ekström, G., 1996. A radial model of anelasticity consistent with long-period surface-wave attenuation. Bull. Seism. Soc. Amer. 86, 155–158.

Durek, J. J., Ekström, G., 1997. Investigating discrepancies among measurements of traveling and standing wave attenuation. J. Geophys. Res. 102, 24529–24544.

Dziewonski, A., 2005. The robust aspects of global seismic tomography. Plates, plumes, and paradigms, 147.

Dziewonski, A., Hager, B., O'Connell, R., 1977. Large-scale heterogeneities in the lower mantle. Journal of Geophysical Research 82, 239–255.

Dziewonski, A. M., Anderson, D. L., 1981. Preliminary reference earth model. Phys. Earth Planet. Inter. 25, 297–356.

Ekstrom, G., Dziewonski, A., 1998. The unique anisotropy of the Pacific upper mantle. Nature 394 (6689), 168–172.

Ferreira, A., Woodhouse, J., 2006. Source, path and receiver effects on seismic surface waves. Geophysical Journal International 168 (1), 109.

Fichtner, A., Igel, H., 2008. Efficient numerical surface wave propagation through the optimization of discrete crustal models-a technique based on non-linear dispersion curve matching (DCM). Geophysical Journal International 173 (2), 519–533.

Fichtner, A., Kennett, B., Igel, H., Bunge, H., 2009a. Full seismic waveform tomography for upper-mantle structure in the Australasian region using adjoint methods. Geophysical Journal International, 387.

Fichtner, A., Kennett, B., Igel, H., Bunge, H., 2009b. Full seismic waveform tomography for upper-mantle structure in the Australasian region using adjoint methods. Geophysical Journal International, 387.

Fishwick, S., Kennett, B., Reading, A., 2005. Contrasts in lithospheric structure within the Australian cratonÑinsights from surface wave tomography. Earth and Planetary Science Letters 231 (3-4), 163–176.

Flanagan, M. P., Wiens, D. A., 1998. Attenuation of broadband p and s waves in tonga: Observations of frequency dependent q. Pure Appl. Geophys. 153, 345–375.

Forsyth, D., Ehrenbard, R., Chapin, S., 1987. Anomalous upper mantle beneath the Australian-Antarctic Discordance. Earth and Planetary Science Letters 84, 471–478.

Forte, A., Peltier, W., Dziewonski, A., Woodward, R., 1993. Dynamic surface topography: a new interpretation based upon mantle flow models derived from seismic tomography. Geophysical Research Letters 20 (3), 225–228.

Friederich, W., 2003. The S-velocity structure of the East Asian mantle from inversion of shear and surface waveforms. Geophysical Journal International 153 (1), 88–102.

Godey, S., Deschamps, F., Trampert, J., Snieder, R., 2004. Thermal and compositional anomalies beneath the North American continent. Journal of Geophysical Research-Solid Earth 109.

Grand, S., Helmberger, D., 1984. Upper mantle shear structure of North America. Geophys. J. Int 76, 399–438.

Gu, Y. J., Dziewoński, A. M., Ekström, G., Aug. 2003. Simultaneous inversion for mantle

shear velocity and topography of transition zone discontinuities. Geophys. J. Int. 154, 559–583.

Gudmundsson, O., Sambridge, M., 1998. A regionalized upper mantle (RUM) seismic model. Journal of Geophysical Research 103, 7121–7136.

Gung, Y., Panning, M., Romanowicz, B., et al., 2003. Global anisotropy and the thickness of continents. Nature 422 (6933), 707–711.

Gung, Y., Romanowicz, B., 2004. Q tomography of the upper mantle using three-component long-period waveforms. Geophys. J. Int. 157, 813–830, doi: 10.1111/j.1365–246X.2004.02265.x.

Hager, B., 1984. Subducted slabs and the geoid- Constraints on mantle rheology and flow. Journal of Geophysical Research 89 (B7), 6003–6015.

Hirschmann, M., 2006. Water, melting, and the deep Earth H2O cycle. Ann. Rev. Earth Planet. Sci. 34, 629–653.

Houser, C., Masters, G., Shearer, P., Laske, G., 2008. Shear and compressional velocity models of the mantle from cluster analysis of long-period waveforms. Geophysical Journal International 174 (1), 195–212.

Jackson, D., Anderson, D., 1970. Physical mechanisms of seismic-wave attenuation. Rev. Geophys. 8, 1–63.

Jackson, I., Fitz-Gerald, J., Faul, U. a. B., 2002. Grain-size-sensitive seismic wave attenuation in polycrystalline olivine. J. Geophys. Res. 107, doi: 10.1029/2001JB001225.

Jackson, I., Webb, S., Weston, L., Boness, D., 2005. Frequency dependence of elastic wave speeds at high temperature: a direct experimental demonstration. Phys. Earth Planet. Inter. 148, 85–96.

Jordan, T., 1978. Composition and development of the continental tectosphere. Nature 274 (5671), 544–548.

Jordan, T., 1981. Global tectonic regionalization for seismological data analysis. Bulletin of the Seismological Society of America 71 (4), 1131.

Kanamori, H., Anderson, D., 1977. Importance of physical dispersion in surface wave and free oscillation problems: Review. Rev. Geophys. Space Phys. 15, 105–112.

Karato, S., Jung, H., Katayama, I., Skemer, P., 2008. Geodynamic significance of seismic anisotropy of the upper mantle: new insights from laboratory studies. Annu. Rev. Earth Planet Sci. 36, 59–95.

Karato, S.-I., Spetzler, H., 1990. Defect microdynamics in minerals and solid-state mechanics of seismic wave attenuation and velocity dispersion in the mantle. Rev. Geophys. 28, 399–429.

Katayama, I., Karato, S., 2006. Effect of temperature on the B-to C-type olivine fabric

transition and implication for flow pattern in subduction zones. Physics of the Earth and Planetary Interiors 157 (1-2), 33–45.

Kawakatsu, H., Kumar, P., Takei, Y., Shinohara, M., Kanazawa, T., Araki, E., Suyehiro, K., 2009. Seismic Evidence for Sharp Lithosphere-Asthenosphere Boundaries of Oceanic Plates. Science 324 (5926), 499.

Kennett, B. L. N., Engdahl, E. R., Buland, R., 1995. Constraints on seismic velocities in the earth from traveltimes. Geophysical Journal International 122, 108–124.

Komatitsch, D., Tromp, J., Jul. 2002. Spectral-element simulations of global seismic wave propagation-ii. three-dimensional models, oceans, rotation and self-gravitation. Geophys. J. Int. 150, 303–318.

Komatitsch, D., Vilotte, J., 1998. The spectral element method: an efficient tool to simulate the seismic response of 2D and 3D geological structures. Bulletin of the seismological society of America 88 (2), 368–392.

Kustowski, B., Dziewonski, A., Ekstrom, G., 2007. Nonlinear crustal corrections for normal-mode seismograms. Bulletin of the Seismological Society of America 97 (5), 1756–1762.

Kustowski, B., Ekstrom, G., Dziewonski, A., 2008. The shear-wave velocity structure in the upper mantle beneath Eurasia. Geophysical Journal International 174 (3), 978–992.

Kustowski, B., Ekström, G., Dziewoński, A. M., Jun. 2008. Anisotropic shear-wave velocity structure of the earth's mantle: A global model. J. Geophys. Res. 113 (B12), 6306.

Lebedev, S., Nolet, G., 2003. Upper mantle beneath Southeast Asia from S velocity tomography. Journal of Geophysical Research-Solid Earth 108 (B1), 2048.

Lee, C., Lenardic, A., Cooper, C., Niu, F., Levander, A., 2005. The role of chemical boundary layers in regulating the thickness of continental and oceanic thermal boundary layers. Earth and Planetary Science Letters 230 (3-4), 379–395.

Li, X., Tanimoto, T., Jan. 1993. Waveforms of long-period body waves in a slightly aspherical earth model. Geophys. J. Int. 112, 92–102.

Li, X.-D., Romanowicz, B., Jun. 1995. Comparison of global waveform inversions with and without considering cross-branch modal coupling. Geophys. J. Int. 121, 695–709.

Li, X.-D., Romanowicz, B., Oct. 1996. Global mantle shear velocity model developed using nonlinear asymptotic coupling theory. J. Geophys. Res. 101, 22245–22272.

Liu, H.-P., Anderson, D., Kanamori, H., 1976. Velocity dispersion due to anelasticity; implications for seismology and mantle composition. Geophys. J. R. astr. Soc. 47, 41–58.

Marone, F., Gung, Y., Romanowicz, B., 2007. Three-dimensional radial anisotropic structure of the North American upper mantle from inversion of surface waveform data. Geophysical Journal International 171 (1), 206–222.

Marone, F., Romanowicz, B., Jul. 2007. Non-linear crustal corrections in high-resolution regional waveform seismic tomography. Geophys. J. Int. 170, 460–467.

Marone, F., Romanowicz, B., 2007. The depth distribution of azimuthal anisotropy in the continental upper mantle. Nature 447 (7141), 198–201.

Masters, G., Gilbert, F., 1983. Attenuation in the earth at low frenquencies. Phil. Trans. R. Soc. Lond. 308, 479–522.

Masters, G., Gubbins, D., 2003. On the resolution of density within the earth. Phys. Earth Planet. Inter. 140, 159–167.

Masters, G., Laske, G., 1997. On bias in surface wave and free oscillation attenuation measurements. EOS Trans.-Am. Geophys. Union 78, F485.

Matas, J., Bukowinski, M., 2007. On the anelastic contribution to the temperature dependence of lower mantle seismic velocities. Earth Planet. Sci. Lett., doi: 10.1016/j.epsl.2007.04.028.

McEvilly, T., 1964. Central US crust-upper mantle structure from Love and Rayleigh wave phase velocity inversion. Bull. Seism. Soc. Am 54, 1997–2015.

McKenzie, D., Priestley, K., 2008. The influence of lithospheric thickness variations on continental evolution. Lithos 102, 1–11.

Mégnin, C., Romanowicz, B., Dec. 2000. The three-dimensional shear velocity structure

of the mantle from the inversion of body, surface and higher-mode waveforms. Geophys. J. Int. 143, 709–728.

Meier, U., Curtis, A., Trampert, J., Aug. 2007. Fully nonlinear inversion of fundamental mode surface waves for a global crustal model. Geophys. Res. Lett. 34 (L16304).

Minster, B., Anderson, D., 1981. A model of dislocation-controlled rheology for the mantle. Phil. Trans. R. Soc. Lond. 299, 319–356.

Montagner, J.-P., Jobert, N., Aug. 1988. Vectorial tomography?ii. application to the indian ocean. Geophys. J. 94, 309–344.

Montagner, J.-P., Kennett, B., 1996. How to reconcile body-wave and normal-mode reference earth models. Geophys. J. Int. 125, 229–248.

Montagner, J.-P., Tanimoto, T., Nov. 1991. Global upper mantle tomography of seismic velocities and anisotropies. J. Geophys. Res. 96, 20337–20351.

Mooney, W. D., Laske, G., Guy Masters, T., Jan. 1998. Crust 5.1: A global crustal model at 5 deg $\times$ deg. J. Geophys. Res. 103, 727–748.

Muller, R., Sdrolias, M., Gaina, C., Roest, W., 2008. Age, spreading rates, and spreading asymmetry of the worldÕs ocean crust. Geochem. Geophys. Geosyst 9 (4).

Nataf, H., Ricard, Y., May 1996. 3smac: an a priori tomographic model of the upper mantle based on geophysical modeling. Phys. Earth Planet. Inter. 95, 101–122.

Nataf, H., Ricard, Y., 1996. 3SMAC: an a priori tomographic model of the upper mantle based on geophysical modeling. Physics of the Earth and Planetary Interiors 95 (1), 101–122.

Nettles, M., Dziewoński, A., 2008. Radially anisotropic shear velocity structure of the upper mantle globally and beneath North America. Journal of Geophysical Research-Solid Earth 113 (B2), B02303.

Panning, M., Capdeville, Y., Romanowicz, B., 2009. Seismic waveform modelling in a 3-D Earth using the Born approximation: potential shortcomings and a remedy. Geophysical Journal International 177 (1), 161–178.

Panning, M., Romanowicz, B., 2004. Inference on flow at the base of the earth's mantle based on seismic anisotropy. Science 303, 351–353.

Panning, M., Romanowicz, B., Oct. 2006. A three-dimensional radially anisotropic model of shear velocity in the whole mantle. Geophys. J. Int. 167, 361–379.

Pasyanos, M., 2009. Lithospheric thickness modeled from long-period surface wave dispersion. Tectonophysics doi:10.1016/j.tecto.2009.02.023.

Pasyanos, M., Nyblade, A., 2007. A top to bottom lithospheric study of Africa and Arabia. Tectonophysics 444 (1-4), 27–44.

Pasyanos, M. E., Dec. 2005. A variable resolution surface wave dispersion study of eurasia, north africa, and surrounding regions. J. Geophys. Res. 110 (B12301).

Priestley, K., Debayle, E., McKenzie, D., Pilidou, S., 2006. Upper mantle structure of eastern Asia from multimode surface waveform tomography. Journal of Geophysical Research-Solid Earth 111 (B10), B10304.

Priestley, K., McKenzie, D., 2006. The thermal structure of the lithosphere from shear wave velocities. Earth and Planetary Science Letters 244 (1-2), 285–301.

Priestley, K., McKenzie, D., Debayle, E., Pilidou, S., 2008. The African upper mantle and its relationship to tectonics and surface geology. Geophysical Journal International 175 (3), 1108–1126.

Qin, Y., Capdeville, Y., Montagner, J., Boschi, L., Thorsten, W. B., Feb 2009. Reliability of mantle tomography models assessed by spectral element simulation. Geophys. J. Int. 177, 125–144.

Ribe, N., 1989. Seismic anisotropy and mantle flow. J. geophys. Res 94, 4213–4223.

Ribe, N., 1992. On the relation between seismic anisotropy and finite strain. Journal of Geophysical Research-Solid Earth 97 (B6).

Ricard, Y., Nataf, H., Montagner, J., 1996. The three-dimensional seismological model a priori constrained: Confrontation with seismic data. Journal of Geophysical Research-Solid Earth 101 (B4).

Ricard, Y., Richards, M., Lithgow-Bertelloni, C., Stunff, Y. L., 1993. A geodynamic model of mantle density heterogeneity. J. Geophys. Res. 98, 21895–21910.

Richards, M. A., Hager, B. H., 1984. Geoid anomalies in a dynamic earth. J. Geophys. Res. 89, 5987–6002.

Ritsema, J., Cupillard, P., Tauzin, B., Xu, W., Stixrude, L., Lithgow-Bertelloni, C., 2009. Joint mineral physics and seismic wave traveltime analysis of upper mantle temperature. Geology 37 (4), 363.

Ritsema, J., van Heijst, H. J., Woodhouse, J. H., Feb 2004. Global transition zone tomography. J. Geophys. Res. 109 (B02302).

Ritzwoller, M., Shapiro, N., Leahy, G., 2003. A resolved mantle anomaly as the cause of the Australian-Antarctic Discordance. J. geophys. Res 108 (B12), 2559.

Rodi, W., Glover, P., Li, T., Alexander, S., 1975. A fast, accurate method for computing group-velocity partial derivatives for Rayleigh and Love modes. Bulletin of the Seismological Society of America 65 (5), 1105.

Romanowicz, B., Jul. 1987. Multiplet-multiplet coupling due to lateral heterogeneity: Asymptotic effects on the amplitude and frequency of the earth's normal modes. Geophy. J. Inter. 90, 75–100.

Romanowicz, B., 1990. The upper mantle degree 2: constraints and inference from global mantle wave attenuation measurements. J. Geophys. Res. 95, 11051–11071.

Romanowicz, B., 1991. Seismic tomography of the Earth's mantle. Annual Review of Earth and Planetary Sciences 19 (1), 77–99.

Romanowicz, B., 1994. Anelastic tomography: a new perspective on upper mantle thermal structure. Earth Planet. Sci. Lett 128, 113–121.

Romanowicz, B., 2009. The Thickness of Tectonic Plates. Science 324 (5926), 474.

Romanowicz, B., Mitchell, B., 2007. Deep earth structure: Q of the earth from crust to core. In: Schubert, G. (Ed.), Treatise on Geophysics. Vol. 1. Elsevier, pp. 731–774.

Romanowicz, B., Panning, M., Gung, Y., Capdeville, Y., 2008. On the computation of long period seismograms in a 3-D earth using normal mode based approximations. Geophysical Journal International 175 (2), 520–536.

Roult, G., Clévédé, E., 2000. New refinements in attenuation measurements from free-oscillation and surface-wave observations. Phys. Earth Planet. Inter. 121, 1–2.

Rychert, C., Shearer, P., 2009. A Global View of the Lithosphere-Asthenosphere Boundary. Science 324 (5926), 495.

Schimmel, M., Assumpçao, M., VanDecar, J., 2003. Seismic velocity anomalies beneath SE Brazil from P and S wave travel time inversions. J. geophys. Res 108 (2191), 3–1.

Sebai, A., Stutzmann, E., Montagner, J., Sicilia, D., Beucler, E., 2006. Anisotropic structure of the African upper mantle from Rayleigh and Love wave tomography. Physics of the Earth and Planetary Interiors 155 (1-2), 48–62.

Selby, N. D., Woodhouse, J. H., 2002. The q structure of the upper man-

tle: Constraints from rayleigh wave amplitudes. J. Geophys. Res. 107, 2097, doi:10.1029/2001JB000257.

Shapiro, N., Ritzwoller, M., 2002. Monte-Carlo inversion for a global shear-velocity model of the crust and upper mantle. Geophysical Journal International 151 (1), 88–105.

Shito, A., Karato, S.-i., Park, J., 2004. Frequency dependence of q in earth's upper mantle inferred from continuous spectra of body waves. Geophys. Res. Lett. 31, 10.1029/2004GL019582.

Sigloch, K., McQuarrie, N., Nolet, G., 2008. Two-stage subduction history under North America inferred from multiple-frequency tomography. Nature Geoscience 1 (7), 458–462.

Simmons, N., Forte, A., Grand, S., 2006. Constraining mantle flow with seismic and geodynamic data: A joint approach. Earth and Planetary Science Letters 246 (1-2), 109–124.

Simons, F., van der Hilst, R., Montagner, J., Zielhuis, A., 2002. Multimode Rayleigh wave inversion for heterogeneity and azimuthal anisotropy of the Australian upper mantle. Geophysical Journal International 151 (3), 738–754.

Sipkin, S., Jordan, T., 1979. Frequency dependence of q_{ScS}. Bull. Seism. Soc. Amer. 69, 1055–1079.

Sleep, N., 1989. Hotspots and mantle plumes: Some phenomenology. Journal of Geophysical Research-Solid Earth 95 (B5), 6715–6736.

Smith, M., Dahlen, F., 1981. The period and q of the chandler wobble. Geophys. J. R. Astr. Soc. 64, 223–281.

Spetzler, J., Trampert, J., 2003. Implementing spectral leakage corrections in global surface wave tomography. Geophysical Journal International 155 (2), 532–538.

Spetzler, J., Trampert, J., Snieder, R., 2002. The effect of scattering in surface wave tomography. Geophysical Journal International 149 (3), 755–767.

Steinberger, B., 2000. Plumes in a convecting mantle: Models and observations for individual hotspots. Journal of Geophysical Research-Solid Earth 105 (B5).

Stutzmann, E., Montagner, J.-P., Oct. 1994. Tomography of the transition zone from the inversion of higher-mode surface waves. Phys. Earth Planet. Inter. 86, 99–115.

Su, W., Dziewonski, A., 1991. Predominance of long-wavelength heterogeneity in the mantle. Nature 352, 121–126.

Su, W., Woodward, R., Dziewonski, A., 1992. Deep origin of mid-ocean-ridge seismic velocity anomalies. Nature 360, 149–152.

Tape, C., Liu, Q., Maggi, A., Tromp, J., 2009. Adjoint tomography of the southern California crust. Science 325 (5943), 988.

Tarantola, A., 1984. Inversion of seismic reflection data in the acoustic approximation. Geophysics 49 (8), 1259–1266.

Tarantola, A., 2005. Inverse problem theory and methods for model parameter estimation. Society for Industrial Mathematics.

Tarantola, A., Valette, B., 1982. Generalized nonlinear inverse problems solved using the least squares criterion. Rev. Geophys. Space Phys. 20, 219–232.

Trampert, J., Snieder, R., 1996. Model estimations biased by truncated expansions: possible artifacts in seismic tomography. Science 271 (5253), 1257.

Tromp, J., Tape, C., Liu, Q., 2005. Seismic tomography, adjoint methods, time reversal and banana-doughnut kernels. Geophysical Journal International 160 (1), 195–216.

Ulug, A., Berckhemer, H., 1984. Frequency dependence of q for seismic body waves in the earth's mantle. J. Geophys. 56, 9–19.

Vinnik, L., 1977. Detection of waves converted from P to SV in the mantle. Physics of the Earth and Planetary Interiors 15, 39–45.

Wang, Z., Dahlen, F., 1995. Validity of surface-wave ray theory on a laterally heterogeneous earth. Geophysical Journal International 123 (3), 757–773.

Wang, Z., Dahlen, F. A., 1995. Spherical-spline parametrization of three-dimensional earth models. Geophys. Res. Lett. 22, 3099–3102.

Weeraratne, D., Forsyth, D., Fischer, K., Nyblade, A., 2003. Evidence for an upper mantle plume beneath the Tanzanian craton from Rayleigh wave tomography. Journal of Geophysical Research-Solid Earth 108 (B9), 2427.

Widmer, R., Masters, G., Gilbert, F., 1991. Spherically symmetric attenuation within the earth from normal mode data. Geophys. J. Int. 104, 541–553.

Woodhouse, J. H., 1998. The calculation of eigenfrequencies and eigenfunctions of the free oscillations of the earth and the sun. In: Seismological Algorithms. Ed. D. J. Doornbos, Elsevier, New York, pp. 321–370.

Woodhouse, J. H., Dahlen, F. A., May 1978. The effect of a general aspherical perturbation on the free oscillations of the earth. Geophys. J. R. Astr. Soc. 53, 335–354.

Woodhouse, J. H., Dziewonski, A. M., Jul. 1984. Mapping the upper mantle: Three dimensional modeling of earth structure by inversion of seismic waveforms. J. Geophys. Res. 89, 5953–5986.

Woodhouse, J. H., Girnius, T. P., Mar. 1982. Surface waves and free oscillations in a regionalized earth model. Geophys. J. R. Astr. Soc. 68, 653–673.

Xu, W., Lithgow-Bertelloni, C., Stixrude, L., Ritsema, J., 2008. The effect of bulk composition and temperature on mantle seismic structure. Earth and Planetary Science Letters 275 (1-2), 70–79.

Zhang, Y., Tanimoto, T., 1992. Ridges, hotspots and their interaction as observed in seismic velocity maps. Nature 355, 45–49.

Zhou, Y., Nolet, G., Dahlen, F., Laske, G., 2006. Global upper-mantle structure from

finite-frequency surface-wave tomography. Journal of Geophysical Research-Solid Earth 111 (B4), B04304.